

The Role of Surface Oxidation in the Break-Up of Laminar Liquid Metal Jets

by

Pyongwon Yim

S.B., Mechanical Engineering, Northeastern University (1987)

S.M., Mechanical Engineering, Northeastern University (1989)

Submitted to the Department of Mechanical Engineering
in Partial Fulfillment of the Requirements for the Degree of

DOCTOR OF PHILOSOPHY IN MECHANICAL ENGINEERING

at the

MASSACHUSETTS INSTITUTE OF TECHNOLOGY


June 1996

© 1996 Massachusetts Institute of Technology
All Rights Reserved


Signature of Author:


Department of Mechanical Engineering
February 15, 1996

Certified by:


Jung-Hoon Chun
Edgerton Associate Professor of Mechanical Engineering
Chairman, ~~Doctoral~~ Thesis Committee

Accepted by:


Ain A. Sonin
Professor of Mechanical Engineering
Chairman, Department Graduate Committee

MASSACHUSETTS INSTITUTE
OF TECHNOLOGY

JUN 27 1996

ARCHIVES

LIBRARIES

The Role of Surface Oxidation in the Break-Up of Laminar Liquid Metal Jets

by

Pyongwon Yim

Submitted to the Department of Mechanical Engineering
on February 15, 1996 in Partial Fulfillment of the Requirements for the Degree of
Doctor of Philosophy in Mechanical Engineering

ABSTRACT

The Uniform Droplet Spray (UDS) process, developed in the Laboratory for Manufacturing and Productivity at MIT, offers many advantages over such conventional metal droplet production processes as gas atomization. The process exploits the acoustically-amplified capillary instability phenomenon of laminar liquid jets to produce uniform droplets. The principal advantage of the UDS process is the facility to produce uniform liquid droplets, which allows for greater control of the thermal state and mass flux of the droplet spray.

The present work investigates the various basic phenomena associated with the UDS process. The thesis comprises three primary parts. The first part investigates the break-up behavior of molten metal jets and compares the results to theories by Lord Rayleigh and others. This was achieved by spraying pure tin into a chamber containing less than 5 ppm of oxygen. The second part investigates the viability of the UDS process for producing large solder balls that can be used for Ball-Grid Array (BGA) Integrated Circuit packaging. It also examines whether the balls so produced are comparable to or better than those produced by conventional processes. The final part investigates the role of surface oxidation in the break-up behavior of liquid metal jets. Again, pure tin was used in this part of the investigation to study the effect of surface oxidation on jet break-up.

From the experimental results and theoretical considerations it is shown that: (i) the break-up behavior of a molten metal jet can be explained by Rayleigh's theory, provided that there is sufficiently low oxygen environment, (ii) large solder balls can be produced cost effectively by the UDS process for BGA packaging, and they are comparable to or better than those that are produced by conventional processes in terms of dimensional tolerance and microstructure, and (iii) the jet of molten tin does not break into a train of uniform droplets if the spray chamber contains more than 1500 ppm of oxygen. Implications of these results to the design and control of the UDS process are discussed and research topics for further investigation are suggested.

Thesis Committee:

Jung-Hoon Chun, Chairman

Esther and Harold E. Edgerton Associate Professor of Mechanical Engineering

Teiichi Ando

Research Associate Professor of Mechanical Engineering, Tufts University

Nannaji Saka

Principal Research Scientist of Mechanical Engineering

Ain A. Sonin

Professor of Mechanical Engineering

Acknowledgments

I would like to express my sincerest appreciation to Professor Jung-Hoon Chun, who has guided me for the past four years. Without his constant encouragement and valuable advice, there would be no thesis today. I also would like to extend my gratitude to my thesis committee members, Dr. Nannaji Saka, Professor Teiichi Ando at Tufts University, and Professor Ain A. Sonin, who raised many important issues and offered me valuable advice. My sincere and personal appreciation goes to Dr. Saka, who has helped me to shape the thesis and guided me along the way. His advice on the research as well as other interesting perspectives on life has been invaluable. In addition, I would like to thank Professor H. Metghalchi, my old advisor at Northeastern University, for valuable advice and encouragement.

I have been very fortunate to work with many friends at the Droplet-Based Manufacturing laboratory and to work in a challenging, yet pleasant environment. Thank you, Chen-An Chen, Christian and Honor Passow, Sucharita Sahu, Godard Abel, Manish Bhatia, Wesley “westicle” Williams for machining so many parts and components for all of us in the DBM group, Jeanie Cherng, Randy Hyun, Paul Acquaviva, Juan-Carlos Rocha, Jiun-Yu Lai, and Ho-Young Kim. Thank you, Professor Seung-Hun Park, a visiting professor from Inha University. It has been a privilege to work with such a great group. Good luck to all of you and I hope I can work with you in the future.

To my other lab and office mates — Tom Nowak, Mark Hytros, Dongsik Kim, Jim Derksen, Sangjun Han, and Greg Hubbard — my sincere thanks. My deepest appreciation goes to Tom, who has been my confidant and friend for the past six years and helped me over difficult times.

Thank you, Leslie Regan for everything you have done for me behind the scenes. Thank you, Julie Drennan who proofread the whole thesis from cover to cover; also to Diane DiAlderete, Mina Yang, Heather Cole, Sally Stiffler, and Karuna Mohindra. Thank you, Fred Cote for helping me with design and machining of experimental apparatuses, and Chris Shutts for helping me with the design of a frequency reducer.

I would like to thank sponsors, who provided the research funding. They include: Leaders for Manufacturing Program, and DBM Research Program sponsors, especially, Unilever, and Fukuta Metals.

To the Composite Polymer Processing Program group — Professor Timothy Gutowski, Dr. Greg Dillion, Steven Stoller, Late Dr. Zhong Cai, Dr. Albert Tam, Eric Wang, Dr. Ein-Teck Neoh, Eric Kim, Stuart Mutter, Javier Gonzalez-Zugasti, Kate Gasser, Susan Fatur, Harong Li, Dr. Andre Sharon, Dr. David Hault, and Dr. Richard Okine of duPont — my sincere gratitude.

I would like to acknowledge Dr. Vinod Sikka of Oak Ridge National Laboratories for providing me with some of the micrographs in Chapter 5; Dr. Marcelino Essien of Sandia National Laboratories for helpful discussions; and Ms. Libby Shaw, a facility coordinator in the Auger Spectroscopy Laboratory, for the help with the measurements of oxide layer thickness of tin powders and fibers. The oxide measurement studies made use of MRSEC Shared Facilities supported by the National Science Foundation under Award Number DMR-9400334.

Thank you, sun-bae-hyoung-deul (seniors) — Dr. Sungwoon Cha, who has been like an older brother I never had, encouraged and rallied behind me through hard times at MIT and put things into a broader perspective, Professor Chul-Bum Park (University of Toronto) whose work habit and faith in Christianity are legendary, Dr. Yun-Jae Kim, Professor Dae-Eun Kim (Yonsei University), Professor Jaebok Song (Korea University), Dr. Sungdo Ha, Professor Woo-Chun Choi (Korea University), Professor Hyungyil Lee (Sogang University), and Kun Bang.

My sincerest thanks to my dong-ki-duel (friends and colleagues) — Daeyup Lee who has been always there for me when I needed a sounding board, Dr. Kyoungdoug Min who made MIT a little easier place to be, and a wonderful roommate for four years, Haeseong Jee who has offered his helping hands when I needed one, Chang-Dong Yoo, Kyeongsun Joo, Dr. Sang-Woo Pyo, In-Soo Suh, Yung-Joon Lee, and Dr. Siyoul Jang. I will always cherish your friendship and the support you gave me during my stay at MIT.

Thanks also to my hu-bae-deul (juniors) — Sukyoung Chey who has been the best hu-bae I ever had and always has been very considerate, thoughtful and kind, Professor Seung-Jin Song (Inha University), Ben Lee, Dr. Brian Kang, the renaissance man at MIT, Jungmok Bae, Shin Suk Park, Kontong Pahng, Sunghwan Jung, Jeong-Ho Park, Woogil Lee, and Tongkwon Shin.

My friends at the Korean Presbyterian Church in Brookline, Drs. John Chuwon Choi, Jeannie Jooyoung Min, and Jay Jaesoo Pak, helped me to endure very uncertain times when my mom was diagnosed with a stomach cancer in early November of 1995. Without their medical advice and moral encouragement, our family would have had a very difficult time during my mom's surgery, recovery, and therapy periods. I also would like to extend my sincere thanks to my friends at the young adult group — Byungmoo Lee, Dr. Hyung-Joon Paik, Kee-Nam Park, Dongho and Young Jin, Chong Bum Kim, Yon Jin Kim, Youmi Cho, Youkyung Kim, and Jeom Nye Yee. Thank you, Elders Yeonil Choe and Wha-Kyung Byun Sherman for advising and supporting the group beyond your duties and calls. My sincerest thanks to Rev. and Mrs. Young Ghil Lee and Dr. and Mrs. Chull Lee for their prayers and encouragement.

Thank you, John D. and Marcie, Doug, and Tom Conway for helping me and my family to adjust to this country. Thank you, Auntie and Uncle (Mr. John R. Conway and Mrs. Minja Yim Conway). I will be forever grateful for all the things you have done for me and my family. I hope my paternal grandfather (Mr. Young-Joon Yim) and my maternal great-grandfather (Mr. Sung-Moon Lee) are smiling from up above.

Thanks for everything, HaeSun.

To my wonderful family, I can find no words to express my sincerest appreciation, and love. Thank you, Mom and Dad (Mr. Ho Yim and Mrs. Young Nan Yu Yim) to whom this thesis is dedicated. Thank you, Pyonghye, Pyongjin, Pyongduk, and Pyongson. Your unconditional love, support, and encouragement made my stay at MIT possible.

Table of Contents

Title Page	1
Abstract	2
Acknowledgments	3
Table of Contents	5
List of Tables	8
List of Figures	10
1 INTRODUCTION	15
1.1 Background and Motivation	15
1.2 The Break-up of Liquid Jets	18
1.3 Objectives of the Present Investigation	20
1.4 Overview of the Thesis	21
2 CAPILLARY INSTABILITY OF LAMINAR LIQUID JETS	22
2.1 Introduction	22
2.2 Linear Theory	23
2.3 The Formation of Satellites	30
2.4 Effects of Material Properties on the Behavior of Jet Break-Up	31
2.4.1 Role of surface tension	32
2.4.2 Role of viscosity	34
2.5 Behavior of Jet Break-Up in Another Liquid Medium	36
2.6 Conclusions	39
Nomenclature	39
3 TRAJECTORY AND HEAT TRANSFER OF DROPLETS	42
3.1 Introduction	42
3.2 Jet Velocity	42
3.3 Trajectory of Droplets	45
3.3.1 Electro-repulsion force	46
3.3.1 Drag force	47
3.4 Solidification of Droplets	49
3.4.1 Results of solidification simulations and their implications	51

3.4.2	Effect of solidification on droplet size	55
3.5	Conclusions	56
	Nomenclature	56
4	EXPERIMENTAL STUDIES OF JET BREAK-UP BEHAVIOR	59
4.1	Introduction	59
4.2	Experimental Apparatus and Procedure	59
4.2.1	Experimental apparatus	59
4.2.2	Experimental procedure	61
4.3	Results and Discussion	62
4.3.1	Measurement of jet velocity	62
4.3.2	Variations of jet velocities with respect to different runs	65
4.3.3	Jet break-up length with respect to time	72
4.3.4	Jet break-up length with respect to dimensionless wavelength	74
4.3.5	Jet break-up length with respect to perturbation amplitude	77
4.4	Conclusions	78
	Nomenclature	79
5	PRODUCTION AND CHARACTERIZATION OF MONO-SIZED BALLS	81
5.1	Introduction	81
5.2	Experimental Procedure	82
5.2.1	Production of solder balls	82
5.2.2	Jet break-up	84
5.2.3	Characterization of solder balls	86
5.3	Results and Discussion	86
5.3.1	Appearance and sphericity	86
5.3.2	Size distribution and production yield	88
5.3.3	Microstructures and re-melting characteristics	92
5.4	Process Viability	95
5.5	Conclusions	96
	Nomenclature	97
6	EFFECTS OF OXIDATION ON JET BREAK-UP BEHAVIOR: THEORY	98
6.1	Introduction	98
6.2	Thermodynamic Equilibrium Conditions for Oxidation	99
6.3	Oxidation of Metals	102
6.4	Gas Phase Mass Transfer	109
6.4.1	Gas phase mass transfer using stagnant film theory	110

6.4.2	Gas phase mass transfer using boundary layer theory	111
6.4.3	Diffusion length in the gas phase using the kinematic viscosity of gas	113
6.4.4	Estimation of tin oxide layer thickness using the diffusion length in the gas phase	113
6.5	Possible Oxidation Mechanisms and Oxide Layer Thickness	116
6.6	Property Changes as a Result of Oxidation	120
6.7	Conclusions	122
	Nomenclature	123
7	EFFECTS OF OXIDATION ON JET BREAK-UP BEHAVIOR: EXPERIMENTAL	127
7.1	Experimental Apparatus and Procedure	127
7.1.1	Experimental apparatus for the investigation of jet break-up	127
7.1.2	Experimental procedure for the investigation of jet break-up	128
7.1.3	Experimental apparatus and procedures for the investigation of oxide layer thickness	130
7.2	Results and Discussion	133
7.2.1	Effect of oxygen content on the jet break-up length	133
7.2.2	Effect of amplitude on the jet break-up length	136
7.2.3	Effect of dimensionless wavelength on the jet break-up length at various partial pressures of oxygen	137
7.2.4	Oxide layer thickness measurement by the Auger Electron Spectroscopy	138
7.2.5	Area mapping of oxide layer surface by the Auger Electron Spectroscopy	147
7.2.6	Effect of oxide film thickness and its ultimate strength on the jet break-up	148
7.3	Conclusions	152
	Nomenclature	153
8	SUMMARY	154
9	RECOMMENDATIONS FOR FURTHER RESEARCH	158
	BIBLIOGRAPHY	161
	APPENDIX	166
A	PHYSICAL PROPERTIES OF SELECTED MATERIALS	166

List of Tables

Table 1.1	Dimensionless wavelength (the ratio of wavelength to jet diameter) for producing uniform droplets	20
Table 2.1	Droplet formation regimes based on the various forces acting on a liquid jet	22
Table 2.2	Properties of various materials	29
Table 2.3	The relationship between the value of μ_l/μ_g and the value of ka for maximum instability and the corresponding wavelength	38
Table 4.1	Properties of pure tin	63
Table 4.2	Theoretical velocities and Reynolds number of flow conditions for selected pressure ranges	64
Table 4.3	Measured velocities by three different methods	64
Table 4.4	Jet velocity measurement uncertainties by mass flow rate due to different variables	68
Table 4.5	Jet velocity measurement uncertainties by video measurement due to different variables	69
Table 4.6	Jet velocity measurement uncertainties by droplet measurement due to different variables	70
Table 4.7	Uncertainties of jet velocity due to pressure settings	71
Table 5.1	Process conditions used to produce Sn-38 wt.% Pb balls	84
Table 5.2	Yield of mono-sized balls	91
Table 6.1	The thickness of tin oxide layer with respect to the oxygen content in the spray chamber. The pressure of spray chamber is assumed to be 135 kPa (5 psig), temperature 298 K, molecular weight of stannic oxide, SnO ₂ , 150.7 kg/kmol, and density of SnO ₂ 7000 kg/m ³ . The jet diameter is assumed to be 100 μm.	116
Table 6.2	Structures and atomic volumes of selected materials	119
Table 7.1	Thickness of oxide film capable of withstanding the pressure caused by the surface tension of a liquid of 0.544 N/m	151
Table 8.1	The thickness of tin oxide layer with respect to the oxygen content in the spray chamber. The pressure of spray chamber is assumed to be 135 kPa (5 psig), temperature 298 K, molecular weight of	

	stannic oxide, SnO_2 , 150.7 kg/kmol, and density of SnO_2 7000 kg/m ³ . The jet diameter is assumed to be 100 μm .	156
Table A.1	Physical properties of pure metals at normal temperatures	166
Table A.2	Physical properties of pure metals at elevated temperatures	167
Table A.3	Physical properties of liquid metals	168
Table A.4	Thermal and electrical properties of liquid metals	169
Table A.5	Density of solid lead-tin at 293 K	170
Table A.6	Density of liquid lead-tin with the relationship of $\rho = c_1 + c_2(T - 273)$	171
Table A.7	The physical properties of silicone oil	172

List of Figures

Figure 1.1	Schematic diagram of a conventional spray forming process.	16
Figure 1.2	Schematic diagram of the droplet generator of an UDS apparatus.	16
Figure 1.3	Schematic diagram of the UDS apparatus.	17
Figure 1.4	SEM picture of tin fibers at 200x magnification. Fibers are produced when the continuous laminar jet of molten metal is sprayed into a chamber in which oxygen content is sufficiently high. The orifice diameter is 100 μm , and the ejection pressure 90 kPa, resulting in jet velocity of ~ 3.9 m/s. The spray chamber was at atmospheric pressure.	19
Figure 1.5	SEM picture of uniform tin powders at 200x magnification.	19
Figure 2.1	Representation of the liquid disintegration with respect to the Reynolds and Ohnesorge numbers.	23
Figure 2.2	Schematic diagram of the break-up of a laminar jet.	24
Figure 2.3	Break-up of liquid tin jet. The diameter of orifice used is 100 μm , jet velocity 4.65 m/s, and vibration frequency 11.34 kHz, which is equivalent to the dimensionless wavelength of 4.1. The resulting droplet diameter was 180 μm .	25
Figure 2.4	Dimensionless growth factor versus dimensionless wavelength by Rayleigh's and Weber's inviscid flow analysis.	27
Figure 2.5	Estimated jet break-up length of various materials based on the orifice diameter of 100 μm and jet velocity of 5 m/s. No material changes during the run due to oxidation are assumed. Weber's equation is used.	29
Figure 2.6	Dimensionless growth rate versus dimensionless wavelength for various Ohnesorge numbers.	30
Figure 2.7	Effect of surface tension and viscosity on the jet break-up length based on the orifice diameter of 100 μm , density 7000 kg / m^3 , jet velocity 5 m/s, and dimensionless wavelength 4.51. Weber's equation is used. (a) Jet break-up length vs. surface tension, (b) Jet break-up length vs. viscosity.	35
Figure 2.8	The relationship between the value of μ_l / μ_g and the value of ka for maximum instability and the corresponding wavelength.	38
Figure 3.1	Droplet charging by the induction method.	43

Figure 3.2	The resultant field E as the sum of the fields due to several point charges.	47
Figure 3.3	Typical heat transfer coefficient of a droplet assuming a pure tin droplet with a diameter of 200 μm , initial velocity of 5 m/s and initial temperature of 555 K. The cooling medium is nitrogen at 298 K.	52
Figure 3.4	Typical solidification curves for droplets. (a) droplet temperature versus distance, (b) liquid fraction of droplet versus distance. The results of solidification simulations based on a droplet diameter of 200 μm , an initial velocity of 5 m/s, and an initial temperature of 555 K are shown in these figures. The cooling medium is nitrogen. The material is pure tin.	53
Figure 3.5	The solidification time of Sn-38 wt.% Pb droplets of various sizes in a nitrogen environment. The initial temperature of the droplet is 508 K.	54
Figure 3.6	The flight distance of Sn-38 wt.% Pb droplets of various sizes in a nitrogen environment. The initial temperature of the droplet is 508 K.	54
Figure 3.7	Possible solidification fronts for droplets.	55
Figure 4.1	Schematic of crucible bottom plate.	61
Figure 4.2	Calculated jet velocity vs. measured jet velocity of liquid tin. Jet diameter is 100 μm . Ejection pressures are 90, 125 and 160 kPa, respectively. The density of liquid tin is assumed to be 6971 kg/m^3 . Jet velocities are calculated assuming the jet diameter is equal to the orifice diameter.	65
Figure 4.3	Measured jet velocity variation due to run to run. The jet velocities are obtained from the mass flow rate measurements. Orifice diameter is 100 μm , ejection pressure 125 kPa. The density of liquid tin is assumed to be 6971 kg/m^3 and jet velocities are calculated assuming the jet diameter is equal to the orifice diameter. The average jet velocity is 4.64 m/s with a standard deviation of 0.08 m/s.	66
Figure 4.4	Calculated jet velocity vs. measured jet velocity of liquid tin with error bars.	71
Figure 4.5	Jet break-up length variation with respect to spraying time for five runs. Jet diameter is 100 μm and ejection pressure 125 kPa, and vibration frequency 11.34 kHz. 400 V was applied to the piezoelectric crystals.	72
Figure 4.6	Break-up of laminar jet.	73
Figure 4.7	Jet break-up length versus dimensionless wavelength at a jet velocity of 4.64 m/s assuming a jet diameter of 100 μm . 400 V was applied to the piezoelectric crystals.	76

Figure 4.8	Jet break-up length versus dimensionless wavelength at various velocities assuming a jet diameter of 100 μm . 400 V was applied to the piezoelectric crystals.	76
Figure 4.9	Jet break-up length with respect to amplitude. Jet diameter is 100 μm , jet velocity 4.75 m/s from the ejection pressure of 125 kPa, and forced vibration frequency 11.34 kHz.	78
Figure 5.1	Uniform Droplet Spray apparatus for producing large solder balls.	83
Figure 5.2	Jet break-up in gaseous atmosphere and in oil.	85
Figure 5.3	SEM picture of Sn-38 wt.% Pb balls produced by the UDS process at 40x magnification. The balls were produced with an orifice of diameter 402 μm , initial jet velocity 2 m/s and vibration frequency 1 kHz.	87
Figure 5.4	SEM picture of irregular-shaped particles at 40x magnification.	88
Figure 5.5	Size distribution of the Sn-38 wt.% Pb balls produced by the UDS process. The balls were produced with an orifice of diameter 402 μm , initial jet velocity 2 m/s and vibration frequency 1 kHz. The mean diameter is 785 μm .	89
Figure 5.6	Optical micrographs of cross sections of solder balls. (a) 50x magnification view of 785 μm Sn-38 wt.% Pb balls produced by the UDS process, (b) 500x magnification view of (a), and (c) 500x magnification view of a 750 μm commercial solder ball.	93
Figure 5.7	Back-Scattered electron images (1000x magnification) of cross sections of solder balls. (a) 785 μm Sn-38 wt.% Pb balls produced by the UDS process, (b) 750 μm commercial solder ball. The Pb-rich phase appears light and the Sn-rich phase dark.	94
Figure 5.8	Heating DSC curves of solder balls. (a) 785 μm Sn-38 wt.% Pb ball produced by the UDS process, (b) 750 μm commercial solder ball.	95
Figure 5.9	Phase diagram of lead-tin alloy system.	96
Figure 6.1	Standard free energy of formation of some selected oxides. ΔG° corresponds to the reaction $(2x/y)\text{M} + \text{O}_2 = (2/y)\text{M}_x\text{O}_y$. The symbol \bullet and $*$ identify the melting and boiling points, respectively, of the metals	101
Figure 6.2	Schematic of oxygen transport in the absence of oxide layer.	103
Figure 6.3	Schematic of transport of oxygen molecules.	105
Figure 6.4	Distribution of the oxidizing species in the oxide layer for the two limiting cases of oxidation.	107
Figure 6.5	Gas phase mass transfer in stagnant film theory.	110

Figure 6.6	Gas phase mass transfer using boundary layer theory.	111
Figure 6.7	Schematic of conversion of oxygen molecules in the boundary layer to metal oxide.	114
Figure 6.8	Possible mechanisms of surface oxidation and the resulting changes in material properties.	121
Figure 6.9	Solid oxide particles in liquid tin.	121
Figure 7.1	Schematic diagram of the UDS apparatus for studying the effects of oxidation on the jet break-up behavior.	128
Figure 7.2	Change of oxidation rates with respect to the solidification of droplets.	131
Figure 7.3	Schematics of oxidation curves under different operating conditions.	131
Figure 7.4	Effects of oxygen content on the jet break-up length. The orifice diameter is 100 μm and the perturbation frequency 11.34 kHz. The voltage input to the piezoelectric crystal was 400 V, which translates to a perturbation amplitude of approximately 4.12×10^{-7} m.	134
Figure 7.5	The jet break-up length of liquid tin versus oxygen concentration in the spray chamber. The orifice diameter is 100 μm , the perturbation frequency 11.34 kHz. The voltage input to the piezoelectric crystal was 400 V, which translates to a perturbation amplitude of approximately 4.12×10^{-7} m.	135
Figure 7.6	Effect of perturbation amplitude on the jet break-up length. The diameter of the orifice used was 100 μm . The frequency applied was 11.34 kHz.	136
Figure 7.7	Effect of frequency and dimensionless wavelength on the jet break-up length due to oxygen content. Orifice diameter is 100 μm and ejection pressure 125 kPa. An average velocity of 4.64 m/s was used. 400 V was applied to the piezoelectric crystal to provide the perturbation amplitude to the nozzle area.	138
Figure 7.8	Auger electron spectroscopy survey for chemical elements on the surface of a sample.	139
Figure 7.9	Montage of oxygen traces at four different places on the tin powder produced at 2,000 ppm oxygen.	141
Figure 7.10	Montage of carbon traces at four different places on the tin powder produced at 2,000 ppm oxygen.	141
Figure 7.11	Montage of tin traces at four different places on the tin powder produced at 2,000 ppm oxygen.	142

Figure 7.12	Montage of oxygen traces at four different places on the tin fiber produced at 200,000 ppm oxygen.	142
Figure 7.13	Intensity of oxygen, carbon, and tin of tin droplets produced at the oxygen level of 5 ppm.	143
Figure 7.14	Intensity of oxygen, carbon, and tin of tin droplets produced at an oxygen level of 500 ppm.	143
Figure 7.15	Intensity of oxygen, carbon, and tin of tin droplets produced at an oxygen level of 2,000 ppm.	144
Figure 7.16	Intensity of oxygen, carbon, and tin of tin droplets produced at an oxygen level of 200,000 ppm.	144
Figure 7.17	Intensity of oxygen, carbon, and tin of tin fiber produced at an oxygen level of 200,000 ppm.	145
Figure 7.18	Intensity of oxygen and tantalum for tantalum with 100 nm oxide layer thickness.	146
Figure 7.19	Free-body diagram.	149
Figure 7.20	Flow of liquid inside of the column of jet due to the pressure caused by surface tension.	150

Chapter 1 INTRODUCTION

1.1 Background and Motivation

In the spray forming of metals, a stream of molten metal is atomized by high velocity gas jets and the atomized droplets are deposited onto a substrate to form a part or a coating as shown schematically in Figure 1.1. For example, the Osprey spray deposition process (Evans et al., 1985) and the Liquid Dynamic Compaction process (Lavernia and Grant, 1988) are now widely used to produce billets, tubes, and sheets. Almost all spray forming processes, however, employ liquid metal droplets of random sizes, thus making the processes difficult to analyze and control.

The Uniform Droplet Spray (UDS) process, invented and developed at the Laboratory for Manufacturing and Productivity, MIT, has many advantages over the conventional gas atomization and spray forming processes (Passow, 1992; Chun and Passow, 1993). The UDS process exploits the capillary instability phenomenon of liquid jets for producing uniform droplets. The principal characteristic of the UDS process is its ability to produce uniform liquid droplets, which allows for a greater control of the thermal state and mass flux of the droplets. The microstructure of the deposit can be readily tailored by controlling the heat and mass fluxes of the droplet spray (Gutierrez-Miravete et al., 1989; Bewlay and Cantor, 1991; Passow, 1992; Passow et al., 1993; Ando et al., 1993; Chen et al., 1994a, 1994b). Figures 1.2 and 1.3 show schematics of a droplet generator and a typical UDS apparatus, respectively.

Many possible applications of the UDS process exist. These include spray-forming, spray-coating, near net-shape manufacturing, tooling, and, of course, uniform metal powder production. One of the important applications of uniform metal powders is in the fabrication of integrated circuit packages, namely, the Ball Grid Array (BGA) packages. In BGA packaging, uniform eutectic solder balls (typically 750 μm in diameter) are used. One of the objectives of the present work, therefore, is to investigate whether the UDS process can be adapted to produce uniform, high-quality balls at lower cost than the conventional processes.

The UDS process accurately and consistently generates uniform droplets from laminar molten metal jets. The ability to control the size and trajectory of droplets and the precise prediction of their thermal state during flight and upon impact on the substrate are the unique features of this process. As will be discussed in Chapter 3, the leading droplets experience more drag force than the trailing ones, which results in droplet merging.

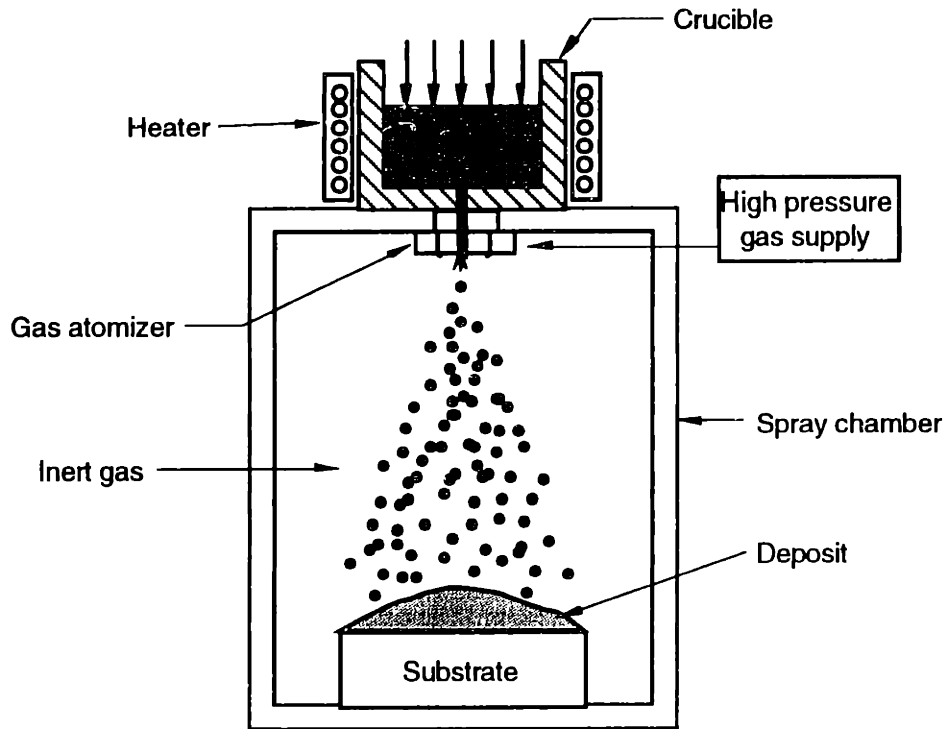


Figure 1.1 Schematic diagram of a conventional spray forming process.

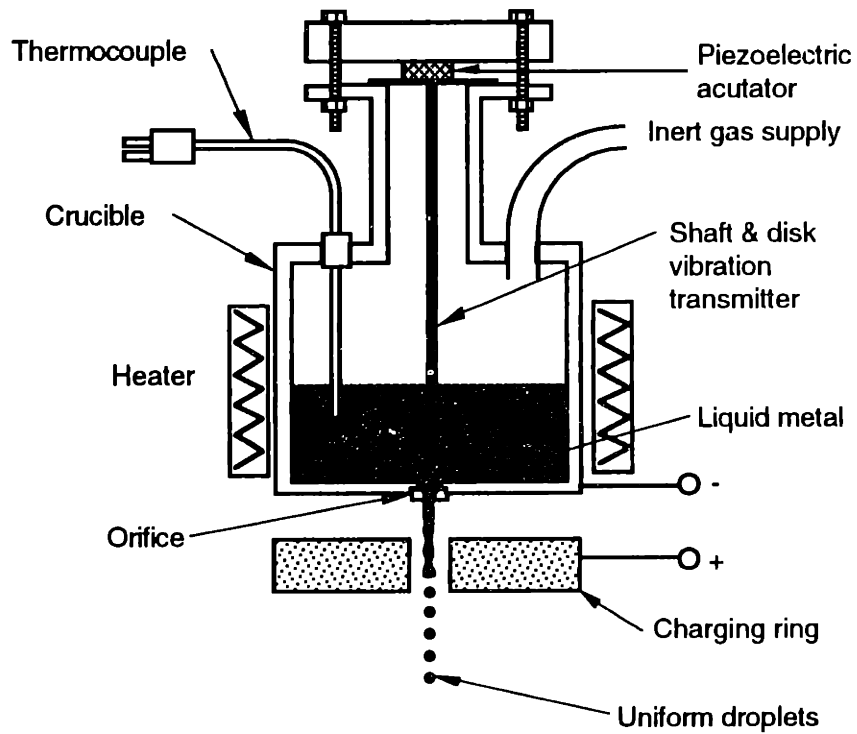


Figure 1.2 Schematic diagram of the droplet generator of an UDS apparatus.

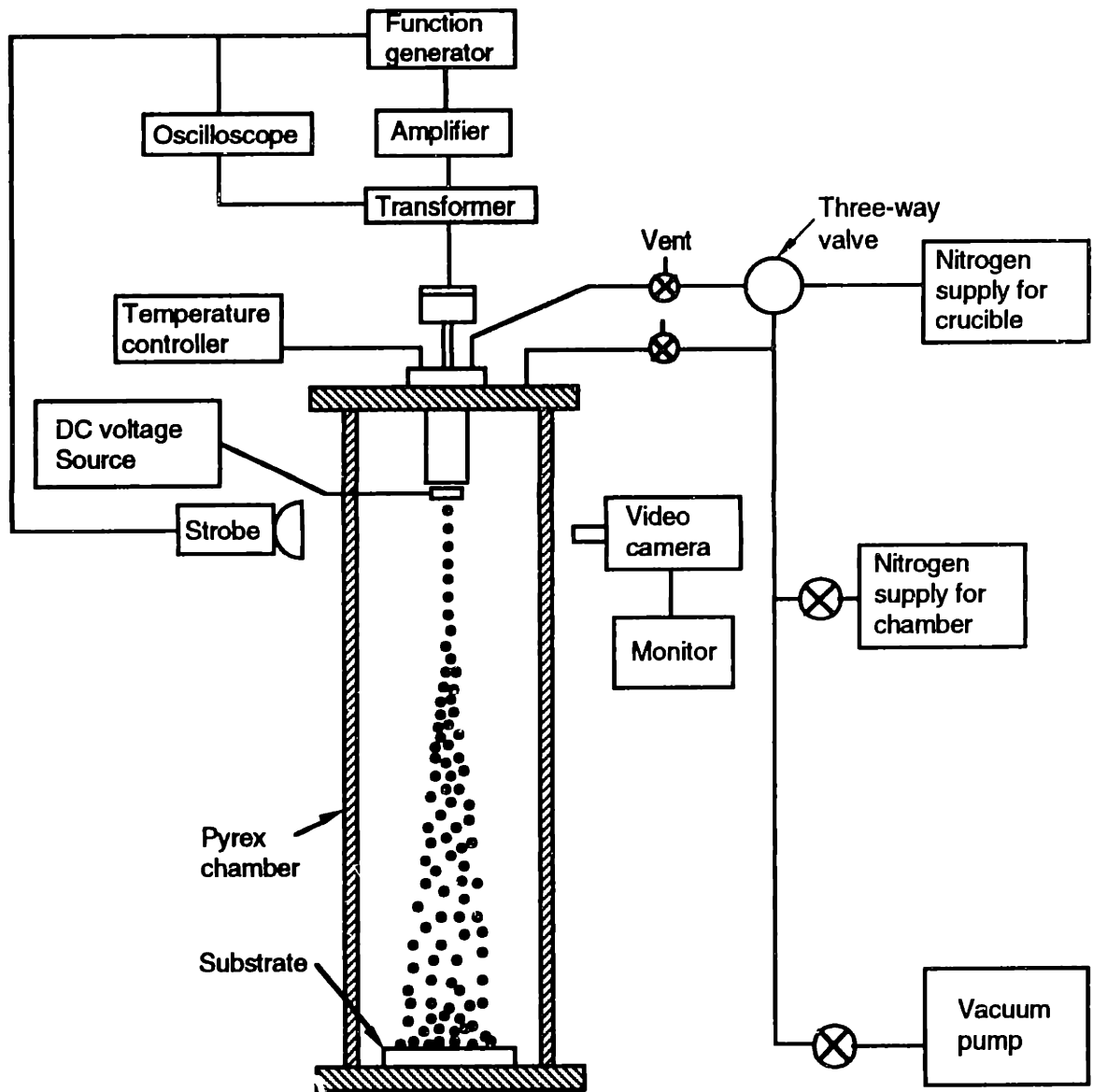


Figure 1.3 Schematic diagram of the UDS apparatus.

It is therefore important to keep the droplets from merging during flight. For this purpose, the droplets are electrostatically charged by induction charging. For the induction charging to be effective, however, the continuous laminar jet must break within the length of the charging plate. Accurate knowledge of the distance from the orifice at which the molten metal jet breaks is thus of great importance.

The break-up length of a liquid jet depends on its physical properties (density, surface tension, and viscosity), the diameter of the orifice, and the amplitude and frequency of the oscillation applied to the jet. Prediction of the break-up length of a reactive molten metal jet is more complicated when it is sprayed into a chamber that contains a sufficiently

high amount of oxygen. Reactive gases may form metal oxides or other tenacious films on the jet surface. In some cases, such surface films stabilize the jet, which results in the production of fibers instead of uniform droplets as shown in Figure 1.4. Thus, determination of the concentration of oxygen below which the molten metal jet can be broken into a train of uniform droplets is of paramount importance to the successful application of the UDS process.

The diameter of uniform metal powders that have been produced by the UDS process ranges from 50 to 800 μm . Figure 1.5 shows uniform tin powders produced by a UDS apparatus. The diameter of the droplets is mainly determined by the nozzle size and is typically twice the nozzle diameter. The perturbation frequency also affects the droplet size, in the range of 1.8 to 2.2 times the nozzle diameter.

1.2 The Break-up of Liquid Jets

It is well known that as a laminar jet of liquid issues from a small nozzle or orifice, the surface tension force of the liquid mediates the jet to break up into a train of droplets. This phenomenon is called capillary instability. Lord Rayleigh (1878) advanced a linear analysis of the break-up phenomenon of free laminar jets. He also suggested that uniform droplets can be produced when the jet is subjected to a periodic oscillation of wavelength greater than the circumference of the jet diameter. A wavelength of 3.5 to 7 times the jet diameter has been used to produce uniform droplets of water (Rayleigh, 1878; Mason et al., 1963; Schneider and Hendricks, 1964; Lindblad and Schneider, 1965; Hendricks and Babil, 1972), and other non-oxidizing liquids, such as sodium nitrite (Erin and Hendricks, 1968) and ink used in ink jet printing technology (Sweet, 1965; Kamphoefner, 1972; Fillmore et al., 1977), as listed in Table 1.1.

The jet break-up length depends on the properties of the liquid metals and the frequency and amplitude of the perturbation at the orifice. One of the difficulties in predicting the jet break-up length of liquid metals is that material properties such as surface tension and viscosity vary with environmental conditions, oxygen partial pressure, and temperature. Another difficulty is that the amplitude of initial disturbance and the frequency at the nozzle area are difficult to determine.

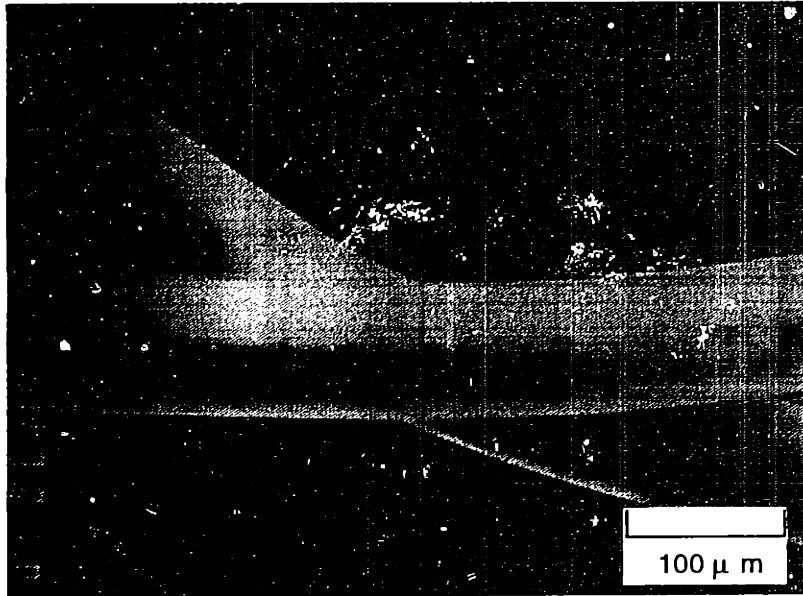


Figure 1.4 SEM picture of tin fibers at 200x magnification. Fibers are produced when the continuous laminar jet of molten metal is sprayed into a chamber in which oxygen content is sufficiently high. The orifice diameter is 100 μm , and the ejection pressure 90 kPa, resulting in jet velocity of ~ 3.9 m/s. The spray chamber was at atmospheric pressure.

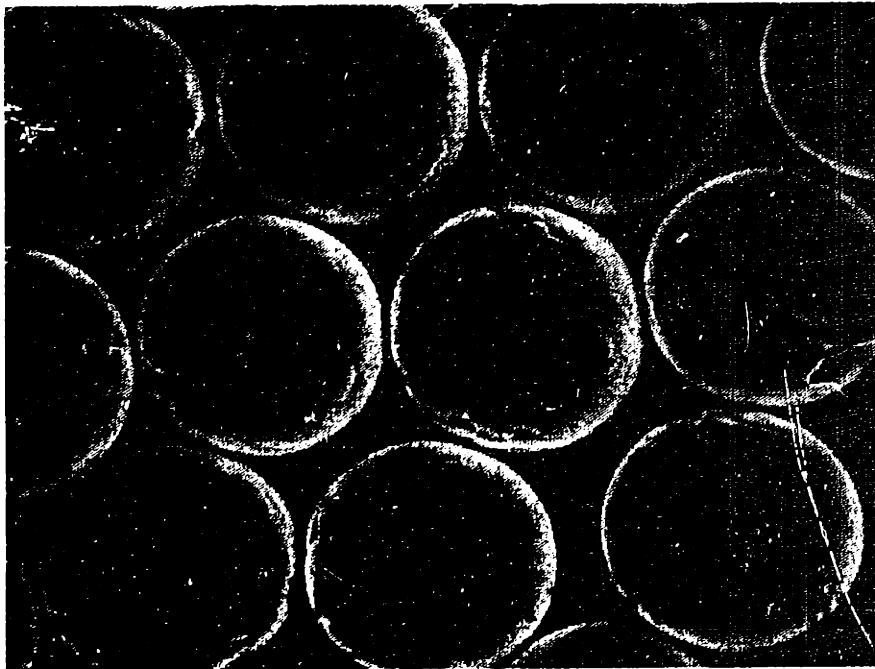


Figure 1.5 SEM picture of uniform tin powders at 200x magnification.

1.3 Objectives of the Present Investigation

This thesis has three primary objectives. The first is to investigate whether the molten metal jet breaks into a train of uniform droplets as predicted by Rayleigh and others when sprayed into an oxygen content low enough not to disturb the break-up behavior of molten metal jets. To investigate this, pure tin was sprayed into a chamber that was charged with industrial grade nitrogen, which typically contains less than 5 ppm oxygen.

Table 1.1 Dimensionless wavelength (the ratio of wavelength to jet diameter) for producing uniform droplets

Material	Dimensionless wavelength	Researchers
Water	3.5 to 7	Schneider and Hendricks, 1964
Sodium Nitrite	5.1 and 5.7	Erin and Hendricks, 1968
Ink	6.0	Sweet, 1965
Ink	4.6	Fillmore et al., 1977
Sn-40 wt.% Pb	3.2 to 10.5	Passow et al., 1993

The second objective is to investigate if large solder balls can be produced for the BGA application and whether such balls are comparable to or better than the balls produced by conventional processes. It was necessary to modify the apparatus to circumvent the requirement of longer solidification distance (or solidification time) since it takes longer flight distances to solidify the larger droplets. For example, 750 μm solder balls normally have to travel vertically downward about 6 m (for an initial velocity of 2 m/s) before they completely solidify.

The third objective is to investigate the role of surface oxidation in the break-up behavior of liquid metal jets. Pure tin was again used to study the effect of surface oxidation. When a continuous laminar molten metal jet is sprayed into an environment of sufficiently high oxygen content, it fails to break into a train of droplets; instead fibers are produced. It is important to characterize the conditions under which such problems occur. In the case of aluminum, which has a high affinity for oxygen, it is necessary to keep the spray chamber free of oxygen as far as possible. Oxygen control may not be necessary for less reactive and noble metals, which do not oxidize readily.

1.4 Overview of the Thesis

The overall goal of the present research is to describe the jet break-up behavior of molten metals when their properties change with environmental conditions. This research should advance the understanding of the UDS process, as well as other processes that rely on surface properties of molten metals, by establishing guidelines that render the process predictable and controllable.

The present chapter describes the background, motivation, and objectives for the thesis. In Chapter 2, the break-up behavior of liquid jets is described in the light of Rayleigh's linear theory for inviscid liquids. Rayleigh's theory is further expanded using Weber's theory (1931) which includes the effect of fluid viscosity. The theories of satellite formation are also briefly mentioned. Also presented is the break-up behavior of laminar liquid jets when sprayed into another liquid medium. All these theories are based on non-reacting atmospheres. Chapter 3 briefly reviews the general physical models of the UDS process, such as charging, trajectory, and heat transfer of droplets. In Chapter 4, the experimental results on the break-up behavior of molten metal jets as they are sprayed into an environment with sufficiently low quantities of oxygen are presented.

Chapter 5 describes the production and characterization of large solder balls (750 μm in diameter). In Chapter 6, the theories of surface oxidation are reviewed and discussed. Molten tin is sprayed into a chamber filled with a known oxygen concentration, < 5 ppm to ~200,000 ppm, to investigate the effects of oxygen concentration on jet break-up. Chapter 7 presents and discusses the results of the jet break-up lengths and oxide layer thickness under various oxygen concentrations. The implications of the experimental results and the theoretical analyses to the UDS process are summarized in Chapter 8. Chapter 9 offers recommendations for further work. The physical properties of certain experimental materials are listed in Appendix A.

Chapter 2 CAPILLARY INSTABILITY OF LAMINAR LIQUID JETS

2.1 Introduction

As a liquid jet issues from a nozzle or orifice, droplets are formed by the actions of various forces: gravity, which acts on the bulk; surface tension (capillary force), which induces small oscillations on the surface of the jet; and surface friction, caused by the aerodynamic motion of the ambient atmosphere surrounding the jet. When the liquid flow rate or the velocity is very small, droplets are formed by the action of gravity alone. As the flow rate increases, however, capillary force dominates the break-up behavior of the jet. When the flow rate becomes even larger, surface friction caused by the turbulent motion of the ambient medium dominates. As listed in Table 2.1, Ohnesorge (1936) classifies the various regimes of the droplet formation process based on the forces participating where the capillary force is taken as unity.

Table 2.1 Droplet formation regimes based on the various forces acting on a liquid jet

Regime	Capillary force	Inertia force	Gravity force	Direct action of viscous friction	Indirect action of viscous friction
I	1	$\rightarrow 0$	substantial	$\rightarrow 0$	0
II	1	moderate	very slight	very slight	$\rightarrow 0$
III	1	increasing	~ 0	substantial	moderate
IV	1	very strong	$\rightarrow 0$	strong	substantial

The droplet formation regimes as a function of the Reynolds and Ohnesorge numbers are shown in Figure 2.1. The Reynolds number is defined as:

$$\text{Re} = \frac{\rho_l v_j d_j}{\mu_l}, \quad (2.1.1)$$

where ρ_l is the density of liquid, v_j the jet velocity, d_j the jet diameter, and μ_l the viscosity of liquid. The Ohnesorge number is defined as:

$$\text{Oh} = \frac{\mu_l}{\sqrt{\rho_l d_j \sigma_l}}, \quad (2.1.2)$$

where σ_j is the surface tension of the liquid. Droplet formation due to capillary instability has been studied by many researchers (Rayleigh, 1878; Mason et al., 1963; Schneider and Hendricks, 1964; Lindblad and Schneider, 1965; Sweet, 1965; Kamphoefner, 1972; Hendricks and Babil, 1972; Passow, 1992; Passow et al., 1993; Abel, 1994). In the following section, the linear theories of the jet break-up process due to Rayleigh (1978) and Weber (1931) are reviewed.

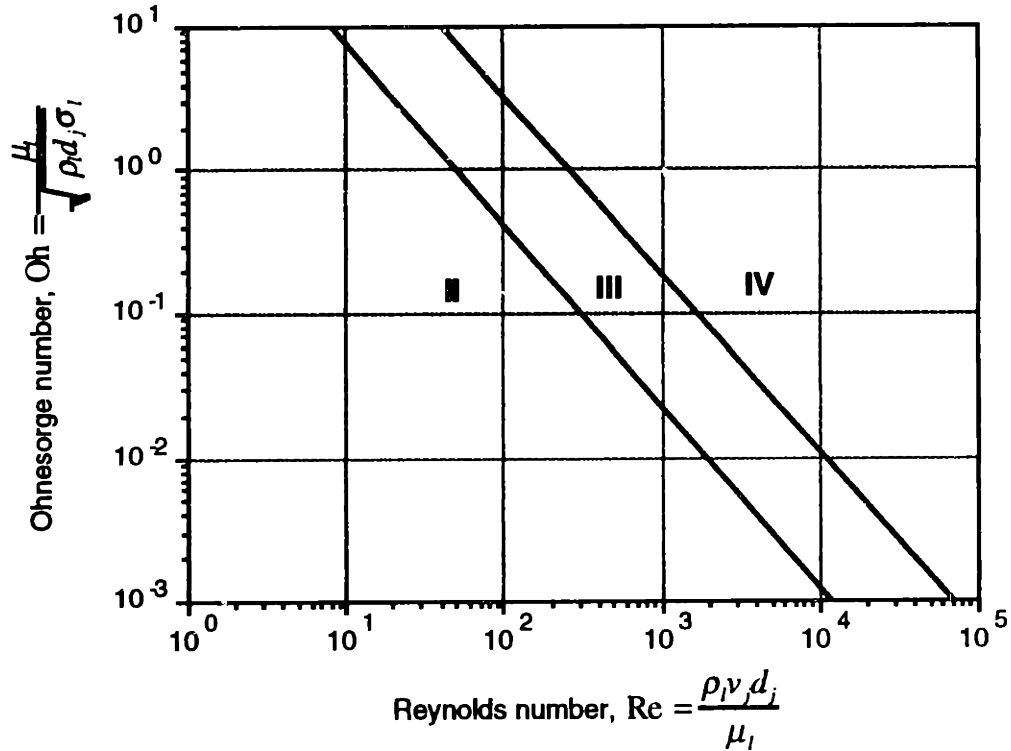


Figure 2.1 Representation of the liquid disintegration with respect to the Reynolds and Ohnesorge numbers.

2.2 Linear Theory

A liquid jet breaks up into a train of droplets because of capillary instability, except when the jet is very viscous or when its surface solidifies before breaking. Figure 2.2 shows a schematic of the break-up of a liquid jet and Figure 2.3 shows the break-up of a molten tin jet.

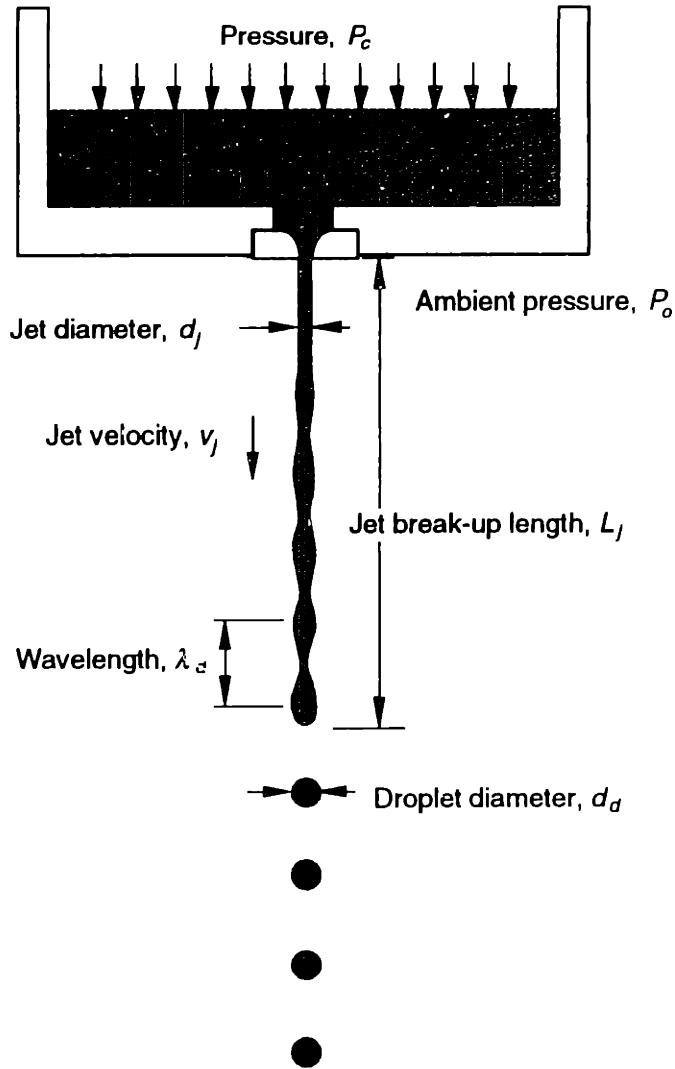


Figure 2.2 Schematic diagram of the break-up of a laminar jet.

The phenomenon of jet break-up due to capillary instability has been a significant research topic for over a century. Rayleigh (1878) developed a linear stability analysis of inviscid laminar jets. Weber (1931) and Lee (1974) further developed the linear analysis and obtained results very similar to those of Rayleigh. Weber, however, included the viscosity effect in his analysis.

Rayleigh postulated that if the jet is perturbed by infinitesimal amounts at the exit of the nozzle, the disturbance grows exponentially with time and sinusoidally with space. The jet radius, r , at any given time is given by:

$$r = a + \delta \exp(qt) \cos\left(\frac{2\pi z}{\lambda}\right), \quad (2.2.1)$$

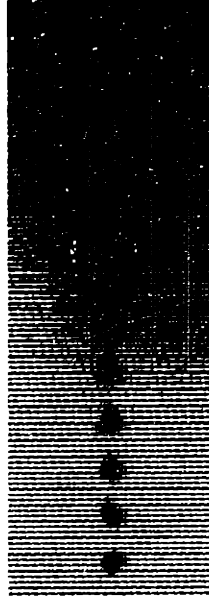


Figure 2.3 Break-up of liquid tin jet. The diameter of orifice used is 100 μm , jet velocity 4.65 m/s, and vibration frequency 11.34 kHz, which is equivalent to the dimensionless wavelength of 4.1. The resulting droplet diameter was 180 μm .

where a is the radius of the nozzle, δ the amplitude of perturbation, q the growth rate factor, t the time, z the distance along the jet axis, and λ the wavelength. The growth factor is determined by the density and surface tension of the liquid, as well as the size of the nozzle. The growth factor determines how fast a neck on the surface of the liquid jet contracts and therefore the jet break-up time and the length, if the jet velocity is known. As described in the previous section, the gravitational effect on the capillary instability of liquid jets is negligible (Ohnesorge, 1936).

Rayleigh used an energy method to calculate the growth factor of inviscid flow. Weber (1931) included the viscosity effect into his analysis and derived the growth factor:

$$q^2 + \frac{3\mu_l \gamma^2}{\rho_l a^2} q = \frac{\sigma_l}{2\rho_l a^3} (1 - \gamma^2) \gamma, \quad (2.2.2)$$

where γ is the dimensionless wave number and is defined as $2\pi a/\lambda (= \pi d_j/\lambda)$.

By solving the quadratic equation for q , differentiating with respect to λ and maximizing equation (2.2.2), the maximum growth rate can be expressed as:

$$q_m = \left\{ \left(\frac{8\rho_l a^3}{\sigma_l} \right)^{1/2} + \frac{6\mu_l a}{\sigma_l} \right\}^{-1} = \sqrt{\frac{\sigma}{\rho d_j^3} \left[\frac{1}{1 + 3\text{Oh}} \right]}. \quad (2.2.3)$$

Thus the growth factor decreases as the density, jet diameter, and viscosity increase, but it increases as the surface tension increases. The dimensionless wavelength, λ/d_j , at which the maximum growth rate occurs is:

$$\frac{\lambda_m}{d_j} = \frac{\lambda_m}{2a} = \pi \sqrt{2 + \frac{3\mu_l}{\sqrt{\rho_l \sigma_l d_j}}} = \pi \sqrt{2 + 3Oh}. \quad (2.2.4)$$

If the viscosity is assumed to be negligible, i.e., $\mu_l = 0$, the result is similar to Rayleigh's (McCarthy and Molly, 1974; Lee, 1974). If the viscosity is zero, equation (2.2.2) becomes:

$$q^2 = \frac{\sigma_l}{2\rho_l a^3} (1 - \gamma^2) \gamma^2, \quad (2.2.5)$$

which is the growth factor by Weber for inviscid flow. Rayleigh's analysis, however, shows the growth factor to be:

$$q^2 = \frac{\sigma_l}{\rho_l a^3} \frac{I_1(\gamma)}{I_0(\gamma)} \gamma (1 - \gamma^2), \quad (2.2.6)$$

where $I_1(\gamma)$ and $I_0(\gamma)$ are modified Bessel functions of the first kind. If the above equation is differentiated and maximized, the maximum growth rate is:

$$q_m = 0.97 \sqrt{\frac{\sigma_l}{\rho_l d_j^3}}, \quad (2.2.7)$$

and the corresponding dimensionless wavelength is:

$$\frac{\lambda_m}{d_j} = 4.508. \quad (2.2.8)$$

Figure 2.4 shows the dimensionless growth factor, $q/\sqrt{\sigma_l \rho_l^{-1} d_j^{-3}}$, as a function of the dimensionless wavelength, λ/d_j , by Rayleigh's analysis and by Weber's analysis for inviscid flow. The results are very similar. As can be seen from the above figure and equations (2.2.4) and (2.2.8), the maximum growth rate occurs when the dimensionless wavelength is 4.508 by Rayleigh's analysis or 4.443 by Weber's analysis for inviscid flow.

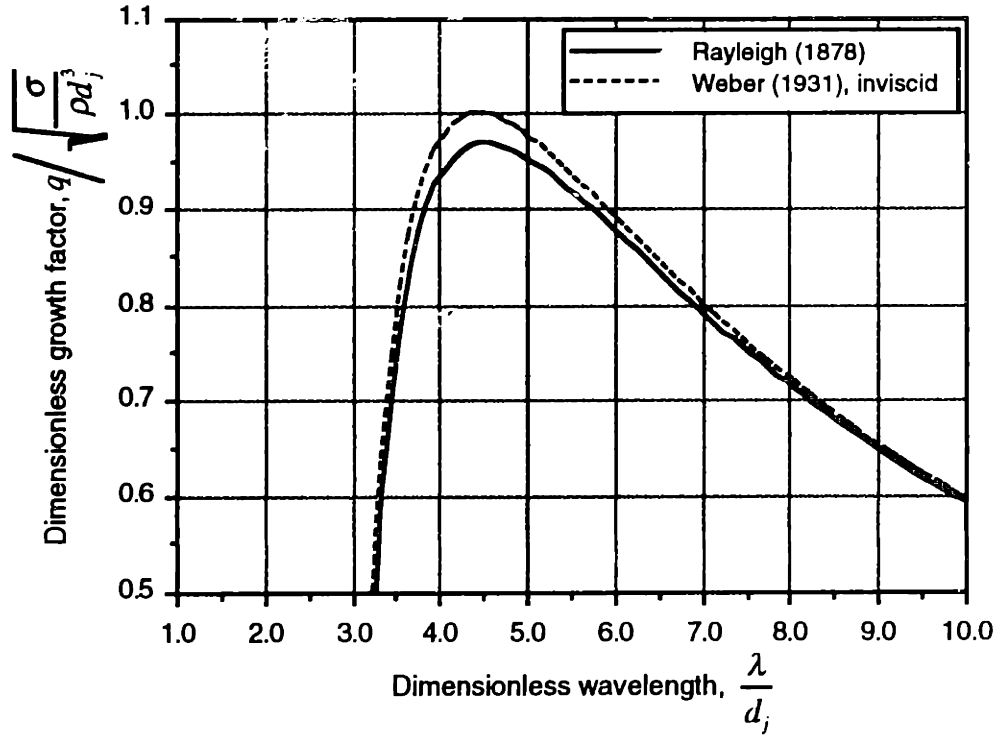


Figure 2.4 Dimensionless growth factor versus dimensionless wavelength by Rayleigh's and Weber's inviscid flow analyses. (Lee, 1974)

The time required to break the jet can be obtained from equation (2.2.1) when the jet radius, r , becomes zero, that is, $a = \delta \exp(q_m t)$ and is given by (McCarthy and Molly, 1974; Heinzl and Hertz, 1985):

$$t = \frac{\ln(a/\delta)}{q_m}. \quad (2.2.9)$$

The length at which the jet breaks into droplets can be obtained from the velocity:

$$L_j = \frac{v_j}{q_m} \ln\left(\frac{a}{\delta}\right). \quad (2.2.10)$$

Substituting for q_m , from equation (2.2.3), into equation (2.2.10) the jet break-up length, L_j becomes:

$$L_j = \ln\left(\frac{a}{\delta}\right) v_j \left[\left(\frac{8\rho_l a^3}{\sigma_l} \right)^{1/2} + \frac{6\mu_l a}{\sigma_l} \right] = \ln\left(\frac{d_j}{2\delta}\right) v_j \left[\left(\frac{\rho_l d_j^3}{\sigma_l} \right)^{1/2} + \frac{3\mu_l d_j}{\sigma_l} \right]. \quad (2.2.11)$$

Equation (2.2.11) can now be rewritten in the dimensionless form as:

$$\frac{L}{d_j} = \ln\left(\frac{a}{\delta}\right) \left[\sqrt{\text{We}} + \frac{3\text{We}}{\text{Re}} \right], \quad (2.2.12)$$

where We is the Weber number and is defined by:

$$\text{We} = \frac{\rho_l v_j^2 d_j}{\sigma_l}. \quad (2.2.13)$$

The logarithmic term can be obtained through experiments by correlating the square-bracketed terms, i.e., Reynolds and Weber numbers, to the ratio of jet break-up length to the jet diameter as shown in equation (2.2.12). Haenlein (1932) performed many experiments and found the logarithmic term to be 12. Grant and Middleman (1966) reported an average value of 13.4. The logarithmic value cited in the literature must be used with discretion since the nozzle design, i.e., diameter and aspect ratio (nozzle length to diameter), inlet and outlet conditions of the nozzle, and the liquid materials change the results. However, it can be safely assumed that the jet break-up length decreases as the amplitude of disturbance increases.

Figure 2.5 shows the jet break-up length calculated by equation (2.2.11) for various materials, assuming that the jet diameter is 100 μm and the jet velocity is 5 m/s. The properties of liquid metals at their freezing temperature and of water at 298 K are used. The logarithmic term is assumed to be 12 as obtained by Haenlein (1932).

As can be seen in Figure 2.5, the break-up length seems to decrease with an increase in the melting temperature of materials. For molten metals, the first term in the square bracket of equation (2.2.11) is greater than the second term by two orders of magnitude. Thus the second term is negligible, which means the Ohnesorge number is very small for molten metals, and the viscosity effect on the break-up of molten metal jets is negligible. However, this is not necessarily true when the surface of a molten metal jet oxidizes to form an oxide layer. This situation will be discussed in Chapters 6 and 7.

As listed in Table 2.2, glycerin is a very viscous liquid, which implies that it takes a very long time for instability to grow on the surface of glycerin jet. In other words, a glycerin jet would be very stable. The Ohnesorge number is a good indicator of jet stability. For example, the Ohnesorge number for glycerin is four orders of magnitude greater than that of any other material listed in the table. Equation (2.2.2) can be modified to obtain the growth factor as:

$$q = \sqrt{\frac{\sigma}{\rho d_j^3}} \left[-6(\text{Oh})\gamma^2 + \sqrt{36(\text{Oh}^2)\gamma^4 + 4(1-\gamma^2)\gamma^2} \right]. \quad (2.2.14)$$

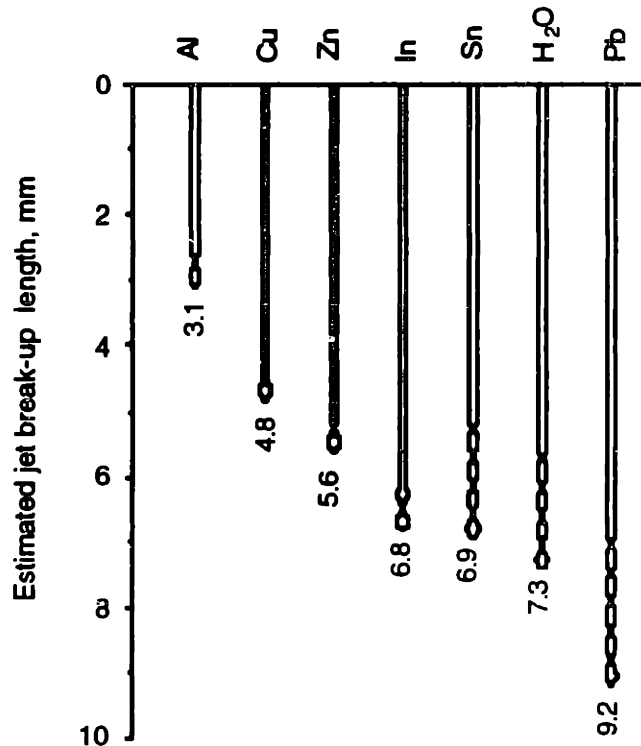


Figure 2.5 Estimated jet break-up length of various materials based on the orifice diameter of 100 μm and jet velocity of 5 m/s. No material changes during the run due to oxidation are assumed. Weber's equation is used.

Table 2.2 Properties of various materials

Material	Jet break-up length (mm)	Density (kg/m^3)	Surface tension (N/m)	viscosity (Pa-s)	Ohnesorge number	Melting temperature (K)
Aluminum	3.1	2385	9.14×10^{-1}	1.30×10^{-3}	2.8×10^{-3}	933.4
Copper	4.8	8000	1.29	4.00×10^{-3}	3.9×10^{-3}	1357.8
Zinc	5.6	6575	7.82×10^{-1}	3.85×10^{-3}	5.4×10^{-3}	692.6
Indium	6.8	7023	5.66×10^{-1}	1.89×10^{-3}	3.0×10^{-3}	429.4
Tin	6.9	7000	5.44×10^{-1}	1.85×10^{-3}	3.0×10^{-3}	505
Water	7.3	1000	7.28×10^{-2}	1.00×10^{-3}	11.7×10^{-3}	
Lead	9.2	10678	4.68×10^{-1}	2.65×10^{-3}	3.7×10^{-3}	600.5
Glycerin	432.2	1260	6.33×10^{-2}	1.49	16.7	

Note: The properties of liquid metals are at their freezing temperatures. The Ohnesorge number is calculated assuming jet diameter of 100 μm . Source: Smithells Metals Reference Book, 6th Edition, 1983.

Figure 2.6 shows the growth factor with respect to the dimensionless wavelength for various Ohnesorge numbers. Clearly, the growth factor for glycerin is very small since the Ohnesorge number is large.

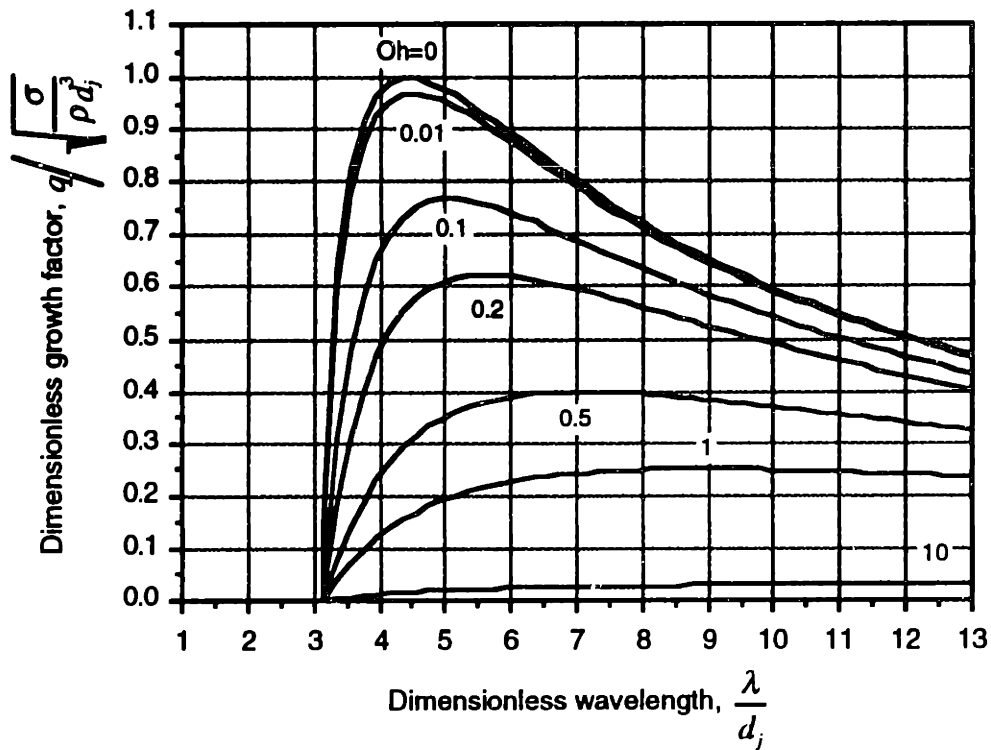


Figure 2.6 Dimensionless growth rate versus dimensionless wavelength for various Ohnesorge numbers.

2.3 The Formation of Satellites

The previous section described the break-up behavior of liquid jets by linear theories. The break-up behavior of a continuous laminar jet, however, is highly non-linear. For example, the linear theories developed by Rayleigh (1878) for inviscid liquids and by Weber (1931) for viscous liquids do not explain the formation of satellites, the small droplets formed between large droplets. In recent decades, non-linear stability analyses have been developed to explain the phenomenon of satellite formation (Yuen, 1968; Goedde and Yuen, 1970; Rutland and Jameson, 1971; Keller et al., 1973; Lafrance, 1975; Sterling and Sleicher, 1975; Taub, 1976; Chaudhary and Maxworthy, 1980a & 1980b; Chaudhary and Redekopp, 1980).

Satellite formation must be suppressed during the UDS process or any other process that uses Rayleigh instability since it produces non-uniform droplets. If satellite

formation is not suppressed or at least controlled, mono-sized droplets are not produced, compromising the process. Random size droplets change the mass flux and thermal state of droplets in the UDS process since the satellites solidify faster than the larger uniform droplets. Moreover, because the ratio of the electrostatic force to the inertia force of the small electrostatically charged droplets is higher than that of larger ones, the smaller particles fly off the centerline of the jet, resulting in non-uniform mass flux in the spray. If the size of the satellites is close to that of the regular uniform droplets, however, the problems may not be significant. Nonetheless, it is desirable to eliminate satellite formation as far as possible.

Satellite formation also poses a serious problem for producing uniform droplets with tight dimensional tolerances. It can, however, be eliminated by imposing the right frequency (Passow, 1992) or by increasing the amplitude of perturbation (Shutts, 1995) in the orifice area. Non-linear theory involves complex mathematical formulation, far beyond the scope of the present investigation, and therefore will not be treated in this thesis in detail.

2.4 Effects of Material Properties on the Behavior of Jet Break-Up

The properties of liquids, such as density, surface tension, and viscosity, greatly affect the behavior of jet break-up. As can be seen in equation (2.2.3), the rate of neck growth increases with the increase of surface tension; the liquid jets breaks faster into droplets when the value of surface tension is high. On the contrary, high viscosity retards the jet break-up process and thus has a stabilizing effect.

In this section, it is assumed that the surface of the molten tin jet does not transform into a solid metal oxide or any other surface film and cover the jet. If a solid oxide film covers the surface of the jet, the surface tension force has to be strong enough to collapse or crack the oxide sheath to break the jet into droplets. Thus the ideas presented in this section will not hold with a solid oxide or metallic surface layer. The possible mechanisms and consequence of oxidation to jet break-up and droplet formation are discussed in Chapter 6 in greater detail.

2.4.1 Role of surface tension

Surface tension is the driving force for capillary instability of laminar jets. It is therefore important to know the quantitative value of surface tension at the time of break-up. The surface tension of molten metals changes with temperature and oxygen partial pressure. It decreases as the temperature increases. For example, the temperature dependence of surface tension, σ , of liquid tin, whose freezing temperature is 505 K, follows the relationship (Brandes, 1983):

$$\sigma = 544 - 0.07(T - T_m) \text{ mN/m}, \quad (2.4.1)$$

where T is the temperature and T_m is the melting temperature. Another relationship is given by Taimatsu and Sangiori (1992) as:

$$\sigma = 570 - 0.108(T - T_m) \text{ mN/m}. \quad (2.4.2)$$

The typical operating temperatures for tin range from 543 to 623 K. The surface tension therefore has a weak dependence on temperature. If equation (2.4.1) is used, the surface tensions of tin at 543 and 623 K are 541 and 536 mN/m, respectively. Thus, the variation in the surface tensions due to temperature changes — for example at 505 and 623 K — is only 8 mN/m, which is less than 2%. Furthermore, the difference between the surface tensions given by the two relationships, those of Brandes (1983) and Taimatsu and Sangiori (1992), is only 5%.

Equation (2.2.11) can be used to estimate the sensitivity of jet break-up length to the change in surface tension, and can be written as:

$$\Delta L_j = \ln\left(\frac{d_j}{2\delta}\right) v_j \left[0.5 \left(\frac{\rho d_j^3}{\sigma^3}\right)^{1/2} + \frac{3\mu d_j}{\sigma^2} \right] \Delta\sigma, \quad (2.4.3)$$

where the logarithmic term is assumed to be constant. As shown in Figure 2.5, the break-up length of pure tin is about 6.9 mm, if the logarithmic term is assumed to be 12 and the jet diameter is 100 μm , jet velocity 5 m/s, density 7000 kg / m^3 , viscosity 1.85 mPa-s, and surface tension 544 mN/m. Even if the surface tension decreases by 27 mN/m (about 5%), the jet break-up length increases only by 0.2 mm, or about a 3% change in the length. Thus, the decrease in surface tension due to an increase in temperature has a negligible effect, unless of course the molten tin jet solidifies before it breaks up into droplets.

The surface tension of molten tin decreases as the partial pressure of oxygen is increased. Taimatsu and Sangiorgi (1992) measured the surface tension of liquid tin as a function of oxygen partial pressure at 1073 K. Its dependence on the oxygen partial pressure is given as:

$$\sigma = 377 - 3.07 \ln P_{O_2} \frac{\text{mN}}{\text{m}}, \quad (2.4.4)$$

where P_{O_2} is the oxygen partial pressure in Pa. The above experimental relationship was obtained for the oxygen partial pressure of 6.9×10^{-13} to 3.1×10^{-17} Pa. In the UDS process, the molten tin is typically sprayed at around 520 K into a spray chamber at the gauge pressure of 35 kPa (5 psig) with the oxygen content of 5 ppm, which translates into a partial pressure of about 0.7 Pa. The conditions under which the relationship of equation (2.4.4) was obtained are different than the typical operating conditions for the UDS process. Using the above equation to determine the surface tension at high partial pressures would be inappropriate, but can be used for a rough estimate. The estimated surface tension at the oxygen partial pressure of 0.7 Pa (typical UDS operating conditions) is about 378 mN/m. The surface tension would decrease to about 347 mN/m at the oxygen partial pressure of 0.02 MPa, which would be the case if the molten tin is sprayed into an atmospheric environment and, of course, if the metal does not oxidize.

In the absence of a good model to estimate surface tension, the effect of oxygen partial pressure on the jet break-up length can be approximated by assuming that the surface tension decreases at most by a factor of 2 from its value at the melting temperature, when the molten tin jet is exposed to an atmospheric environment. The jet break-up length would then increase by about 2 mm using the sensitivity analysis shown in equation (2.4.3). The tin jet should break within 10 mm even though the liquid jet is exposed to an atmospheric environment. Furthermore, a liquid tin droplet at an initial temperature of 553 K needs to travel vertically downward about 200 to 300 mm to solidify completely. Although the decrease in surface tension increases the jet break-up length, the jet should remain liquid within the predicted break-up length. When the liquid tin is sprayed into the ambient air, however, the jet forms fibers. Thus, the formation of fibers cannot be explained by the decrease in the surface tension value, which may be due to the increase of oxygen partial pressure.

2.4.2 Role of viscosity

High viscosity retards the break-up of a liquid jet as shown in equation (2.2.11). For example, because of their high viscosity, jets of glycerin and polymeric fluids take longer to break than an inviscid water jet does. However, the viscosity needs to increase by more than two orders of magnitude to have any effect on the jet break-up length for molten metals, for the surface tension term is greater than the viscous term by two orders of magnitude.

The viscosity, μ , of liquid metals depends on the temperature (Brandes, 1983):

$$\mu = \mu_o \exp\left(\frac{E}{RT}\right), \quad (2.4.5)$$

where μ_o is the viscosity at the freezing temperature, E the activation energy, R the gas constant, and T the temperature. For example, the viscosity of liquid tin at 505 K is 1.85 mPa-s, and it is 1.45 mPa-s at 623 K, as listed in Table A.3 in Appendix A. The viscosity, therefore, increases by about 0.40 mPa-s as the molten tin cools from 623 to 505 K.

Equation (2.2.11) can be used to find the sensitivity of jet break-up length due to the change in viscosity. It can be written as:

$$\Delta L_j = \ln\left(\frac{d_j}{2\delta}\right) v_j \left[\frac{3d_j}{\sigma}\right] \Delta\mu. \quad (2.4.6)$$

Thus, if the viscosity increases by 0.40 mPa-s, the jet length would increase to 0.013 mm, which is very small compared with a typical break-up length of about 10 mm. Within the range of viscosity mentioned above, the jet break-up length should hardly change because of the change in viscosity due to temperature change. Again, this is only true if the jet surface remains liquid.

The effect of surface tension on the jet break-up length is shown in Figure 2.6(a) and the effect of viscosity in Figure 2.6(b), where the jet diameter is assumed to be 100 μm , density 7000 kg/m^3 , jet velocity 5 m/s, and dimensionless wavelength 4.51. The jet length is calculated using equation (2.2.11). As shown in the figures, the jet break-up length remains more or less the same until the viscosity term becomes very large. In the case of pure tin, the viscosity has to increase to about 0.02 Pa-s (about an order of magnitude) to have any appreciable increase in the jet break-up length as shown in Figure 2.6(b). The jet break-up length doubles when the viscosity term is equal to the surface tension term, i.e., when the viscosity of molten jet becomes 0.2 Pa-s.

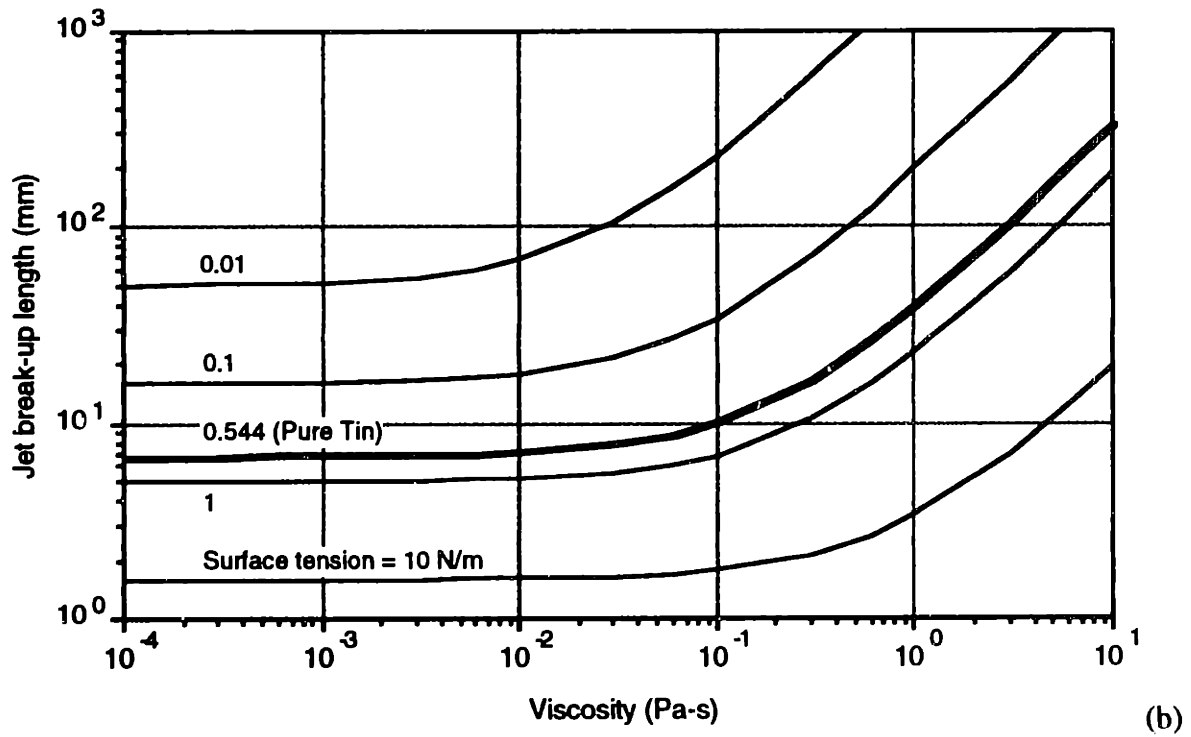
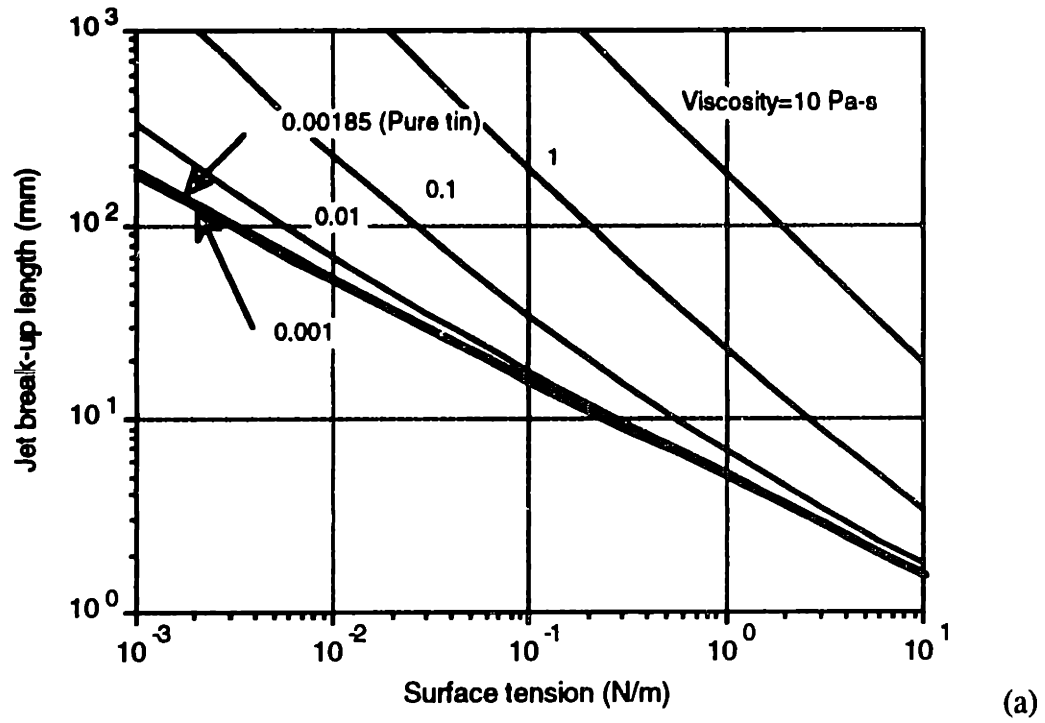


Figure 2.7 Effect of surface tension and viscosity on the jet break-up length based on the orifice diameter of $100\ \mu\text{m}$, density $7000\ \text{kg/m}^3$, jet velocity $5\ \text{m/s}$, and dimensionless wavelength 4.51 . Weber's equation is used. (a) Jet break-up length vs. surface tension, (b) Jet break-up length vs. viscosity.

2.5 Behavior of Jet Break-Up in Another Liquid Medium

Thus far, the break-up behavior of laminar inviscid or viscous liquid jets in a vacuum or in a gaseous atmosphere has been discussed. The analysis is more complicated, however, if friction on the jet surface due to aerodynamic drag is not negligible and if the surrounding medium is not air but a liquid.

In this section, the break-up behavior when a liquid jet issues into another fluid environment is discussed. Tomotika (1936) used a linear analysis to evaluate the growth factor, q , utilizing the following boundary conditions at the interface of the two fluids: (i) there is no slippage at the surface of the column; (ii) the tangential stress at the surface of the jet is continuous; and (iii) the difference between the normal stresses inside and outside the jet is due to the interfacial surface tension. These boundary conditions lead to (Tomotika, 1936; McCarthy and Molly, 1974):

$$\begin{vmatrix} I_1(ka) & I_1(k_{1,l}a) & K_1(ka) & K_1(k_{1,r}a) \\ kaI_0(ka) & k_{1,l}aI_0(k_{1,l}a) & -kaK_0(ka) & -k_{1,r}aK_0(k_{1,r}a) \\ \frac{2\mu_l}{\mu_s}k^2I_1(ka) & \frac{\mu_l}{\mu_s}(k^2+k_{1,l}^2)I_1(k_{1,l}a) & 2k^2K_1(ka) & (k^2+k_{1,r}^2)K_1(k_{1,r}a) \\ F_1 & F_2 & F_3 & F_4 \end{vmatrix} = 0, \quad (2.5.1)$$

where $I_n(x)$ and $K_n(x)$ are the modified Bessel functions of the n th order, $I_1'(x)$ and $K_1'(x)$ are the first derivatives of $I_1(x)$ and $K_1(x)$ with respect to x , respectively. The rest of the terms are defined as follows:

$$k_{1,l}^2 = k^2 + \frac{q}{v_l} \quad (2.5.2)$$

$$k_{1,r}^2 = k^2 + \frac{q}{v_s} \quad (2.5.3)$$

$$F_1 = 2i\frac{\mu_l}{\mu_s}k^2I_1'(ka) - \frac{q\rho_l}{i\mu_s}I_0(ka) + \sigma\frac{(k^2a^2-1)}{a^2}\frac{ik}{q\mu_s}I_1(ka) \quad (2.5.4a)$$

$$F_2 = 2i\frac{\mu_l}{\mu_s}kk_{1,l}I_1'(k_{1,l}a) + \sigma\frac{(k^2a^2-1)}{a^2}\frac{ik}{q\mu_s}I_1(k_{1,l}a) \quad (2.5.4b)$$

$$F_3 = 2ik^2 K_1'(ka) + \frac{q\rho_g}{i\mu_g} K_0(ka) \quad (2.5.4c)$$

$$F_4 = 2ikk_{1,g} K_1'(k_{1,g}a) \quad (2.5.4d)$$

Equation (2.5.1) can be reduced for a low viscosity liquid jet in a gas (by neglecting the viscosity of the jet, the viscosity of ambient atmosphere, and the density of the atmosphere) to obtain growth factor similar to that due to Rayleigh. That is:

$$q^2 = \frac{\sigma}{\rho_l a^3} \frac{I_1(ka)}{I_0(ka)} ka(1 - ka^2) . \quad (2.5.5)$$

For cases where the viscosity of the liquid jet cannot be ignored, equation (2.5.1) reduces to:

$$q^2 + \frac{3\mu_l k^2}{\rho_l} q = \frac{\sigma_l}{2\rho_l a^3} (1 - k^2 a^2) k^2 a^2 \quad (2.5.6)$$

This is the same result as obtained by Weber (1931) and McCarthy and Molly (1974). Tomotika then went on to discuss the two limiting cases where $\mu_l/\mu_g \rightarrow \infty$ and $\mu_l/\mu_g \rightarrow 0$. In both cases, he found that the value of growth factor, q , is highest when $ka (= 2\pi a/\lambda) = 0$, which means the wavelength, λ , at which the maximum instability of jet occurs is very large compared with the jet diameter. Tomotika further discussed the case in which the ratio of viscosity is neither infinity nor zero, i.e., the ratio has a finite value but the effect of inertia terms is still negligible. He determined that maximum instability occurs when ka is 0.568 for the case where the ratio μ_l/μ_g equals 0.91 and the corresponding wavelength is $5.53 d_j$. He compared his analytical results with experimental data and found them to be in fair agreement.

Tomotika (1935) also gave the relationship between the value of ka for its maximum instability and the value of μ_l/μ_g , as shown in Table 2.3 and in Figure 2.8. As discussed earlier, ka approaches zero as the viscosity ratio tends to either infinity or zero. The maximum ka occurs when the ratio is about 0.5.

Table 2.3 The relationship between the value of μ_i/μ_s and the value of ka for maximum instability and the corresponding wavelength

μ_i/μ_s	ka	λ
0	0	∞
0.001	0.257	$12.22 d_j$
0.01	0.415	$7.57 d_j$
0.1	0.573	$5.48 d_j$
0.5	0.584	$5.38 d_j$
0.91	0.568	$5.53 d_j$
1	0.563	$5.58 d_j$
5	0.486	$6.46 d_j$
10	0.409	$7.68 d_j$
20	0.353	$8.90 d_j$
100	0.243	$12.93 d_j$
∞	0	∞

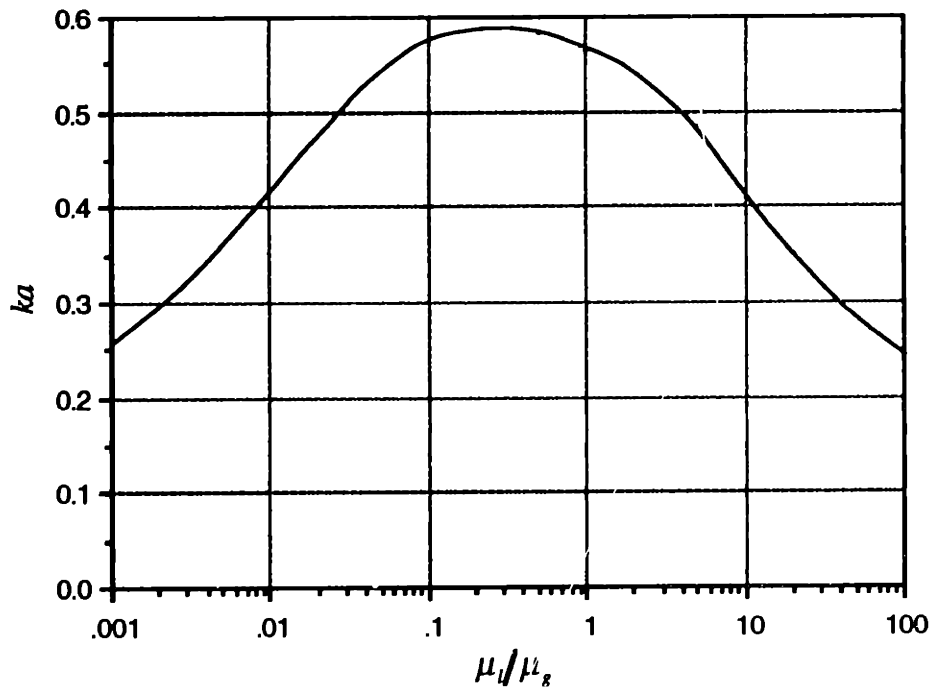


Figure 2.8 The relationship between the value of μ_i/μ_s and the value of ka for maximum instability and the corresponding wavelength.

2.6 Conclusions

In this chapter, the linear theories presented by Rayleigh (1878) and Weber (1931) on the break-up behavior of liquid jets have been discussed. As mentioned in Chapter 1, researchers have shown that water (Mason et al., 1963; Schneider and Hendricks, 1964; Lindblad and Schneider, 1965; Hendricks and Babil, 1972), and other non-oxidizing liquids, such as sodium nitrite (Erin and Hendricks, 1968) and ink used in ink jet printing technology (Sweet, 1965; Kamphoefner, 1972; Fillmore et al., 1977), more or less follow the relationships presented by Rayleigh and Weber. Also discussed in this chapter is the formation of satellites, which can be explained only by a non-linear theory. The break-up of laminar liquid jets when they are sprayed into another liquid medium is also discussed. All these theories are based on non-reacting atmospheres. Chapter 4 will present the experimental results on the break-up behavior of molten metal jets as they are sprayed into an environment with sufficiently low oxygen concentrations.

Nomenclature

a	initial jet radius
d_d	diameter of droplets
d_j	initial jet diameter, $2a$
d_o	diameter of orifice
E	activation energy
$F_{1,2,3,4}$	constants listed in equations (2.5.4a) through (2.5.4d)
f	frequency of imposed vibration
$I(x)$	modified Bessel function
$I'(x)$	derivative of $I(x)$
$K(x)$	modified Bessel function
$K'(x)$	derivative of $K(x)$
k	wave number, $\frac{2\pi}{\lambda}$
$k_{1,g}$	constant listed in equation (2.5.3)
$k_{1,l}$	constant listed in equation (2.5.2)
L_j	jet break-up length
ΔL_j	change in jet break-up length

Oh	Ohnesorge number, $\frac{\mu}{\sqrt{\rho d \sigma}}$
P_c	pressure of crucible
P_o	pressure of chamber
ΔP	pressure difference, $P_c - P_o$
P_{O_2}	partial pressure of oxygen
q	growth rate factor
q_m	maximum growth factor
R	universal gas constant
Re	Reynolds number, $\frac{\rho v d}{\mu} = \frac{v d}{\nu}$
r	radius of jet, instantaneous
T	temperature
T_m	melting temperature of a material
t	time
v_j	jet velocity
We	Weber number, $\frac{\rho v^2 d}{\sigma}$
z	distance along the jet axis
γ	dimensionless wave number, $ka = \frac{2\pi a}{\lambda} = \frac{\pi d_j}{\lambda}$
δ	amplitude of disturbance applied to nozzle area
λ	wavelength, $\frac{v_j}{f}$
λ_m	maximum wavelength at which the maximum growth rate occurs
μ	viscosity
μ_s	viscosity of surrounding medium
μ_l	viscosity of liquid jet
μ_o	viscosity of a material at its melting temperature
$\Delta\mu$	change in viscosity
ν	kinematic viscosity, $\frac{\mu}{\rho}$
ν_s	kinematic viscosity of surrounding medium
ν_l	kinematic viscosity of liquid jet
π	Pi, 3.14159
ρ_s	density of surrounding medium

ρ_l density of liquid jet
 σ surface tension
 σ_l surface tension of liquid
 $\Delta\sigma$ change in surface tension

Chapter 3 **TRAJECTORY AND HEAT TRANSFER OF DROPLETS**

3.1 Introduction

The previous chapter addressed the phenomenon of jet break-up. This chapter discusses the jet velocity, droplet trajectory, and solidification of droplets. These parameters have significant effects on the mass flux and thermal state of droplets. Once uniform droplets have been formed from the continuous laminar jet, it is imperative to keep them mono-sized since the merging of droplets results in non-uniform droplets. However, the droplets tend to merge as they travel downward since the leading droplets experience more drag force than the trailing droplets. To prevent merging, they are charged electrostatically by induction charging as shown in Figure 3.1. The charged droplets in a aligned single stream are susceptible to lateral instability, which changes the train of droplets into droplet sprays. This chapter also discusses the drag force which affects the trajectory of droplets. The solidification of droplets with the assumption of a Newtonian cooling is discussed as well.

3.2 Jet Velocity

Jet diameter is an important parameter in determining the size of droplets, which itself is a significant input condition to the UDS process. The magnitude of the jet diameter also determines the minimum velocity a jet has to sustain for a continuous laminar flow. Otherwise, the flow will be drop-wise where the gravitational effect is significant, as discussed in Section 2.1. Lindblad and Schneider (1965) and Stricker and Sofer (1991) state that the minimum jet velocity, $v_{j,\min}$, needed to form a liquid jet from a capillary tube is:

$$v_{j,\min} = \sqrt{\frac{8\sigma}{\rho_l d_j}}, \quad (3.2.1)$$

where ρ_l is the liquid density, σ the surface tension, and d_j the jet diameter. Since the pressure applied to the crucible affects the jet velocity, it has to be higher than the minimum jet velocity.

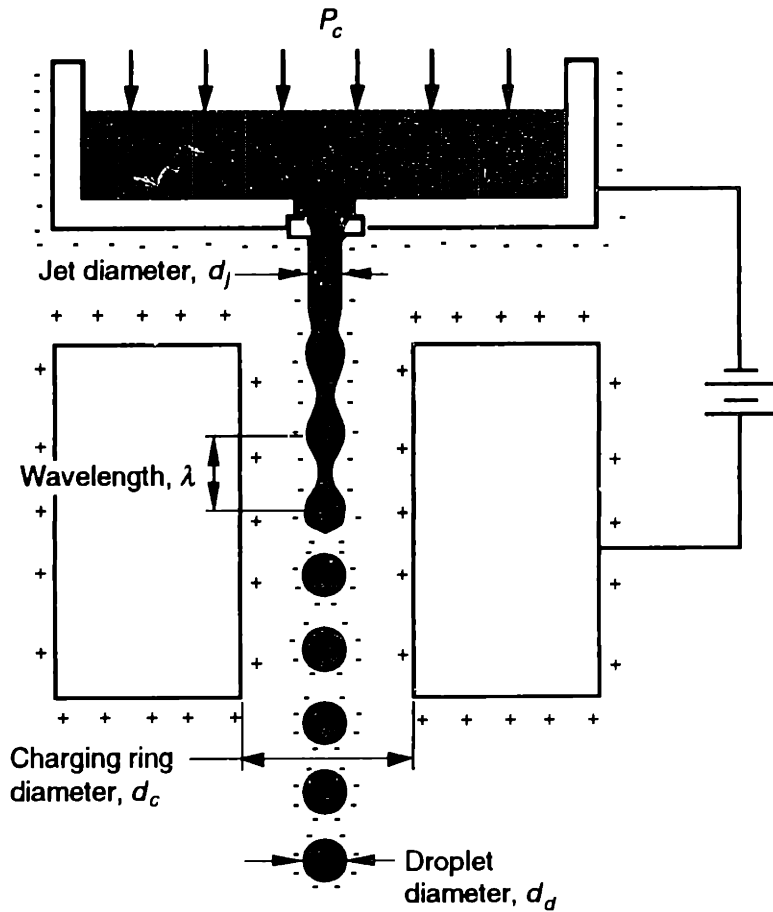


Figure 3.1 Droplet charging by the induction method.

One of the convenient ways of measuring the jet velocity of a liquid is to measure the mass flow rate. The mass flow rate, \dot{m} , depends on the liquid density, jet velocity, and the cross-sectional area of the orifice, A_c , through which the fluid exits. Assuming the jet diameter equals the orifice diameter, the mass flow rate is given by:

$$\dot{m} = \rho_l v_j A_c = \rho_l v_j \left(\frac{\pi d_j^2}{4} \right). \quad (3.2.2)$$

Thus, the jet velocity, v_j , can be calculated by measuring the mass flow rate with:

$$v_j = \frac{4\dot{m}}{\pi d_j^2 \rho_l}. \quad (3.2.3)$$

The jet velocity measured by discharged weight can be compared with the jet velocity by measuring the wavelength, λ_d , of the train of uniform droplets. Assuming that

one droplet forms for every perturbation (i.e., wavelength) applied at a certain frequency f , the measured wavelength can be used to predict the jet velocity by:

$$v_j = \lambda_d \cdot f. \quad (3.2.4)$$

The jet velocities obtained by measuring the discharged weight and the wavelength from the monitor can also be compared with the theoretical jet velocity using the Bernoulli's equation, neglecting the gravitational effect and the friction due to flow restriction at the entrance area of an orifice. The theoretical jet velocity, $v_{j,theo}$, is then given by:

$$v_{j,theo} = \sqrt{\frac{2 \cdot \Delta P}{\rho_l}}, \quad (3.2.5)$$

where ΔP is the pressure difference between the crucible and the spray chamber, or the ejection pressure. The actual jet velocity, v_j , can be written as:

$$v_j = C_{noz} \sqrt{\frac{2 \cdot \Delta P}{\rho_l}}, \quad (3.2.6)$$

where C_{noz} is the discharge coefficient of the flow through the nozzle. The discharge coefficient is due to the friction of the flow through the nozzle as well as to the surface tension of the liquid. Experimental data by Passow (1992) showed that C_{noz} is 0.94 and 0.92 for 100 μm and 45 μm orifice diameters, respectively, assuming that the density of Sn-40 wt.% Pb is 8120 kg / m^3 .

Another way of estimating the jet velocity is to measure the diameter of the droplet (Tyler, 1933; Lindblad and Schneider, 1965; Stricker and Sofer, 1991) assuming that a single droplet forms for every perturbation frequency. It further can be assumed that the volume of a cylinder (a columnar jet) with a length of λ_d and the volume of a resulting droplet are the same (when no satellites form between the main droplets). The volume of the cylinder, V_{cyl} , can be written as:

$$V_{cyl} = \left(\frac{\pi d_j^2}{4} \right) \cdot \lambda_d, \quad (3.2.7)$$

where λ_d is the wavelength corresponding to the perturbation frequency. The cylinder is unstable and will form a spherical droplet due to surface tension. The volume of a spherical droplet with a diameter, d_d , is:

$$V_{sph} = \frac{\pi}{6} d_d^3 . \quad (3.2.8)$$

From equations (3.2.7) and (3.2.8), the resulting droplet size can be written as:

$$d_d = d_j \left(1.5 \frac{\lambda_d}{d_j} \right)^{1/3} . \quad (3.2.9)$$

Typically, dimensionless wavelengths, λ_d/d_j , of 3.5 to 7 (as shown in Table 1.1) have been used to produce uniform powders. The droplet diameter therefore can be varied as:

$$1.74 < \frac{d_d}{d_j} < 2.19 . \quad (3.2.10)$$

To estimate the jet velocity from the diameter of a droplet, equation (3.2.9) can be substituted into equation (3.2.4), yielding:

$$v_j = f \cdot d_j \frac{2}{3} \left(\frac{d_d}{d_j} \right)^3 . \quad (3.2.11)$$

3.3 Trajectory of Droplets

Exact prediction of the velocity and trajectory of droplets is important for the control of the UDS process. The initial velocity of the droplets can be obtained using the relationships described in the previous section.

As the droplets travel downward through the gaseous atmosphere, they experience drag force, which attenuates the velocity. The leading droplet experiences a larger drag force than the trailing droplets, resulting in merging of the trailing droplet into the leading droplet. Thus, the droplets lose their mono-sized uniformity. The droplets are electrostatically charged to prevent the merging. As the charged droplets travel downward, they experience lateral instability (Crowley, 1968; Hertz and Månsson, 1972; Passow, 1992). That is, due to the Coulomb force, the charged droplets repel each other and move radially outward to form a spray.

The trajectory of droplets depends on the drag force, the electrostatic repulsive force, and the gravitational force. Thus, the general form of the trajectory can be written as:

$$m_d \mathbf{a} = \mathbf{F}_e + \mathbf{F}_d + m_d \mathbf{g}, \quad (3.3.1)$$

where m_d is the mass of a droplet, \mathbf{a} the acceleration, \mathbf{F}_e the Coulomb repulsion force, \mathbf{F}_d the drag force, and \mathbf{g} the gravitational acceleration.

3.3.1 Electro-repulsion force

The electro-repulsion force due to the Coulomb's law on a droplet is given by:

$$\mathbf{F}_e = q\mathbf{E} = \frac{q}{4\pi\epsilon_0} \sum \frac{q_i \hat{n}}{r_i^2}, \quad (3.3.2)$$

where q is the charge per a droplet, \mathbf{E} the electric field, ϵ_0 the permittivity constant of free space, \hat{n} the directional unit vector, and r_i the distance between the point charges as shown in Figure 3.2 (Hendricks, 1973).

Assuming that all droplets have the same charge, equation (3.3.2) becomes:

$$\mathbf{F}_e = \frac{q^2}{4\pi\epsilon_0} \sum \frac{\hat{n}}{r_i^2}. \quad (3.3.3)$$

The amount of charge per droplet determines how strong the lateral instability should be; as the charge per droplet increases, so the droplets will scatter radially outward from the centerline of the stream. Thus, the charging amount can be used to vary the mass flux and thermal state of droplets. The charge per droplet is determined by the voltage applied to the charging plate, the droplet diameter, and the slot configuration of the charging plate. When the break-up of laminar jets occurs in the slot, a charge is induced on the surface of droplets. Charging of droplets using this method is known as the induction charging method. The material must be electrically conductive in this charging method. This particular method has been used in ink jet technology (Sweet, 1965; Hertz and Månsson, 1972) and the UDS manufacturing process (Passow, 1992; Passow et al., 1993; Abel 1994). If an electrically non-conductive material such as wax or polymer must be charged, the corona charging method is used.

Figure 3.1 shows the schematic for the charging of droplets. Assuming that the jet and charging plate are the cylindrical capacitor, the capacitance, C , of the capacitor can be expressed as:

$$C = \frac{q}{V} = \frac{1}{2\pi\epsilon_0} \frac{\lambda_d}{\ln(d_c/d_j)}, \quad (3.3.4)$$

where q is the charge per droplet, V the voltage across the capacitor, ϵ_0 the permittivity constant of free space, λ_d the wavelength, and d_c the diameter of the hole in the charging plate. To calculate the charge on the droplets, the above equation can be re-written as:

$$q_d = \frac{1}{2\pi\epsilon_0} \frac{\lambda_d}{\ln(d_c/d_j)} V. \quad (3.3.5)$$

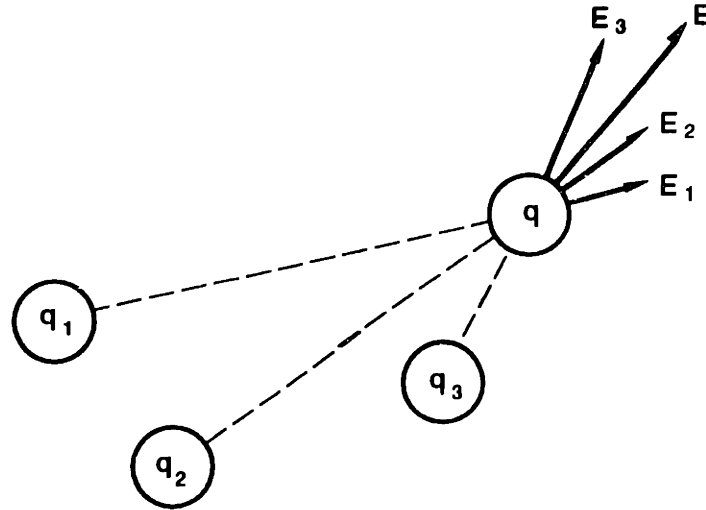


Figure 3.2 The resultant field E as the sum of the fields due to several point charges.

3.3.1 Drag force

The drag force is defined as:

$$\mathbf{F}_d = C_d (\rho_l - \rho_g) \frac{\pi d_d^2}{4} \frac{|\mathbf{v}|\mathbf{v}}{2}, \quad (3.3.6)$$

where C_d is the drag coefficient, ρ_l the density of liquid, ρ_g the density of air, d_d the diameter of the droplet, and \mathbf{v} is the relative velocity of the droplet with respect to the air. Since the density of droplet is much greater than that of the surrounding gas (i.e., $\rho_l \gg \rho_g$), equation (3.3.6) becomes:

$$\mathbf{F}_d = C_d \rho_l \frac{\pi d_d^2}{4} \frac{|\mathbf{v}|\mathbf{v}}{2}. \quad (3.3.7)$$

The drag coefficient is given by (Mathur et al., 1989):

$$C_d = 0.28 + \frac{6}{\sqrt{\text{Re}}} + \frac{21}{\text{Re}}. \quad (3.3.8)$$

The Reynolds number is defined as:

$$\text{Re} = \frac{\rho_g |v| d_d}{\mu_g}, \quad (3.3.9)$$

where ρ_g and μ_g are the density and viscosity of gas, respectively. Equation (3.3.8) is applicable for $0.1 < \text{Re} < 4000$.

Equation (3.3.8) represents the drag coefficient for a single sphere moving in an otherwise still air, where the distance between the center of two neighboring droplets, L , is much greater than the droplet diameter, d_d . The other extreme case is when $L \sim d_d$, where the drag coefficient may be assumed to approach the drag coefficient for a long rod, $C_{d,rod}$ (Mulholland et al., 1988; Passow, 1992; Passow et al., 1993; Abel, 1994). That relationship is given as:

$$C_{d,rod} = \frac{0.755}{\text{Re}}. \quad (3.3.10)$$

Mulholland et al. (1988) give the drag coefficient for an aligned stream of uniformly sized droplets, $C_{d,align}$, as

$$C_{d,align} = \left[(C_{d,o+})^{-n} + (C_{d,\infty})^{-n} \right]^{-1/n}, \quad (3.3.11)$$

where $C_{d,o+}$ is the drag coefficient as the ratio of the droplet spacing to the droplet diameter approaches one (i.e., $L/d_d \rightarrow 1$), $C_{d,\infty}$ a coefficient for an isolated droplet as given by the equation (3.3.8), and n an empirical parameter, which was found to be 0.678 ± 0.07 . $C_{d,o+}$ is given as:

$$C_{d,o+} = C_{d,o} + \frac{a}{\text{Re}} \left(\frac{L}{d_d} - 1 \right), \quad (3.3.12)$$

where $C_{d,o}$ is the drag coefficient at $L/d_d = 1$, and a an experimentally determined parameter. The value of a was found to be 43.0 ± 15.4 . Mulholland et al. (1988) further suggest that:

$$C_{d,o} = \left[(C_{d,rod})^{-n} - (C_{d,\infty})^{-n} \right]^{-1/n}. \quad (3.3.13)$$

When the droplets have scattered so that they are at least the radius of a droplet apart from the center line of stream, the drag coefficient for a single sphere, $C_{d,\infty}$, can be used. Otherwise, the adjusted drag coefficient, $C_{d,adj}$, should be used (Passow, 1992). It is given as:

$$C_{d,adj} = \left(1 - \frac{2L}{d_d}\right) C_{d,align} + \frac{2L}{d_d} C_{d,\infty}. \quad (3.3.14)$$

Combining the equations (3.3.1), (3.3.3), and (3.3.6), the equation of motion for a droplet becomes:

$$m\mathbf{a} = \frac{q^2}{4\pi\epsilon_0} \sum \frac{\hat{n}}{r_i^2} + C_d(\rho_l - \rho_s) \frac{\pi d_d^2}{4} \frac{|\mathbf{v}| \mathbf{v}}{2} + m\mathbf{g}. \quad (3.3.15)$$

Using the equation (3.3.15), the trajectory of droplets can be calculated at any given time during flight.

Accurate prediction of the drag coefficient is desired to estimate the rate at which the velocity of droplets change. As will be seen in the next section, velocity controls the convective heat transfer coefficient, which in turn determines the solidification rate of droplets.

3.4 Solidification of Droplets

A solidification model for a spray of droplets was developed by Passow (1992) to predict the solidification rate of droplets. The temperature, T_d , and liquid fraction, x , of droplets determine the thermal state (or enthalpy, H_d) of droplets per unit mass:

$$H_d = C_p(T_d - 298) + x\Delta H_f, \quad (3.4.1)$$

where C_p is the specific heat and ΔH_f the latent heat. Depending on the state of droplets, i.e., liquid or solid, the appropriate specific heat has to be used. For example:

$$H_d = C_{p,l}(T_d - 298) + \Delta H_f, \quad T_d > T_m \quad (3.4.2a)$$

$$H_d = C_p(T_d - 298) + x\Delta H_f, \quad T_d = T_m \quad (3.4.2b)$$

$$H_d = C_{p,s}(T_d - 298), \quad T_d < T_m \quad (3.4.2c)$$

The droplets solidify as they travel downward. Solidification is assumed to take place due to convective and radiative heat transfer. The heat transfer, Q , due to convection and radiation can be stated as (Mathur et al., 1989; Passow, 1992; Abel, 1994):

$$Q = hA_s(T_d - T_g) + \sigma_{SB}\epsilon A_s(T_d^4 - T_g^4), \quad (3.4.3)$$

where h is the convective heat transfer coefficient, A_s the surface area of droplets, T_g the temperature of gas surrounding the droplet (i.e., ambient temperature), σ_{SB} the Stefan-Boltzmann constant, and ϵ the emissivity, which lies between zero and unity. For all real bodies, the emissivity is always less than one. Typically, the radiation term is negligible compared with the convective term under the operating UDS process conditions for low melting temperature metals. The heat loss from the droplets during flight can be expressed as:

$$Q = \frac{mC_p\Delta T}{\Delta t}. \quad (3.4.4)$$

The temperature and liquid fraction change can be obtained by combining equations (3.4.1) through (3.4.4) over the time step Δt .

The Biot number determines whether the temperature distribution in a droplet is uniform. The Biot number, Bi , is defined as the ratio of the heat transfer coefficient for convection at the surface of a droplet to the specific conduction of the solid, and is given by (Ozisik, 1985):

$$Bi = \frac{h}{k_d/d_d}, \quad (3.4.5)$$

where k_d is the thermal conductivity of droplets. The assumption of uniform temperature within the droplet is valid if the specific conduction of the droplet is much larger than the heat transfer coefficient for convection. When the Biot number is less than 0.01, the heat loss from convection is interface-controlled and the convective heat transfer coefficient can be written as (Mathur et al., 1989; Passow, 1992; Abel, 1994):

$$h = \left(\frac{k_g}{d_d}\right) \left(2.0 + 0.6 Re^{1/2} Pr^{1/3}\right) \left(\frac{C_{g,ave}}{C_g}\right)^{0.26}, \quad (3.4.6)$$

where k_g is the thermal conductivity of the surrounding gas, Pr the Prandtl number, C_g the specific heat of the gas at T_g , and $C_{g,ave}$ the specific heat of the gas at $T_{g,ave}$. $T_{g,ave}$ is defined as:

$$T_{g,ave} = \frac{T_d + T_o}{2} . \quad (3.4.7)$$

The specific heat ratio is included to account for the high temperature gradient in the gas immediately surrounding the droplet (Mathur et al., 1989). The Reynolds number of flow over a spherical droplet is defined as:

$$Re = \frac{\rho_g |v| d_d}{\mu_g} . \quad (3.4.8)$$

The Prandtl number is defined is:

$$Pr = \frac{\mu_g C_g}{k_g} . \quad (3.4.9)$$

The convective heat transfer coefficient in the equation (3.4.6) is to calculate the temperature and liquid fraction of droplets at any given time step. Figure 3.3 shows the typical heat transfer coefficient when a 200 μm tin droplet is traveling in a nitrogen environment, assuming an initial temperature of 555 K, an initial velocity of 5 m/s, and an ambient temperature of 298 K. The value of the heat transfer coefficient initially is about 800 $\text{W}/(\text{m}^2 \cdot \text{K})$ and drops steadily to about 700 $\text{W}/(\text{m}^2 \cdot \text{K})$ after traveling 1 m. The decrease in the droplet velocity while the droplet travels in air causes the decrease in the heat transfer coefficient. Thus, the solidification rate of a droplet decreases as the droplet travels downward.

Solidification can be calculated for its rate and thermal state at a given time according to the basic assumptions stated above. The droplets can be estimated to solidify by Newtonian cooling, that is, that there is no temperature gradient across the lumped mass. An assumption of Newtonian cooling is valid only when the Biot number is less than 0.01.

3.4.1 Results of solidification simulations and their implications

Typically, metals are superheated to 50 K above their melting temperatures when they are sprayed in the chamber. Thus, the droplets emanating from the nozzle are cooled

from their superheated state through the liquid-solid state to the solid state. Figure 3.4(a) and (b) shows the solidification of a droplet as it travels downward in a nitrogen environment at 298 K. Figure 3.4(a) shows the temperature change and Figure 3.4(b) shows the liquid fraction with respect to the flight distance. The droplet is pure tin with a 200 μm diameter, an initial temperature of 555 K (50 K above its melting temperature), and an initial velocity of 5 m/s. As can be seen in Figure 3.4(a), the latent heat extraction accounts for the most of the solidification time (or distance)

Figures 3.5 and 3.6 show the time and the flight distance needed to completely solidify Sn-38 wt.% Pb droplets with 200, 400, 600, and 800 μm in diameters at various initial droplet velocities. As may be expected, the larger droplets require more time and distance to solidify since more heat has to be extracted. As shown in Figure 3.5, the solidification time for a droplet with a given diameter decreases with the increase of the initial droplet velocity. The increase in the droplet velocity causes the Reynolds number to increase and, thus, the heat transfer rate coefficient of a droplet increases as can be seen in equation (3.4.6).

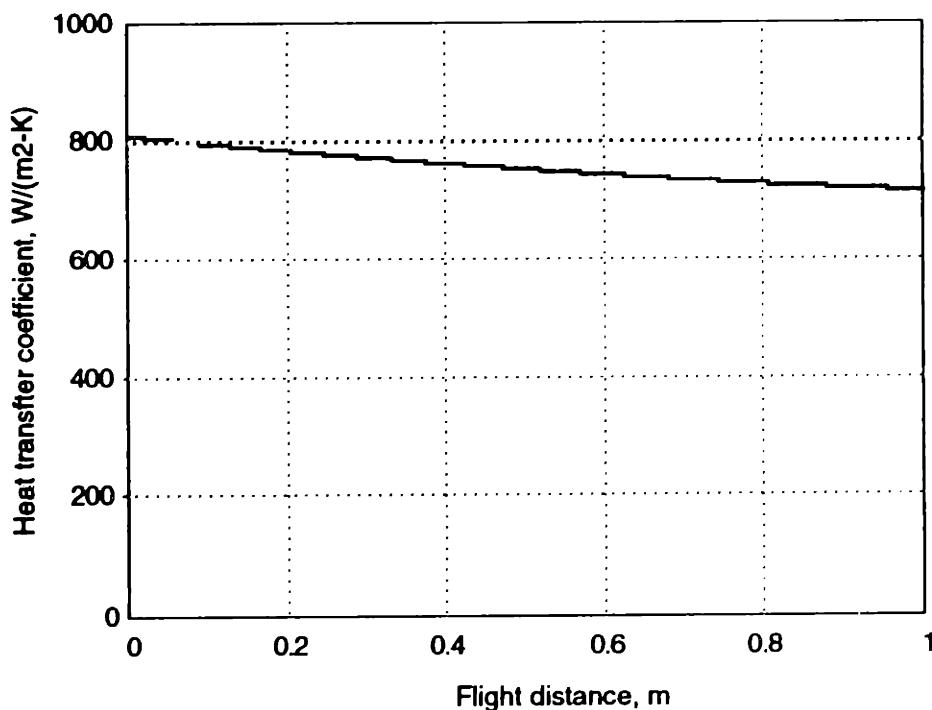


Figure 3.3 Typical heat transfer coefficient of a droplet assuming a pure tin droplet with a diameter of 200 μm , initial velocity of 5 m/s and initial temperature of 555 K. The cooling medium is nitrogen at 298 K.

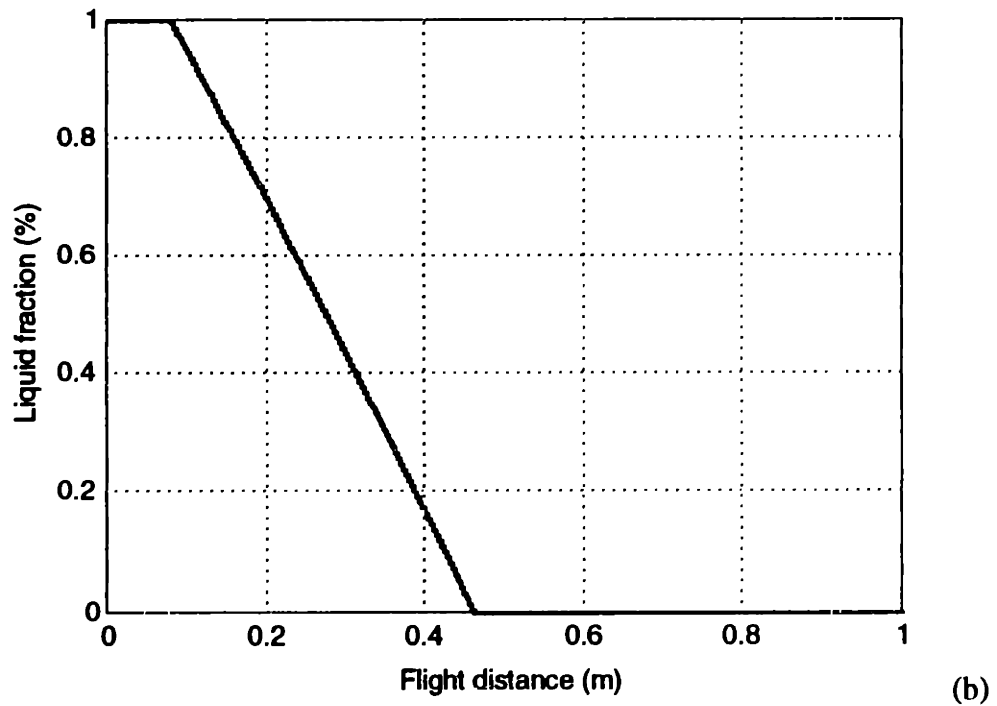
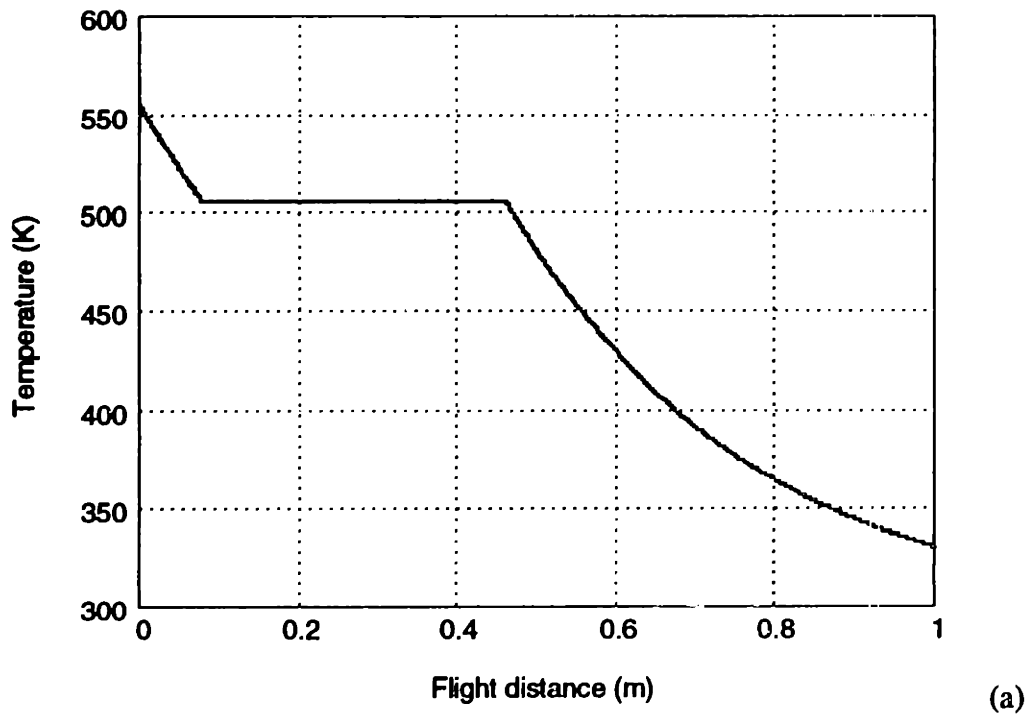


Figure 3.4 Typical solidification curves for droplets. (a) droplet temperature versus distance, (b) liquid fraction of droplet versus distance. The results of solidification simulations based on a droplet diameter of 200 μm , an initial velocity of 5 m/s, and an initial temperature of 555 K are shown in these figures. The cooling medium is nitrogen. The material is pure tin.

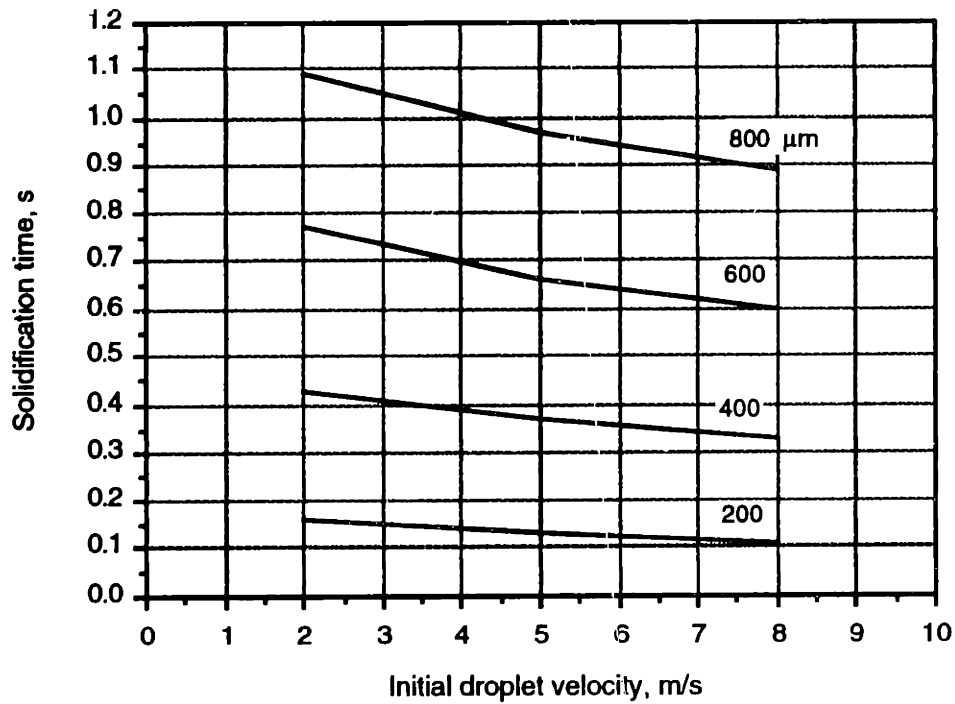


Figure 3.5 The solidification time of Sn-38 wt.% Pb droplets of various sizes in a nitrogen environment. The initial temperature of the droplet is 508 K.

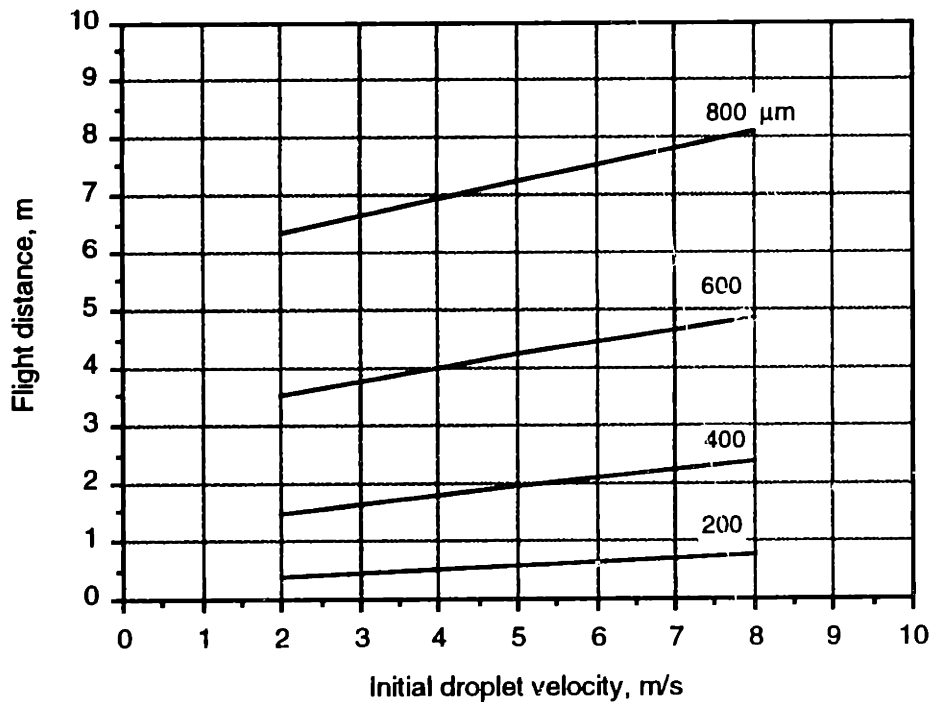


Figure 3.6 The flight distance of Sn-38 wt.% Pb droplets of various sizes in a nitrogen environment. The initial temperature of the droplet is 508 K.

However, the flight distance also increases as a result of the increase in the initial velocity, as shown in Figure 3.6. For example, a 800 μm diameter ball requires about 6.5 m to solidify completely with an initial droplet velocity of 2 m/s and an initial temperature of 508 K. This solidification model, however, does not determine how the droplets solidify. There are at least two ways in which it can solidify. The first is uniform solidification and the other is solidification through the bulk of a droplet as shown in Figure 3.7. The implication of the solidification front needs to be investigated further since it will have an effect on the microstructural evolution of droplets.

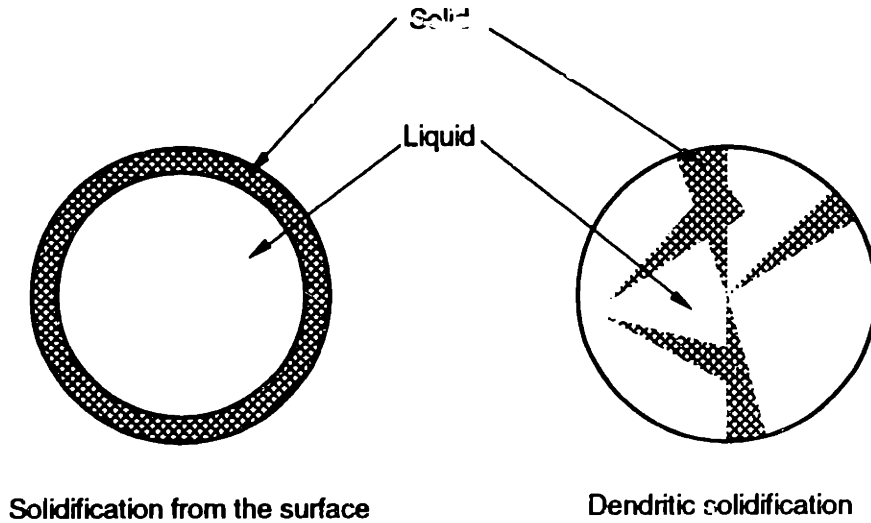


Figure 3.7 Possible solidification fronts for droplets.

3.4.2 Effect of solidification on droplet size

When droplets solidify, they shrink since the density of liquid metal is less than that of solid metal. By the law of mass conservation, it follows that:

$$m_d = \rho_s \left(\frac{\pi d_{d,s}}{6} \right)^3 = \rho_l \left(\frac{\pi d_{d,l}}{6} \right)^3. \quad (3.4.10)$$

The resulting particle size becomes:

$$d_{d,s} = \left(\frac{\rho_l}{\rho_s} \right)^{1/3} d_{d,l} = K_c d_{d,l}, \quad (3.4.11)$$

where K_c is the correction factor. In the case of tin, densities of solid and liquid are 7300 and 7000 kg/m^3 , respectively. Thus the correction factor K_c is 0.986, meaning that the

droplet size will contract by 1.4% as they solidify. For example, a 200 μm liquid tin droplet becomes 197 μm when solid.

3.5 Conclusions

This chapter reviewed the parameters which affect the UDS process. How the ejection pressure can be used to predict the velocity of a liquid jet, which determines the initial droplet velocity, was discussed. The trajectory model was then reviewed. It was established that electrostatic repulsive force, drag force, and gravitational force affect the trajectory of droplets. The drag coefficient was modified to include the effect due to the alignment of droplets. The trajectory of droplets allows accurate estimation of the mass flux of droplets at a given distance from the nozzle. The rate of heat transfer was then reviewed. The heat transfer model assumes Newtonian cooling, for the Biot number of less than 0.01, which assumes that there is no temperature gradient within a droplet.

Nomenclature

A_c	cross-sectional area of an orifice
A_d	surface area of a droplet
a	an empirical coefficient (43.0 ± 15.4)
\mathbf{a}	acceleration
Bi	Biot number, $\frac{hd_d}{k_d}$
C	capacitance
C_d	drag coefficient
$C_{d,adj}$	adjusted drag coefficient
$C_{d,align}$	drag coefficient for an aligned stream of uniformly sized droplets
$C_{d,o+}$	drag coefficient as $L_{space}/d_d \rightarrow 1$
$C_{d,o}$	drag coefficient at $L_{space}/d_d = 1$
$C_{d,rod}$	drag coefficient of a rod
$C_{d,-}$	drag coefficient of an isolated droplet
C_g	specific heat of surrounding medium
$C_{g,ave}$	specific heat of surrounding medium at $T_{g,ave}$
C_{noz}	discharge coefficient of the flow through the nozzle

C_p	specific heat, J / (kg · K)
$C_{p,l}$	specific heat of liquid metal
$C_{p,s}$	specific heat of solid metal
d_d	droplet diameter
$d_{d,l}$	droplet diameter in liquid state
$d_{d,s}$	droplet diameter in solid state
d_j	initial jet diameter
d_o	orifice diameter
E	electric field
F_d	drag force
F_e	electro-repulsion force
f	frequency of imposed vibration
g	gravitational acceleration
H_d	enthalpy
ΔH_f	latent heat
h	convective heat transfer coefficient
K_c	correction factor for droplet diameter changes due to solidification shrinkage
k_d	thermal conductivity of a droplet
k_g	thermal conductivity of surrounding gas
L	distance between two neighboring droplets
\dot{m}	mass flow rate
m_d	mass of a droplet
n	empirical coefficient (0.678±0.07)
\hat{n}	directional unit vector
ΔP	pressure difference, $P_c - P_o$
P_c	pressure of crucible
P_o	pressure of chamber (i.e., ambient pressure)
P_{O_2}	partial pressure of oxygen
Pr	Prandtl number, $\frac{\mu_g C_{p,g}}{k_g}$
Q	total heat transfer
q	charge per droplet
Re	Reynolds number, $\frac{\rho_g \bar{v} d_d}{\mu_g}$
\bar{r}_i	unit vector for a distance
r_i	distance between two point charges

T_d	droplet temperature
T_g	temperature of gas
$T_{g,ave}$	average temperature of surrounding medium, $\frac{T_d + T_o}{2}$
T_m	melting temperature of a droplet
T_o	surrounding gas temperature, i.e., ambient temperature
t	time
Δt	time step
V	voltage
V_{cyl}	volume of a columnar jet
V_{sph}	volume of a spherical droplet
v	relative velocity of a droplet with respect to the air
v_j	jet velocity
$v_{j,min}$	minimum jet velocity required to maintain the continuous laminar jet condition
$v_{j,theo}$	theoretical jet velocity
x	liquid fraction
ϵ_o	permittivity of free space, $8.8542 \times 10^{-12} \text{ C}^2/(\text{N} \cdot \text{m}^2)$
ϵ	emissivity of radiation
λ_d	wavelength, v_j/f
μ	viscosity
μ_l	viscosity of liquid
μ_g	viscosity of surrounding medium
ρ_l	density of liquid jet, or at liquid state
ρ_g	density of surrounding medium
ρ_s	density at solid
σ	surface tension (Interfacial tension)
σ_{SB}	Stefan-Boltzmann constant, $5.6697 \times 10^{-8} \text{ W}/(\text{m}^2 \cdot \text{K}^4)$

Chapter 4 EXPERIMENTAL STUDIES OF JET BREAK-UP BEHAVIOR

4.1 Introduction

Chapter 2 discussed the linear theory of liquid jet break-up. This chapter discusses experimental procedures to investigate the jet break-up behavior of molten metal jets. The features of the UDS apparatus are discussed in detail and the experimental results are presented. The material used in this study was pure tin (99.99%). The pure tin was melted in a stainless crucible and sprayed into an inert gas environment, which has been vacuumed and refilled with a nitrogen gas with an oxygen content of less than 5 ppm.

4.2 Experimental Apparatus and Procedure

4.2.1 Experimental apparatus

The apparatus is essentially the same as presented in Chapter 1. See Figure 1.3 for a schematic representation. It consists of the droplet generator, a spray chamber, a gas control system, and a video monitoring unit. The droplet generator unit, shown in Figure 1.2, consists of a crucible, a temperature controller, a melt vibration unit, and a charging unit. The crucible is made of 303 stainless steel. A resistance heater melts the metal. The thermocouple is a K-type, connected to the temperature controller (OMEGA, Model No. CN9500) to maintain the metal at a desired temperature. The melt vibration system consists of a stack of piezoelectric crystals (PZT-5A/Navy Type), a function generator with a digital readout (BK PRECISION, 2 MHz, Model No. 3011B), an audio amplifier (Radio Shack, 20 Watts, Model No. MAP-30), an audio transformer to increase the voltage applied to the piezoelectric crystals, and an oscilloscope (BK PRECISION, 2 MHz, Model No. 2120).

The charging plate made of 12.7 mm thick brass was placed under the crucible. An insulator (glass or alumina oxide—typically 2.5 mm thick) was placed between the crucible and the charging plate. The charging plate had a 9.5 mm slot where the molten metal jet breaks into a train of uniform droplets. The charging plate is connected to the high DC voltage source (Bertan Associates, Inc., Series 230) to charge the droplets electrostatically.

The continuous laminar jet was formed through the small nozzle at a certain velocity by applying high pressure (typically 7 to 350 kPa of ejection pressure) nitrogen gas to the

crucible. The velocity depends on the nozzle geometry and the pressure applied to the crucible. As the jet came out of the nozzle, the perturbation frequency was applied to the nozzle area through a long shaft, which transmitted the vibration from the piezoelectric crystals.

The piezoelectric crystals are placed away from the heating zone so that the temperature increase in the system does not affect the performance of the crystals. The amplitude of the perturbation can be increased to some degree if the crystals are stacked in series mechanically and in parallel electrically. It was, however, observed that stacking more than four piezoelectric crystals did not further increase the amplitude since the voltage that can be applied reduces as more crystals are stacked up. The performance of crystal can be explained by:

$$a = \omega^2 s, \quad (4.2.1)$$

where a is the acceleration, ω the frequency of oscillation, and s the displacement of the crystals. As can be seen in the above equation, the displacement would be smaller if the frequency of oscillation were to increase. If the voltage to the crystals is increased to achieve a larger displacement, the frequency has to be reduced. Otherwise, the crystals would not be able to respond to the applied frequency; they would simply vibrate out of control, and eventually lose their piezoelectric behavior. Thus, it is not feasible to increase the displacement by increasing the number of crystals in the stack or by increasing the voltage. The manufacturer does not recommend the application of more than 1000 V to the crystals.

The droplet generator system was placed in a Dow Corning Pyrex spray chamber which is 0.9 m long and 0.15 m in diameter. The droplets were solidified and collected in the spray chamber. The video monitoring system included a monitor (Sony, Model No. PVM-1390), a CCD video camera (Techni-Quip), a strobe light (Quadtech, Model No. 1538-A). The monitoring system was used to observe and measure the break-up process and the break-up length. The break-up process was recorded by a VCR (Mitsubishi, Model No. HS-U34) The gas control system included the supply of nitrogen gases to the spray chamber and the crucible. The gas flows were regulated by two-way and three-way valves, connected by 9.5 mm (3/8") OD Teflon tubes.

4.2.2 Experimental procedure

The 100 μm diameter orifice made of ruby (Bird Precision, Part No. 22499) was mounted to the bottom of the crucible plate using a ceramic adhesive as shown in Figure 4.1. About 0.5 Kg of 99.99% pure tin was placed inside of the crucible. The bottom plate with the orifice was then attached to the crucible by eight 8-32 NC screws. A 1.6 mm graphite nickel-reinforced gasket (Flexitallic Gasket, Deer Park, TX) was placed between the crucible and the crucible plate to prevent the leak of molten metal.

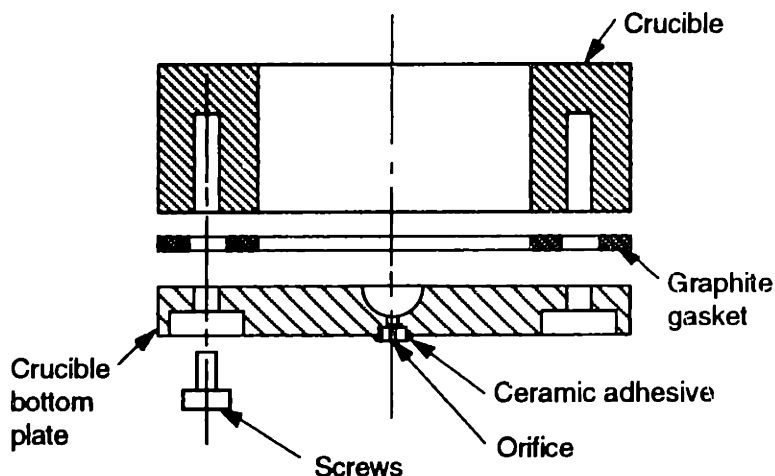


Figure 4.1 Schematic of crucible bottom plate.

The spray chamber was evacuated to about 50 mTorr using a mechanical vacuum pump (Welsh Scientific, Model No. 1376). The chamber then was filled to the gauge pressure of 35 kPa (5 psig) with an industrial grade pure nitrogen, which contains less than 5 ppm of oxygen. The above procedure was repeated three times to purify the spraying chamber further. Then pure tin was melted to 508 K. Next, the crucible was then pressurized to the gauge pressure of 125 to 195 kPa (18 to 28 psig) to produce a continuous laminar jet with a velocity of 4 to 5 m/s.

As the continuous laminar jet of molten tin discharged from the nozzle, the appropriate frequency was applied to break the jet into a train of uniform droplets. The discharged tin was collected then in a container to measure the mass flow rate, which then can be used to obtain the jet velocity as discussed in Chapter 2. The amplitude of perturbation to the nozzle area was changed by varying the voltage to the piezoelectric crystal. The function generator generated vibration frequency; the signal was fed then into the amplifier and an audio transformer to step up the voltage to the piezoelectric crystal. Typically, a voltage of 400 was supplied to the crystal. The voltage was monitored by the

oscilloscope. The voltage was attenuated by 100 times before it was connected to the oscilloscope since the voltage ranges for the oscilloscope were ± 20 mV and ± 20 V. As the jet broke into a train of uniform powders, the jet break-up length and wavelength were measured from the monitor.

4.3 Results and Discussion

4.3.1 Measurement of jet velocity

It is imperative in the UDS process to make sure that jet velocities from the nozzle are consistent since jet velocity is one of the parameters which determine the solidification of droplets and their impact on the substrate. Three different gauge pressures were applied to the crucible to measure the jet velocities: 125, 160 and 195 kPa. The spray chamber was filled to the gauge pressure of 35 kPa (5 psig), resulting in ejection pressures of 90, 125, and 160 kPa (13, 18 and 23 psia), respectively. The pressure ranges are not high since the safety of the design and the formation of continuous laminar jets of molten metal limit the pressure that can be applied to the crucible. Nevertheless, selected pressure ranges are of practical use for typical UDS operating conditions.

If too much pressure is applied to the crucible, the jet may become turbulent and allow secondary atomization, generating non-uniform droplets. If too little pressure is applied, the jet may not form; instead, the flow will become “drop-wise,” as discussed in Chapter 3. The minimum jet velocity, $v_{j,\min}$, to form a continuous laminar jet is given by:

$$v_{j,\min} = \sqrt{\frac{8\sigma}{\rho_l d_j}}, \quad (4.3.1)$$

where ρ_l is the liquid density, σ the surface tension, and d_j the jet diameter. For pure tin at the operating temperature of 553 K as shown in Table 4.1, the minimum jet velocity to maintain a continuous laminar jet should be about 2.5 m/s for the jet with a diameter of 100 μm , assuming the jet diameter is equal to the orifice diameter. The minimum pressure to be applied to the crucible can be calculated since the velocity is related to the pressure by the following equation:

$$v_j = C_{noz} \sqrt{\frac{2 \cdot \Delta P}{\rho_l}}, \quad (4.3.2)$$

where C_{noz} is the discharge coefficient of the flow through the nozzle and ΔP the ejection pressure. If the discharge coefficient is assumed to be one, the minimum pressure needed to be applied to the crucible to form a continuous laminar jet should be about 22 kPa above the spray chamber.

Table 4.1 Properties of pure tin

	Density (Kg/m ³)	Surface tension (N/m)	Viscosity ($\frac{kg}{m \cdot s}$)
At melting temperature of 505 K (232 C)	7000	0.544	1.85×10^{-3}
At operating temperature of 553 K (280 C)	6971	0.5406	1.664×10^{-3}

Table 4.2 shows the theoretical velocities and Reynolds numbers of flow conditions for selected pressure ranges. The Reynolds number is defined as:

$$Re = \frac{\rho_l v_j d_j}{\mu_l}, \quad (4.3.3)$$

where μ_l is the viscosity of liquid. The theoretical velocities for selected pressure ranges are well above the minimum required jet velocity. The Reynolds numbers are between 2000 to 3000. The critical Reynolds number is known to be 2300 for a pipe flow, and is defined as the transition point from laminar to turbulent flow. However, it has been observed that the laminar flow can be maintained for the Reynolds number of up to 40,000 depending on flow conditions and pipe smoothness (Shames, 1982). From the preliminary experimental observations, the flows at the ejection pressures of 125 and 160 kPa were shown to be laminar since no secondary atomization was observed as with the case of turbulent flows.

Table 4.3 and Figure 4.2 show the measured jet velocities for selected pressure ranges. They were measured by three different methods as described in Chapter 3. The jet velocities were calculated by measuring the discharged mass of tin, by measuring the wavelength of droplets from the monitor, and by measuring the size of droplets produced. The relationships used are as follows:

$$v_j = \frac{4\dot{m}}{\pi d_j^2 \rho_l} \text{ for the mass flow rate method} \quad (4.3.4)$$

$$v_j = \lambda_d \cdot f \text{ for the video measurement method,} \quad (4.3.5)$$

and

$$v_j = f \cdot d_j \frac{2}{3} \left(\frac{d_d}{d_j} \right)^3 \text{ for the droplet measurement method,} \quad (4.3.6)$$

where \dot{m} is the mass flow rate, λ_d the wavelength, f the applied frequency, and d_d the droplet diameter.

Table 4.2 Theoretical velocities and Reynolds number of flow conditions for selected pressure ranges

Ejection pressure (kPa)	Theoretical jet velocity (m/s)	Reynolds number
90	5.1	2130
125	6.0	2510
160	6.8	2840

Table 4.3 Measured velocities by three different methods

Ejection pressure (kPa)	Theoretical velocity (m/s)	Mass flow rate (m/s)	Video measurement (m/s)	Droplet Measurement (m/s)	Discharged coefficient *
90	5.08	3.87	3.95	N/A	0.76
125	5.99	4.64	5.02	4.48	0.77
160	6.78	4.96	5.76	N/A	0.73

* the jet velocities measured by mass flow rate were used to calculate the discharged coefficient.

The average jet velocities calculated by mass flow rate and video measurement for the ejection pressure of 125 kPa were 4.64 and 5.02 m/s with the standard deviations of 0.07 and 0.14 m/s, respectively. These standard deviations represent about 1.5% or 2.8%, respectively, from the average jet velocities. These numbers (discussed in more detail in the following section) represent eleven experimental runs. The jet velocity obtained by the droplet measurement for 125 kPa was 4.48 m/s, which is less than the measurements by the mass flow rate and the video measurement.

The jet velocities for the ejection pressures of 90 and 160 kPa were 3.87 and 4.96 m/s by the mass flow rate and 3.95 and 5.76 m/s by the video measurement. Although few runs were performed for these pressure settings, the calculated jet velocities

seem to be consistent with those of 125 kPa. The discharged coefficients are very close to each other, as can be seen in Table 4.3.

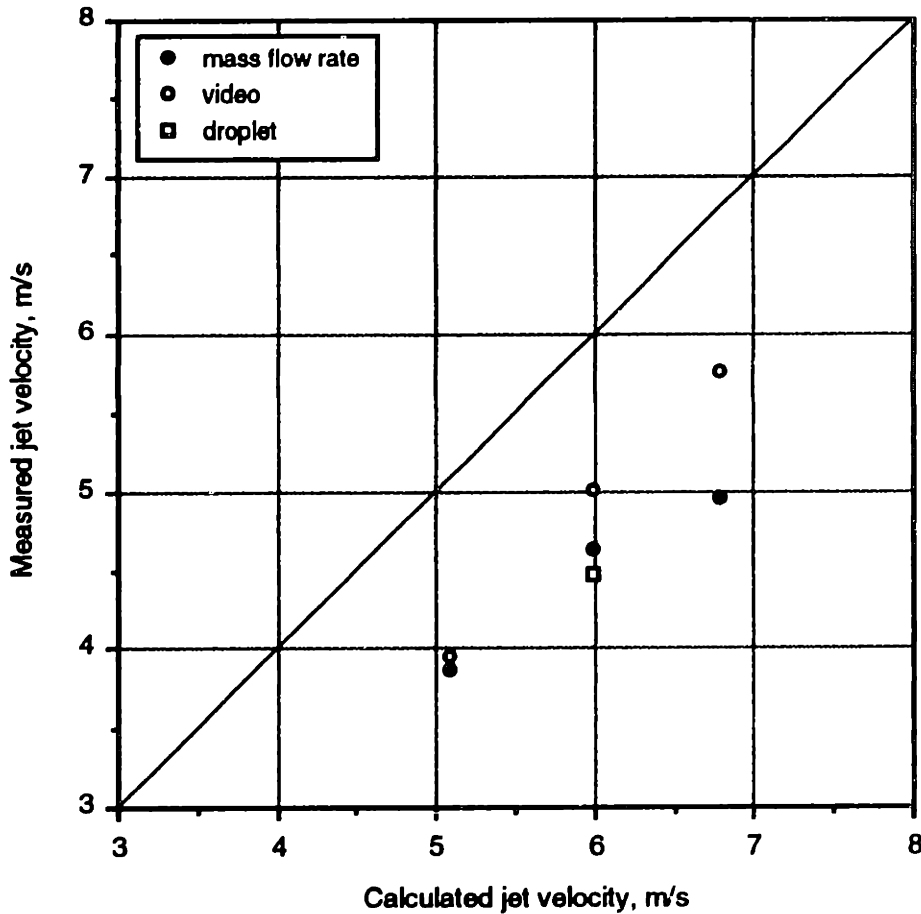


Figure 4.2 Calculated jet velocity vs. measured jet velocity of liquid tin. Jet diameter is 100 μm . Ejection pressures are 90, 125 and 160 kPa, respectively. The density of liquid tin is assumed to be 6971 kg/m^3 . Jet velocities are calculated assuming the jet diameter is equal to the orifice diameter.

4.3.2 Variations of jet velocities with respect to different runs

Figure 4.3 shows the trends of jet velocity obtained by the mass flow rate measurement and by the video measurement. The ejection pressure of 125 kPa was applied to the crucible to form a continuous laminar jet of pure molten tin. The discharged mass was collected in a container for a given period of time to obtain the mass flow rate, which was converted to the jet velocity using equation (4.3.4). The density of pure tin was assumed to be 6971 kg/m^3 as shown in Table 4.1. The average jet velocity for these

eleven runs was 4.64 m/s with a standard deviation of 0.08 m/s. The high and low jet velocities were 4.76 and 4.56 m/s, respectively.

To estimate the jet velocity using the video monitor, the spacing between the droplets was measured. The video was scaled up to 18x in these measurements. The wavelength of 15 droplets was measured and divided by 15 to reduce the measurement error for the wavelength between the two neighboring droplets. The jet velocity was calculated using equation (4.3.5). The average jet velocity for these runs was 5.02 m/s with a standard deviation of 0.14 m/s. The high and low jet velocities by the video measurements were 5.22 and 4.83 m/s, respectively.

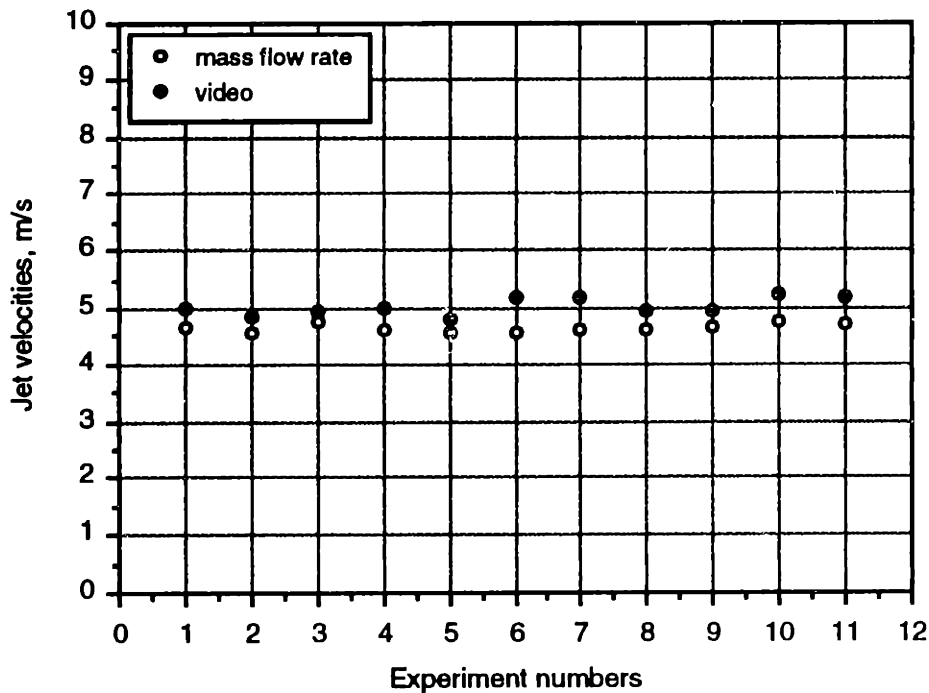


Figure 4.3 Measured jet velocity variation due to run to run. The jet velocities are obtained from the mass flow rate measurements. Orifice diameter is 100 μm , ejection pressure 125 kPa. The density of liquid tin is assumed to be 6971 kg/m^3 and jet velocities are calculated assuming the jet diameter is equal to the orifice diameter. The average jet velocity is 4.64 m/s with a standard deviation of 0.08 m/s.

Sensitivity of jet velocity by the mass flow rate

The sensitivity of jet velocity by the mass flow rate due to the variables can be written as:

$$\Delta v_j = \sqrt{\left(\frac{\partial v_j}{\partial \dot{m}} \Delta \dot{m}\right)^2 + \left(\frac{\partial v_j}{\partial \rho_l} \Delta \rho_l\right)^2 + \left(\frac{\partial v_j}{\partial d_j} \Delta d_j\right)^2}. \quad (4.3.7)$$

As shown in equation (4.3.7) the sensitivity is dictated by a possible measurement error of mass flow rate, the manufacturer's specification for the orifice diameter, and the density variation due to the cooling of the strand, i.e., the laminar jet. The mass flow rate is about 0.25 g/s, and does not influence the variation on the jet velocity. The variation due the density changes can be assumed to be about 30 kg/m³, which is the difference between the operating temperature and the melting temperature of tin as shown in Table 4.1. The jet velocity variation due to the density difference is about 0.02 m/s. The tolerance of orifice diameter according to the manufacturer's specification is 5 μm, which yields the variation of 0.45 m/s. The variation of 5% from the nominal orifice diameter contributes to a variation of about 10% in the jet velocity of liquid. The measurement error for the mass flow rate can to be calculated from the mass flow rate itself. The mass flow is calculated by:

$$\dot{m} = M / t, \quad (4.3.8)$$

where M is the total mass collected in a given time t . Thus, the uncertainty associated with the mass flow rate can be obtained by:

$$\Delta \dot{m} = \sqrt{\left(\frac{\partial \dot{m}}{\partial M} \Delta M\right)^2 + \left(\frac{\partial \dot{m}}{\partial t} \Delta t\right)^2}. \quad (4.3.9)$$

Typically, the total mass collected was about 0.1 kg in 300 s; these numbers will be used as a base case. The uncertainties associated with the mass and time measurements were approximately 0.1 × 10³ kg and 0.5 s, respectively. The uncertainty associated with the mass flow rate calculated using equation (4.3.9) is found to be 6.5 × 10⁻⁷ kg/s. Thus, the variation of jet velocity due to the mass flow rate uncertainty is 0.012 m/s. Table 4.4 summarizes the contribution of three different parameters to the sensitivity of jet velocity obtained using the mass flow rate. It shows that jet velocity measurement by the mass flow rate is most sensitive to the uncertainties of orifice diameter.

The standard deviation of the measurements is lower than the sensitivity of jet velocity due to the variation of parameters that determine the jet velocity. Usually, the variation of orifice diameter is less than the manufacturer's specification on the part drawing. When the diameter of orifices from a batch was measured, it was about $\pm 1 \mu\text{m}$ of the nominal orifice diameter. Thus, the sensitivity of jet velocity measurement becomes about 0.09 m/s, which is consistent with the standard deviation of the jet velocity measurements.

Table 4.4 Jet velocity measurement uncertainties by mass flow rate due to different variables

	Uncertainties	Variation on jet velocity (m/s)
Mass flow rate	$\frac{\partial v_j}{\partial \dot{m}} \Delta \dot{m} = \frac{4}{\pi d_j^2} \frac{1}{\rho_l} \Delta \dot{m}$	0.012
Density	$\frac{\partial v_j}{\partial \rho_l} \Delta \rho_l = \frac{4}{\pi d_j^2} \frac{\dot{m}}{\rho_l^2} \Delta \rho_l$	0.02
Jet diameter	$\frac{\partial v_j}{\partial d_j} \Delta d_j = \frac{8}{\pi d_j^3} \frac{\dot{m}}{\rho_l} \Delta d_j$	0.45
Total	Δv_j	0.45

Sensitivity of jet velocity by video measurement

The sensitivity of jet velocity by the video measurement depends on the wavelength and frequency measurements. It can be written as:

$$\Delta v_j = \sqrt{\left(\frac{\partial v_j}{\partial \lambda_d} \Delta \lambda_d\right)^2 + \left(\frac{\partial v_j}{\partial f} \Delta f\right)^2} \quad (4.3.10)$$

The typical wavelength for a 100 μm orifice diameter is approximately $0.45 \times 10^{-3} \text{ m}$ and the frequency is about 11 kHz. The uncertainties for the wavelength measurement and frequency are $0.03 \times 10^{-3} \text{ m}$ and 1% of the frequency reading, i.e., 0.11 kHz. Table 4.5 summarizes the variation on jet velocity due to the uncertainties of these parameters. It shows that the sensitivity of jet velocity measurement by the video measurement is dominated by the measurement uncertainty in the wavelength measurement of droplet spacing.

Table 4.5 Jet velocity measurement uncertainties by video measurement due to different variables

Uncertainties		Variation on jet velocity (m/s)
Wavelength	$\frac{\partial v_j}{\partial \lambda_d} \Delta \lambda_d = f \Delta \lambda_d$	0.33
Frequency	$\frac{\partial v_j}{\partial f} \Delta f = \lambda_d \Delta f$	0.05
Total	Δv_j	0.33

Sensitivity of jet velocity by droplet measurement

The sensitivity of jet velocity by droplet measurement depends on uncertainties of frequency, orifice diameter, and droplet diameter measurement.

$$\Delta v_j = \sqrt{\left(\frac{\partial v_j}{\partial f} \Delta f\right)^2 + \left(\frac{\partial v_j}{\partial d_j} \Delta d_j\right)^2 + \left(\frac{\partial v_j}{\partial d_d} \Delta d_d\right)^2} \quad (4.3.11)$$

The uncertainties for frequency and orifice diameter were given earlier. The diameter of powders produced was approximately 180 μm. The measurement was done with a microscope with the uncertainty of 1.3 μm (0.00005”). Table 4.6 summarizes the findings. Again, the dominant parameter that affects the sensitivity of jet velocity measurement by the droplet measurement is the uncertainty in the orifice diameter. As discussed earlier, the tolerance specification of the orifice can be substituted by the measurement uncertainty by the microscope measurement of the orifice diameter, in which case the variation on jet velocity due to the uncertainty in the orifice diameter can be reduced to about 0.09 m/s. This is similar to the variation due to the uncertainty of droplet diameter measurement.

Using the above sensitivity calculation, Figure 4.2 can be reconstructed to include the error bars for the different measurements for the jet velocity. As shown in Figure 4.4, the jet velocity by the video measurement was shifted to the left and the jet velocity by the droplet measurement was shifted to the right to avoid overlap of the error bars. The jet velocities calculated by the mass flow rate and the video measurement for the ejection pressure of 90 kPa seem to match fairly well. For the ejection pressure of 125 kPa, there are some discrepancies of jet velocities by the three different methods. However, the values are still within the boundaries of the error bars. For the ejection pressure of 165 kPa, however, the discrepancy of jet velocities by the mass flow rate and the video

measurement become larger, and the boundary or error bars barely touch each other. The curve of the video screen may have contributed to the reading error, which may have overestimated the wavelength of the droplet spacing, causing the increase in jet velocity calculation.

Table 4.6 Jet velocity measurement uncertainties by droplet measurement due to different variables

		Variation on jet velocity (m/s)
Frequency	$\frac{\partial v_j}{\partial f} \Delta f = \frac{2 d_d^3}{3 d_j^2} \Delta f$	0.04
Jet diameter	$\frac{\partial v_j}{\partial d_j} \Delta d_j = f \frac{4 d_d^3}{3 d_j^3} \Delta d_j$	0.43
Droplet diameter	$\frac{\partial v_j}{\partial d_d} \Delta d_d = 2 f \frac{d_d^2}{d_j^2} \Delta d_d$	0.09
Total	Δv_j	0.44

Sensitivity of jet velocity to pressure

The theoretical jet velocities were calculated from the ejection pressures. However, there are uncertainties associated with the pressure setting, which cannot be ignored when interpreting the results. The sensitivity of jet velocity due to the pressure depends on uncertainties of pressure settings and density of fluid as follows:

$$\Delta v_j = \sqrt{\left(\frac{\partial v_j}{\partial (\Delta P)} \Delta (\Delta P) \right)^2 + \left(\frac{\partial v_j}{\partial \rho_l} \Delta \rho_l \right)^2} \quad (4.3.12)$$

Uncertainties associated with the ejection pressure and density were estimated to be 10 kPa (1.5 psia), and 30 kg/m³, respectively. Table 4.7 summarizes the uncertainties associated with the above parameters, assuming a discharge coefficient of 0.75. As the ejection pressure increases, the uncertainty due to the pressure setting decreases. The effect of density uncertainty on the sensitivity of jet velocity is quite negligible.

Table 4.7 Uncertainties of jet velocity due to pressure settings

Uncertainties	Variation on jet velocity (m/s) $\Delta P=90$ kPa	Variation on jet velocity (m/s) $\Delta P=125$ kPa	Variation on jet velocity (m/s) $\Delta P=160$ kPa
Ejection pressure $\frac{\partial v_j}{\partial(\Delta P)} \Delta(\Delta P) = C_{noz} \sqrt{\frac{1}{2\Delta P \rho_l}} \Delta(\Delta P)$	0.22	0.18	0.16
Density $\frac{\partial v_j}{\partial \rho_l} \Delta \rho_l = C_{noz} \sqrt{\frac{\Delta P}{2\rho_l^3}} \Delta \rho_l$	0.01	0.01	0.01
Total Δv_j	0.22	0.18	0.16

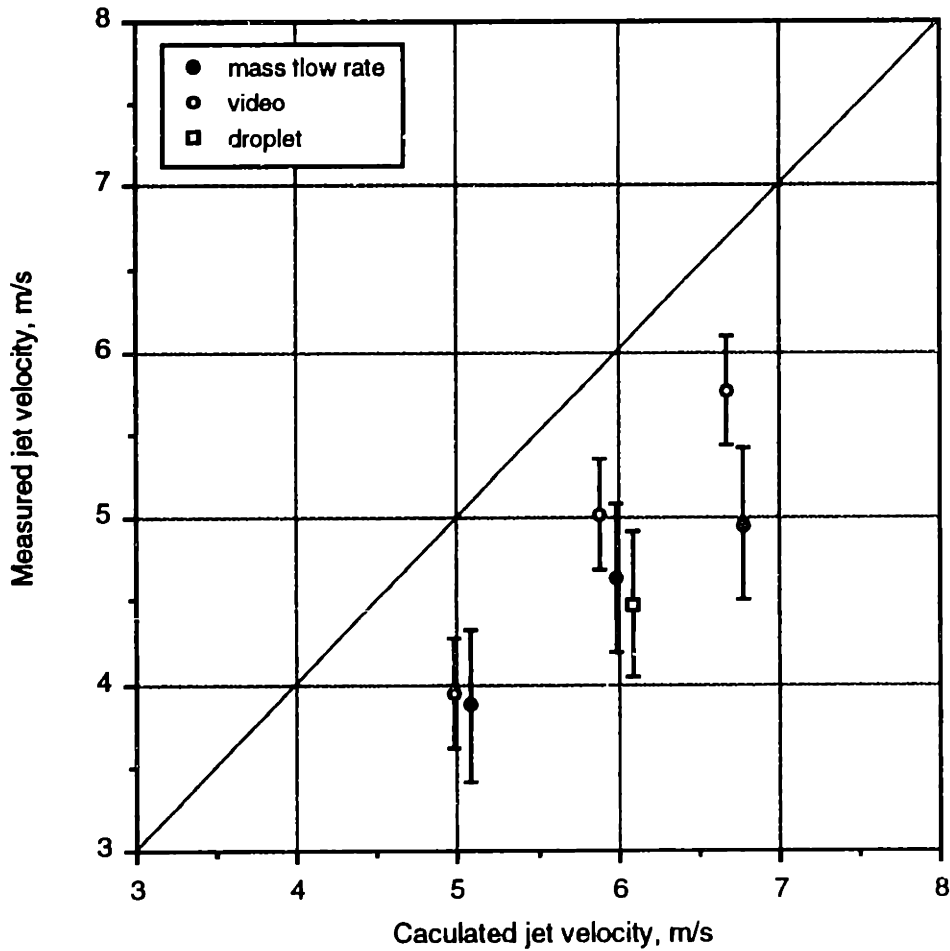


Figure 4.4 Calculated jet velocity vs. measured jet velocity of liquid tin with error bars.

4.3.3 Jet break-up length with respect to time

One of the ways to characterize the break-up behavior of laminar jets is to observe the break-up length. As discussed in Chapter 2, material properties, orifice size, and the frequency and amplitude of perturbation determine the jet break-up length. Thus, reliable prediction of jet break-up processes depends on consistent break-up length for run-to-run and within-the-run for the same experimental conditions. Figure 4.5 shows the variation of jet length with respect to the time for five different runs with the same experimental conditions.

Approximately 0.3 kg of pure tin was melted in the crucible. Pressure was applied to the crucible to form a laminar jet. The ejection pressure was 125 kPa. The jet was subjected to vibration at a frequency of 11.34 kHz. The amplitude of perturbation on the jet was not directly measured. However, the amplitude correlated with the voltage was applied to the piezoelectric crystals, which was 400 V. The orifice diameter was 100 μm .

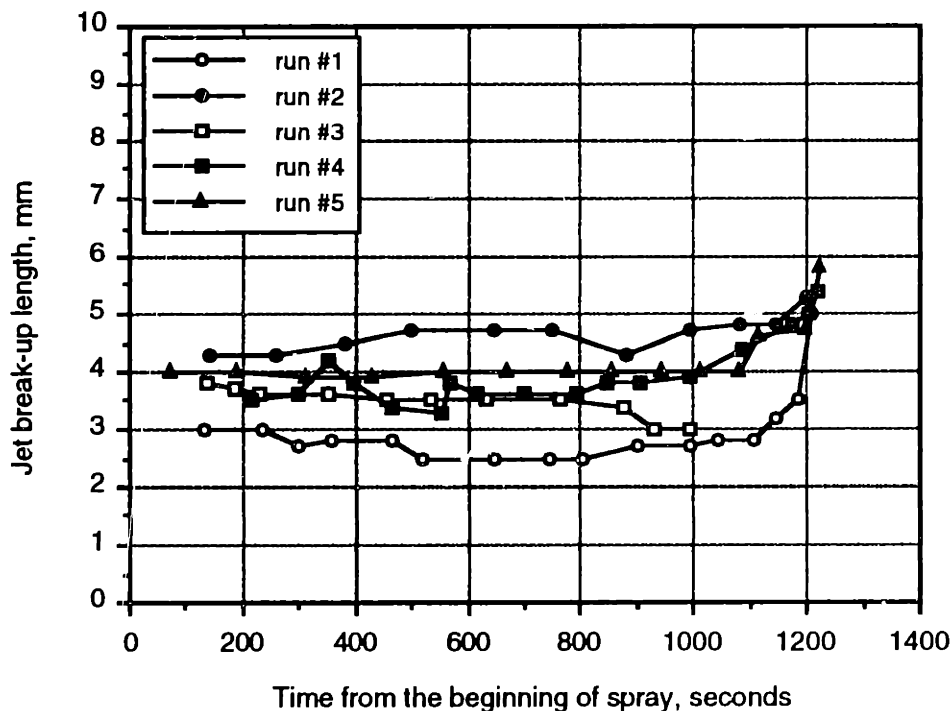


Figure 4.5 Jet break-up length variation with respect to spraying time for five runs. Jet diameter is 100 μm and ejection pressure 125 kPa, and vibration frequency 11.34 kHz. 400 V was applied to the piezoelectric crystals.

The break-up lengths for different runs seem to vary from 2.5 to 4.5 mm with the average of approximately 3.5 mm even though the experimental conditions were the same. The break-up length for a single run seems to be consistent throughout the run except for increasing near the end. The increase in the break-up length may be caused by the sudden drop in the vibration transfer. As shown in Figure 4.6, the vibration is transmitted from the piezoelectric crystals to the orifice area through a long vibration shaft, which is immersed in the melt. When the top surface of the melt drops below the end of the shaft, the vibration is no longer transmitted to the orifice area through the melt. The vibration has to be transmitted via the gas in the crucible, which may dampen the amplitude of vibration, causing the break-up length to increase. The discrepancies of break-up length from run to run may have been due to the actual torque applied to the bolts (connecting the top plate and the crucible top plate) and screws (connecting the crucible and the crucible bottom plate).

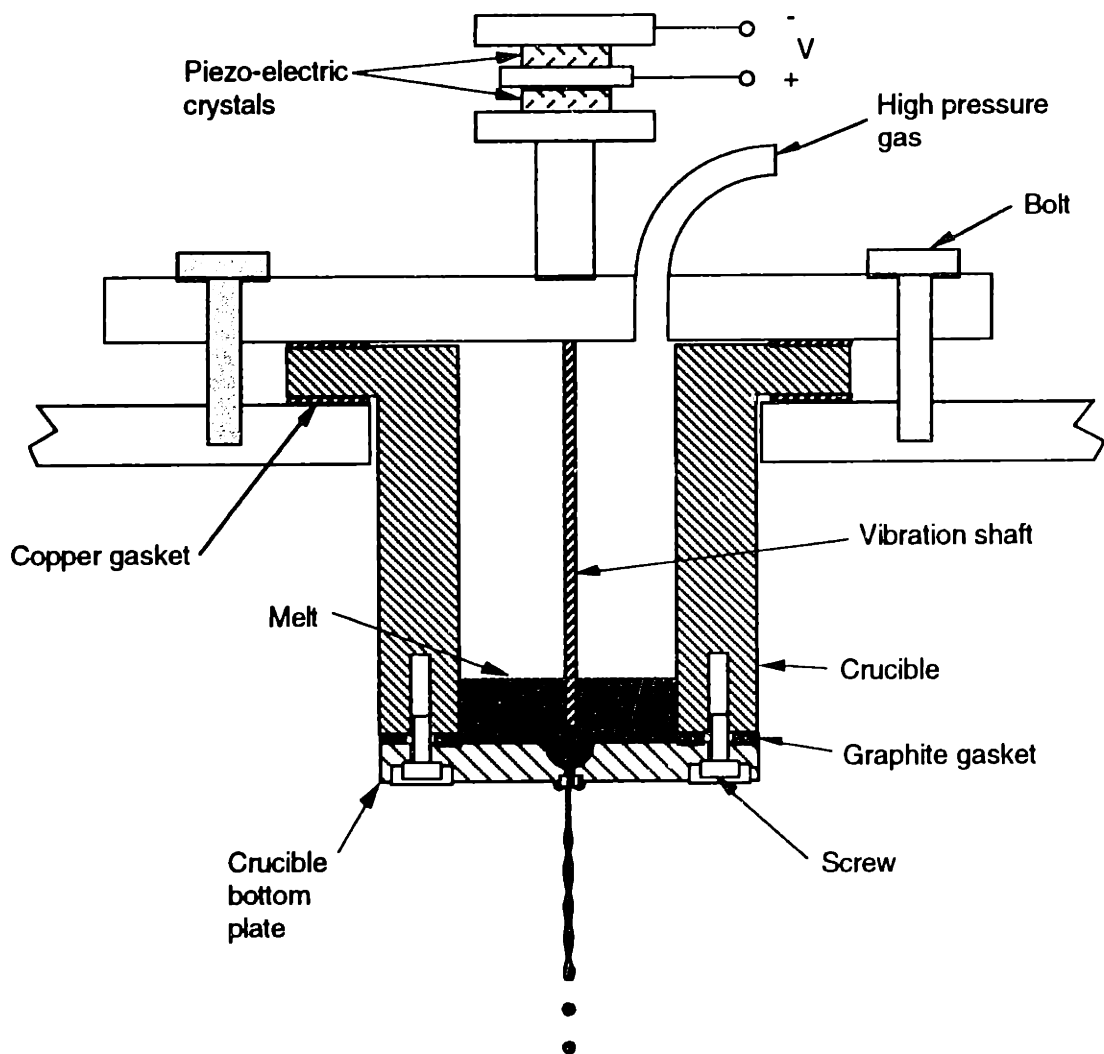


Figure 4.6 Break-up of laminar jet.

4.3.4 Jet break-up length with respect to dimensionless wavelength

As discussed in Chapter 2, the jet break-up length can be calculated using:

$$L_j = \frac{v_j}{q} \ln\left(\frac{d_j}{2\delta}\right), \quad (4.3.13)$$

where the growth rate, q , is defined as:

$$q = \sqrt{\frac{\sigma}{\rho d_j^3} \left[-6(\text{Oh})\gamma^2 + \sqrt{36(\text{Oh}^2)\gamma^4 + 4(1-\gamma^2)\gamma^2} \right]}. \quad (4.3.14)$$

The Ohnesorge number, Oh , is defined as:

$$\text{Oh} = \frac{\mu}{\sqrt{\rho d \sigma}}, \quad (4.3.15)$$

and the dimensionless wave number, γ , is defined as:

$$\gamma = \frac{\pi d_j}{\lambda}. \quad (4.3.16)$$

Assuming the jet break-up length, L_j , is about 3.5 mm when 400 V is applied to the piezoelectric crystals, and using the material properties at the operating temperature of 553 K as listed in Table 4.1, the logarithmic term, $\ln(d_j/2\delta)$, becomes 6.38. This implies that the initial disturbance to the jet is 8.5×10^{-8} m for a jet with the diameter of 100 μm . The displacement coefficient for the piezoelectric crystals is 374×10^{-12} m/volt. Thus, applying 400 V to the two stacks of crystals should result in the displacement of 7×10^{-7} m for the piezoelectric crystals. Thus, it seems that only one tenth of the perturbation amplitude from the crystals is transmitted to the jet surface.

Figure 4.7 shows the jet break-up length with respect to the dimensionless wavelength, λ/d_j , for the ejection pressure of 125 kPa, which translates to the jet velocity of 4.64 m/s calculated by the mass flow rate as discussed in the previous section. The dimensionless wavelength was calculated by using:

$$\frac{\lambda}{d_j} = \frac{v_j}{fd_j}. \quad (4.3.17)$$

The frequency of vibration to break a jet into a train of uniform droplets ranges from 8.06 to 15.01 kHz, which translates to the dimensionless wavelength of 5.73 to 3.08. The

points indicate the dimensionless wavelengths at which uniform droplets were produced although other dimensionless wavelengths in between low and high could have been used to break the jet into uniform droplets.

According to Rayleigh's analysis, as discussed in Chapter 2, the minimum jet break-up length should occur near the dimensionless wavelength of 4.51, i.e., at the maximum growth rate. Experimental results, however, show the minimum jet break-up length seems to occur at dimensionless wavelength of 4.0. If Figure 4.7 were to be redrawn using the jet velocity calculated by the video measurement, which was 5.02 m/s, the dimensionless wavelength should be closer to 4.51, the expected value.

Rayleigh's analysis also shows that the dimensionless wavelength has to be greater than 3.14 for the jet to become unstable such that it breaks into droplets. However, some of the experimental points in Figure 4.7 are below the critical dimensionless wavelength of 3.14. This discrepancy of dimensionless wavelengths can also be attributed to the underestimation of jet velocity by the assumption that the orifice diameter is equal to the jet diameter. If the jet diameter is less than the orifice diameter, the actual dimensionless wavelength used in the figure has to be higher, making the experimental values more consistent with the theoretical values. Measuring the jet diameter using the video screen is difficult since the measurement is limited by the pixel size and numbers in the screen. More accurate measurement of jet diameter would allow more accurate assessment of jet velocity.

Figure 4.8 shows the jet break-up length versus the dimensionless wavelength for three different pressure settings. The jet velocities used in the figure were calculated by the mass flow rate measurement. The dimensionless wavelength for ejection pressure of 90 kPa, i.e., jet velocity of 3.87 m/s, ranges from 2.89 to 7.37, or the frequency of 13.38 to 5.25 kHz, respectively. The dimensionless wavelength for the ejection pressure of 160 kPa, i.e., jet velocity of 4.96 m/s, ranges from 3.27 to 6.12, or the frequency of 15.19 to 8.10 kHz, respectively. As the jet velocity increases, the jet break-up length increases as seen in equation (4.3.13). However, the break-up lengths with the jet velocity of 3.87 m/s (ejection pressure of 90 kPa) seem generally higher than those with 4.64 m/s (ejection pressure of 125 kPa). This can be attributed to the variations in the jet velocities from run to run, as seen in Figure 4.5.

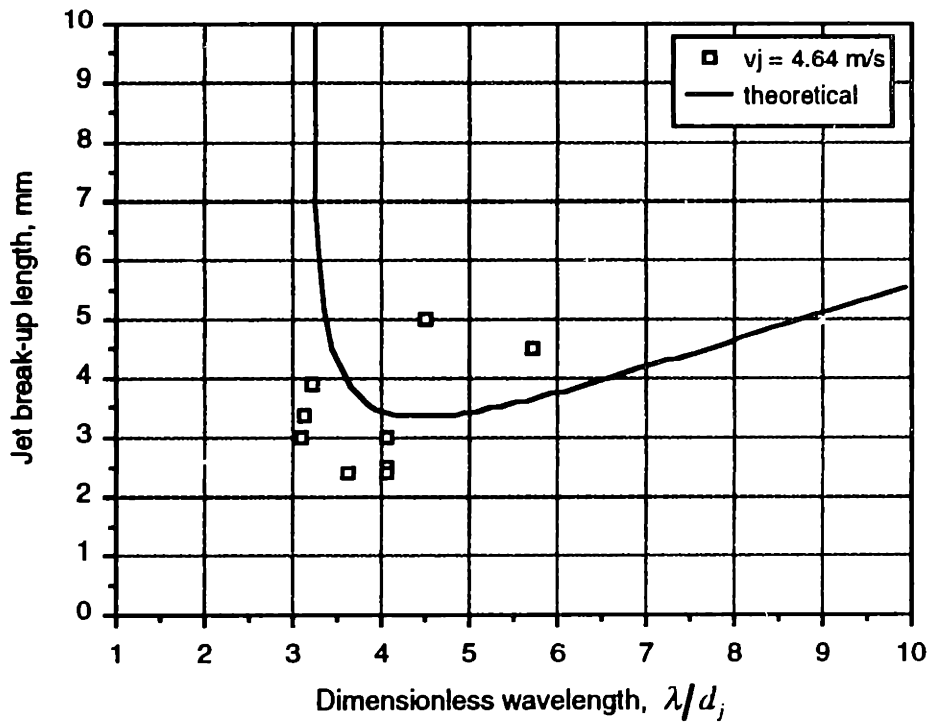


Figure 4.7 Jet break-up length versus dimensionless wavelength at a jet velocity of 4.64 m/s assuming a jet diameter of 100 μm . 400 V was applied to the piezoelectric crystals.

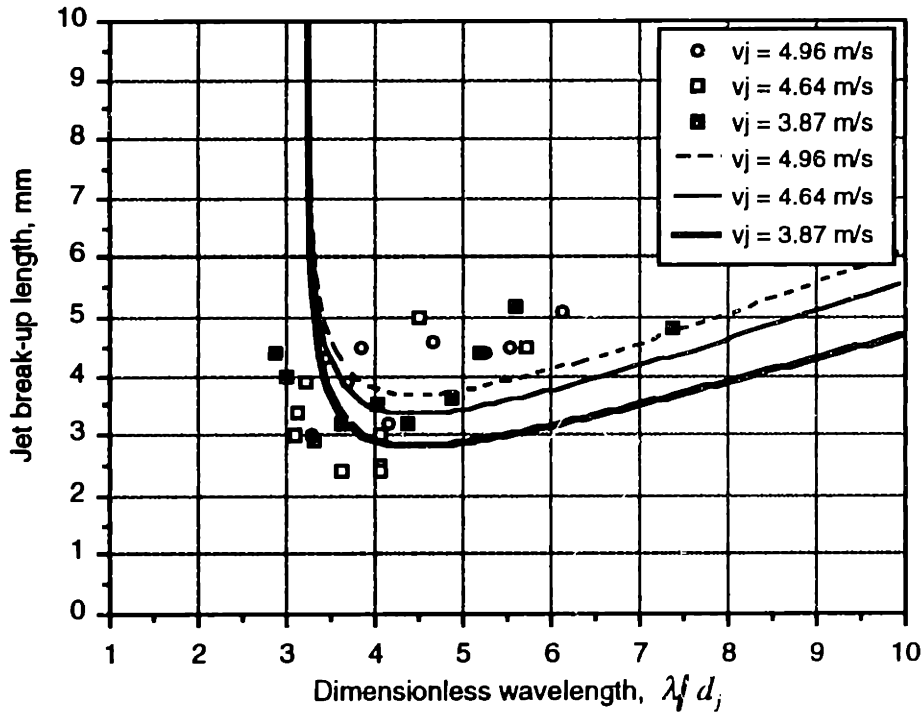


Figure 4.8 Jet break-up length versus dimensionless wavelength at various velocities assuming a jet diameter of 100 μm . 400 V was applied to the piezoelectric crystals.

4.3.5 Jet break-up length with respect to perturbation amplitude

As mentioned earlier, the jet break-up length can be varied by changing the amplitude of perturbation. Equation (4.3.13) shows the relationship between the jet break-up length and the amplitude of perturbation applied to the orifice area. Figure 4.9 shows the jet break-up length versus the voltage applied to the piezoelectric crystals. As discussed earlier, the voltage was used as a amplitude of perturbation since no direct measurement of the perturbation amplitude was made. As expected from Rayleigh's analysis, the jet break-up length is inverse-logarithmically related to the perturbation amplitude as shown in the Figure 4.9. The figure only contains one set of experiments although many preliminary runs were done to confirm that the relationship indeed follows Rayleigh's analysis.

For this particular run, the jet velocity by the mass flow rate was 4.75 m/s, which was slightly higher than the average value of 4.64 m/s. The orifice diameter was 100 μm . The ejection pressure was 125 kPa. The frequency of vibration was 11.34 kHz. The best fit logarithmic curve shown in the figure is:

$$L_j = 7.5 \times 10^{-3} - 8.0 \times 10^{-4} \ln V_{\text{piezo}} , \quad (4.3.18)$$

where L_j is in meters, and the applied voltage, V_{piezo} , is in volts. Equation (4.3.13) and the above equation can be used to correlate the disturbance amplitude, δ , to the applied voltage, V_{piezo} . It can be written as:

$$\ln \delta = 1.46 \cdot \ln V_{\text{piezo}} - 23.45 \quad (4.3.19)$$

The above relationship was obtained by assuming the jet velocity of 4.75 m/s. The growth rate, q , was assumed to be 8660 1/s for the frequency of 11.34 kHz and for the material properties of pure tin at 553 K as listed in Table 4.1.

The average break-up length from Figure 4.5 was approximately 3.5 mm at 400 V for the experimental conditions listed above. In Figure 4.9, however, the break-up length at 400 V is approximately 4.5 mm, meaning the best fit curve would have been shifted downward if the average values were used. However, the slope would not have changed significantly.

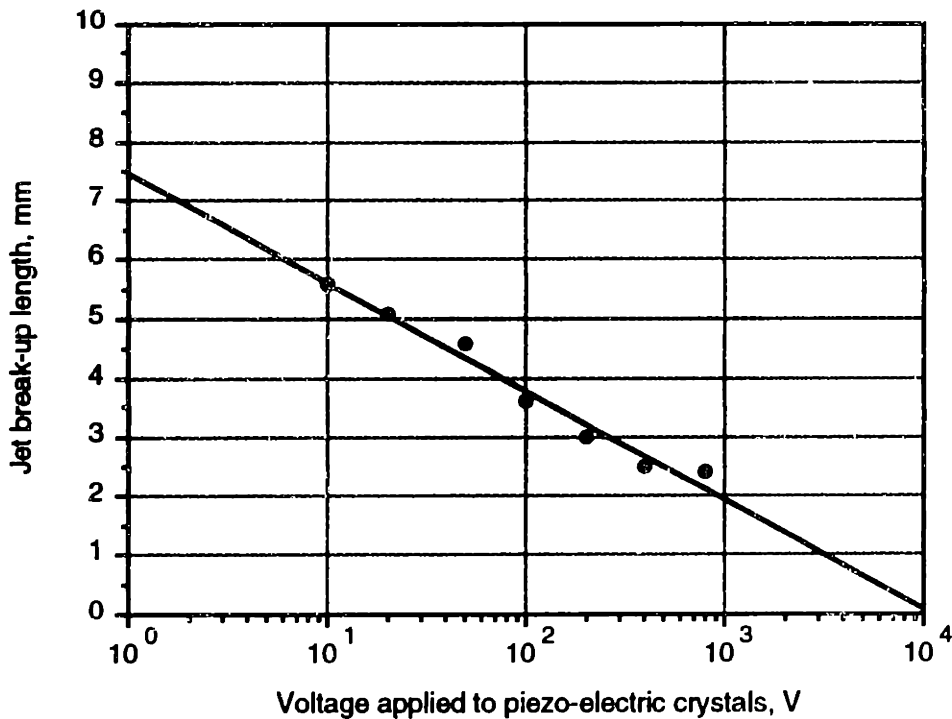


Figure 4.9 Jet break-up length with respect to amplitude. Jet diameter is 100 μm , jet velocity 4.75 m/s from the ejection pressure of 125 kPa, and forced vibration frequency 11.34 kHz.

4.4 Conclusions

This chapter discussed the experimental apparatus and procedures to investigate the break-up behavior of molten metal jets. The jet break-up length was used as one of the ways to determine the jet break-up behavior. The break-up length depends on the material properties, orifice diameter, jet velocity, and the frequency and amplitude of vibration.

The techniques used to estimate jet velocities were discussed. The jet velocity calculation was most sensitive to uncertainties in the orifice size. The jet break-up lengths were investigated for repeatability from run-to-run and for within-a-run. Although the break-up length stayed more or less the same for within-a-run, there were some discrepancies in the jet break-up length for the run-to-run. The discrepancies may have been contributed to the torque applied to the bolts connecting the crucible top plate to the top plate and to the screws connecting the crucible to the crucible bottom plate.

The jet break-up length versus the dimensionless number at different jet velocities was investigated. The results seemed to follow Rayleigh's analysis even though the minimum jet break-up length occurred at the dimensionless wavelength of near 4.0, as

opposed to the expected number of 4.51. This result, however, could have been improved with a more accurate estimation of jet velocities. It appeared that the break-up of molten tin behaved as that of inviscid flow as shown in Figure 2.3.

Break-up length versus amplitude was also investigated. The results followed Rayleigh's assumption that the initial amplitude of perturbation was inverse-logarithmically related to the break-up length. Since no direct measurement was performed to measure the amplitude of perturbation, the relationship between the voltage applied to the piezoelectric crystals and the amplitude was drawn from the experimental results.

Nomenclature

a	acceleration of displacement
C_{noz}	discharge coefficient of the flow through the nozzle
d_d	droplet diameter
d_j	initial jet diameter
f	frequency of imposed vibration
L_j	jet break-up length
M	total mass collected in a given time t
\dot{m}	mass flow rate
Oh	Ohnesorge number, $\frac{\mu}{\sqrt{\rho d \sigma}}$
ΔP	ejection pressure, or pressure difference, $P_c - P_o$
P_c	pressure of crucible
P_o	pressure of spray chamber (i.e., ambient pressure)
q	growth rate factor
Re	Reynolds number in a pipe, $\frac{\rho_l v_j d_j}{\mu}$
s	displacement of oscillation
t	time
V_{piezo}	voltage applied to the piezoelectric crystals
v_j	jet velocity
$v_{j,min}$	minimum jet velocity required to maintain the continuous laminar jet condition
γ	dimensionless wave number, $ka = \frac{2\pi a}{\lambda} = \frac{\pi d_j}{\lambda}$
δ	amplitude of perturbation applied to nozzle area

λ	wavelength, v_j/f
λ_d	wavelength between two droplets
λ/d_j	dimensionless wavelength
μ	viscosity of liquid
ρ_l	density of liquid
σ	surface tension of liquid
ω	frequency of oscillation

Chapter 5 **PRODUCTION AND CHARACTERIZATION OF MONO-SIZED BALLS**

5.1 Introduction

This chapter discusses how mono-sized balls of the eutectic Sn-38 wt.% Pb alloy were produced by controlling the break-up of a continuous laminar jet into uniform droplets and by then rapidly solidifying the droplets in a silicone oil bath (Yim et al., 1995; Yim et al., 1996). Although other sizes are possible, the process parameters were selected to produce droplets of a fixed diameter between 700 and 800 μm . The use of silicone oil assured fast cooling and minimum droplet merging. The balls showed high sphericity, a narrow size distribution (within $\pm 5\%$ of the target diameter), and a uniform, rapidly solidified microstructure. They also showed uniform re-melting characteristics due to their homogeneous microstructures. The present study suggests that the mono-sized Sn-Pb alloy balls produced by the UDS process may be applicable to the BGA packaging of integrated-circuit modules.

As the microelectronics industry rapidly progresses toward miniaturized, high-performance devices, it requires chip packages with higher input/output connections. One solution to this ever-increasing demand is the BGA package, a type of surface mount chip package. In the BGA technique, an electronic package is connected to a printed circuit board (PCB) by an array of solder balls. The package is placed in registration with the PCB and heated until the solder balls are melted to connect terminals on the printed circuit board or other substrates (Danner, 1994). The advantages of BGA packaging include high assembly yields; use of existing assembly equipment and processes; efficient use of printed wiring board (PWB) space; improved electrical performance; and lower assembly costs (Danner, 1994; Miks, 1994; Banks et al., 1995). Currently, solder balls for BGA packaging are produced by melting cut-solder wires in an oil bath for spheroidization followed by solidification (Foulke, 1995). For successful commercialization, however, the production of higher quality solder balls with tighter dimensional tolerance at lower cost is greatly desired.

Although Chapter 4 discussed the production of particles with diameters of 100 to 200 μm , the UDS process can produce larger particles as well. This process, however, requires a larger chamber with a sufficient height and width to achieve complete in-flight solidification of the droplets. For example, it is estimated that the chamber must be at least

6 m tall for complete solidification of 785 μm Sn-38 wt.% Pb droplets as shown in Figure 3.6. Alternatively, the use of a long chamber may be avoided by solidifying the droplets in an appropriate quench medium. In both approaches, the prevention of droplet merging before complete solidification is essential. However, droplet charging is hindered by the immersion of the droplets in a quench medium and is eliminated in producing large solder balls.

The present study reports on the production of 785 μm uniform balls of a Sn-38 wt.% Pb alloy by the latter approach. The particle size of 785 μm was chosen because of the potential use in BGA packaging, for which 750 μm solder balls are currently used.

5.2 Experimental Procedure

5.2.1 Production of solder balls

The experimental apparatus and procedures were similar to those discussed in Chapter 4. The apparatus, however, was slightly modified as shown in Figure 5.1 to include a glass cylinder containing Dow Corning 704 diffusion pump fluid (silicone oil), placed in a gas-tight Pyrex glass chamber to accommodate the production of larger particles. A solenoid vibrator replaced the piezoelectric crystals. As mentioned above, large droplets allowed to solidify in oil eliminated the need for a longer chamber. The jet break-up length, L_j , increases as the orifice diameter (i.e., jet diameter) increases, as seen in the following equation:

$$L_j = \ln\left(\frac{d_j}{2\delta}\right)v_j \left[\left(\frac{\rho_l d_j^3}{\sigma_l}\right)^{1/2} + \frac{3\mu_l d_j}{\sigma_l} \right], \quad (5.2.1)$$

where d_j is the orifice or jet diameter, ρ_l the density, σ_l the surface tension, and μ_l the viscosity. One of the problems of a long jet break-up length is that the jet break-up is inconsistent. To achieve a shorter break-up length and a consistently clean break-up of jets, the perturbation amplitude should be increased as shown in the above equation. However, the piezoelectric crystals cannot deliver a perturbation amplitude sufficiently high to yield a clean break-up of a jet into a train of uniform droplets. Thus, a solenoid vibrator, which can deliver a high amplitude at a low frequency, was used to provide a perturbation amplitude to the jet of molten eutectic solder alloy.

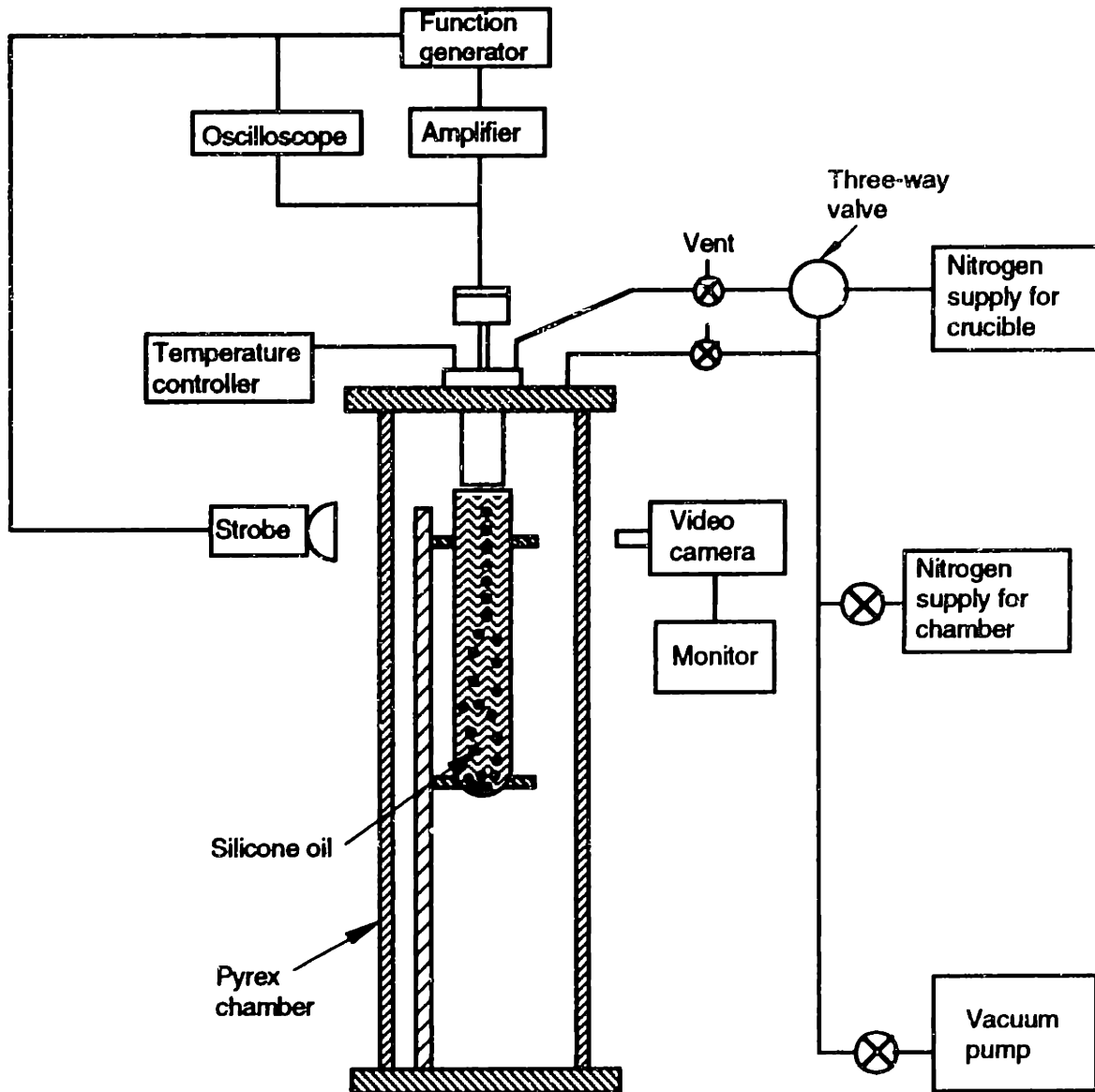


Figure 5.1 Uniform Droplet Spray apparatus for producing large solder balls.

In each experiment, about 0.5 kg of the eutectic solder alloy was melted in the crucible. The chamber was evacuated to about 50 mTorr and back-filled with nitrogen gas containing less than 5 ppm oxygen to the gauge pressure of 35 kPa (5 psig). This process was repeated twice more before melting the alloy. After reaching a melt temperature of 508 K (235 C), a laminar jet of the molten alloy was ejected by gas pressure between 30 to 38 kPa (4.5 to 5.5 psia). This resulted in a laminar jet velocity of approximately 2 m/s. The jet was subjected to forced vibrations at a frequency between 0.9 and 1.1 kHz transmitted by the solenoid vibrator, which caused the controlled break-up of the laminar jet into uniform droplets. The uniform droplets were quenched in a silicone oil bath placed directly below the orifice. The distance between the orifice and the oil bath was varied to

optimize the jet break-up and droplet quenching process. Droplet charging was initially eliminated in this procedure as it was hindered by the immediate quenching of the droplets in the oil bath. The solidified balls were ultrasonically cleaned in acetone and then subjected to surface and microstructural characterization.

5.2.2 Jet break-up

Several trial runs were conducted to optimize the jet break-up and droplet-quenching processes. The droplets were generated in a nitrogen atmosphere to check the droplet uniformity without an oil-bath quench. The break-up process was monitored by a CCD camera while adjustments were made to the frequency of vibrations and ejection pressure. Table 5.1 lists the final process conditions used.

Table 5.1 Process conditions used to produce Sn-38 wt.% Pb balls

Orifice diameter	406 μm
Orifice-oil distance	2 to 50 mm
Melt temperature	508 K
Ejection pressure (differential)	30 to 38 kPa (4.5 to 5.5 psia)
Initial jet velocity	2 m/s
Vibration frequency	0.9 to 1.1 kHz
Oil bath	Diffusion pump fluid (Silicone oil)
Oil temperature	298 K

For the 406 μm diameter orifice used, the optimal vibration frequency and ejection pressures were 1 kHz and 38 kPa (5.5 psia), respectively. This set of conditions yielded uniform 785 μm diameter droplets, traveling vertically downward at an initial droplet velocity of approximately 2 m/s. After the frequency and ejection pressure were adjusted to allow the jet to break into a train of uniform droplets, a bath containing silicone oil was placed directly under the orifice to rapidly solidify the droplets as shown in Figure 5.1. The distance between the orifice and the oil surface was varied from 2 to 50 mm. When this distance was larger than about 20 mm, the jet broke entirely above the oil surface, with many droplets merging as they entered the oil and solidifying into coalesced forms. At distances less than 5 mm, the jet break-up occurred in the oil, producing mostly spherical, uncoalesced droplets. See Figure 5.2 for a schematic diagram.

With the values for the variables used in the present study (see Table 5.1), the break-up distance in nitrogen was estimated from to be about 10 to 15 mm from the video pictures monitored by the CCD camera. The break-up length in silicone oil is expected to be less since jet velocity attenuates in oil. However, no attempts were made to calculate or measure that break-up distance.

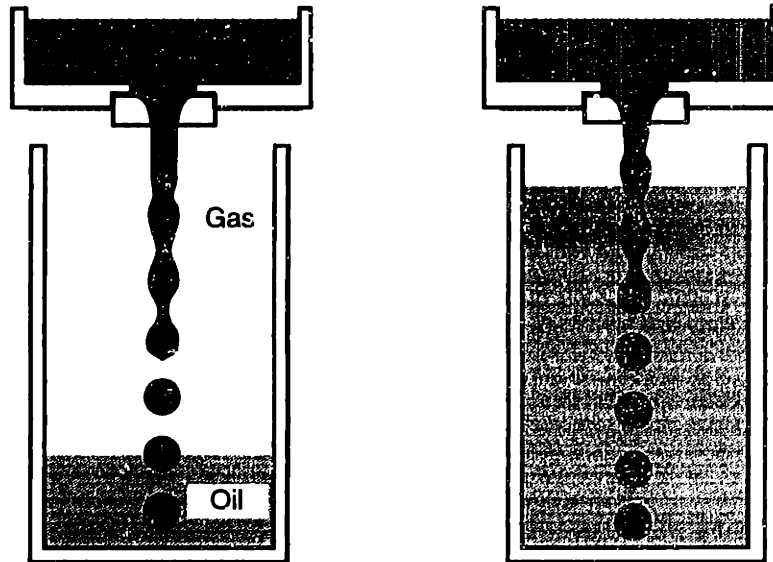


Figure 5.2 Jet break-up in gaseous atmosphere and in oil.

Section 2.5 in Chapter 2 discussed the break-up behavior of a liquid jet in a liquid, and the differences of the maximum instability for such cases from the break-up behavior of a liquid jet in a quiescent gas environment. Figure 2.8 shows the relationship between the viscosity ratio and the dimensionless wave number, γ , by Tomotika (1935). The viscosity ratio is defined as the viscosity of a liquid jet (liquid eutectic tin/lead alloy in this case) divided by the viscosity of the ambient liquid (silicone oil in this case). The viscosity of eutectic tin/lead alloy at the melting temperature is approximately 2.15×10^{-3} kg/(m · s). The viscosity of silicon oil at 298 K is approximately 36.3×10^{-3} kg/(m · s). Thus, the viscosity ratio should be approximately 0.06. This ratio should result in the dimensionless wave number of 0.54. Since the dimensionless wave number is defined as $\pi d_j / \lambda$, the dimensionless wavelength, λ / d_j , should be about 5.8, which is higher than the dimensionless wavelength for the maximum instability for the jet break-up in a quiescent gas environment. Nevertheless, this should not pose a serious problem in the breaking of the liquid alloy jet in a silicone oil.

5.2.3 Characterization of solder balls

The solidified balls were examined for their appearance, shape, size and size distribution, and microstructure by optical microscopy and by scanning electron microscopy (SEM). Standard procedures were used in the metallographic study. Energy Dispersive X-ray (EDX) Fluorescence analysis was also performed to determine the distribution of the Sn and Pb-rich phases in the balls. The melting characteristics of the balls were studied by a differential scanning calorimeter (DSC) (Perkin-Elmer, Model No. DSC7). One ball was placed in an aluminum pan, which weighed 16.256 mg. The aluminum pan with the ball and an aluminum pan without a ball were placed in the calorimeter. Both samples were heated at a rate of 10 K/min while maintaining the same temperature for both samples. Since the pan which contained the ball weighed more, it took more energy to maintain its temperature than the pan which did not contain the ball. The difference between the heating rates was recorded. For comparison, the same procedures were repeated with commercial solder balls of a eutectic composition produced by melting chopped wire in hot oil and solidifying the spheroidized droplets.

5.3 Results and Discussion

5.3.1 Appearance and sphericity

The uniform balls produced in this study showed a smooth surface and a spherical shape as shown in Figure 5.3. The smooth surface can be attributed to the use of silicone oil which acts as a smooth mold. No quantitative measurements of the sphericity were attempted. However, the process conditions used permitted the droplets to sufficiently spheroidize before they had solidified, resulting in reasonable sphericity. In general, droplet sphericity should improve with increasing superheat of the jet so that there is enough time for spheroidization before the onset of solidification. However, if the temperature of the liquid metal jet is too high, it may also give rise to droplet merging. Choosing the optimal superheat and quench rate, thus, should further improve the sphericity.

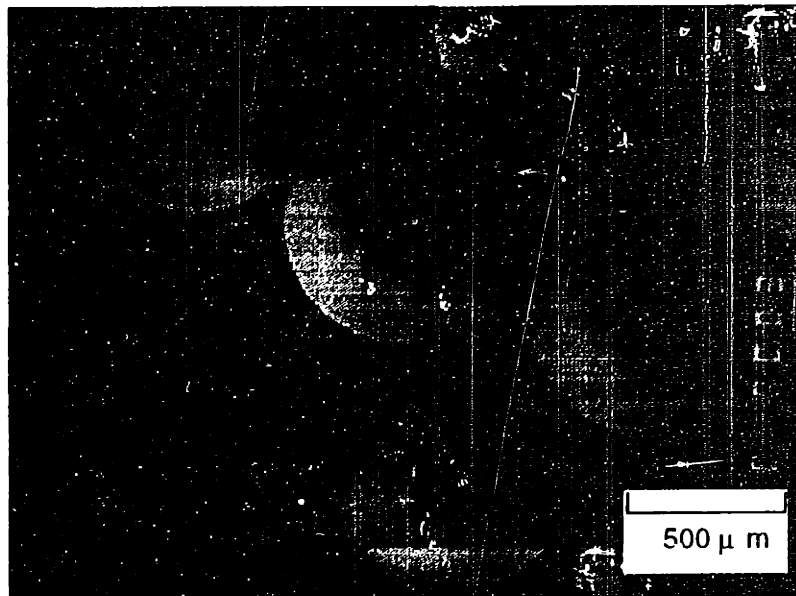
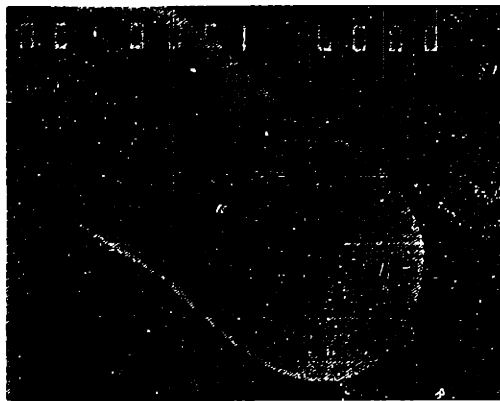


Figure 5.3 SEM picture of Sn-38 wt.% Pb balls produced by the UDS process at 40x magnification. The balls were produced with an orifice of diameter 402 μm , initial jet velocity 2 m/s and vibration frequency 1 kHz.

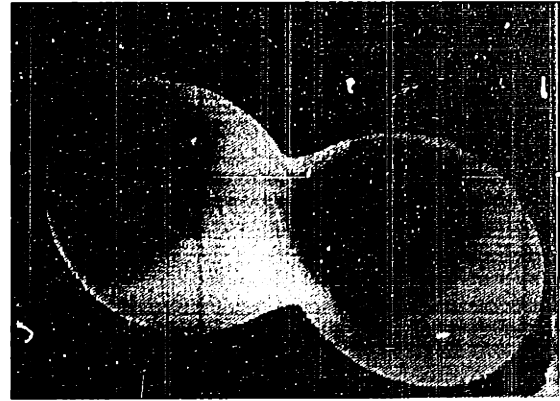
Nevertheless, some irregularly shaped particles formed due to the merging of droplets as shown in Figure 5.4. The irregular particles were mostly either cylindrical or dumb-bell shaped, depending on the liquid fraction of the droplets when they merged. When the process conditions were not optimized to induce uniform jet break-up, finer droplets or “satellites” (Pimbley and Lee, 1977) formed between larger droplets and merged with them, forming snowman-shaped particles. The percentage of these irregular particles was particularly low when the jet break-up occurred in the silicone oil. The spherical particles showed excellent flowability and could easily be separated from the irregular ones by rolling them over an inclined surface.

The use of silicone oil also decreases the chance of droplet merging by providing high quench rates. Heat transfer simulation based on Newtonian cooling (applicable when the Biot number is less than about 0.01) estimates that the solidification time of the 785 μm droplets at 508 K in the silicone oil is about 0.3 seconds. Thus, they were estimated to have fully solidified within 20 mm beneath the oil surface. In contrast, if droplets of the same size were to solidify in a nitrogen environment, it would take about 1.1 seconds, or 6 m, to fully solidify. The high quench rate and the decrease in droplet velocity due to the high drag force caused by the high viscosity of the oil are the primary reasons for the shorter distance in the former case. The droplet merging within this distance was expected to further decrease when the droplets were charged. The yield of spherical uniform balls

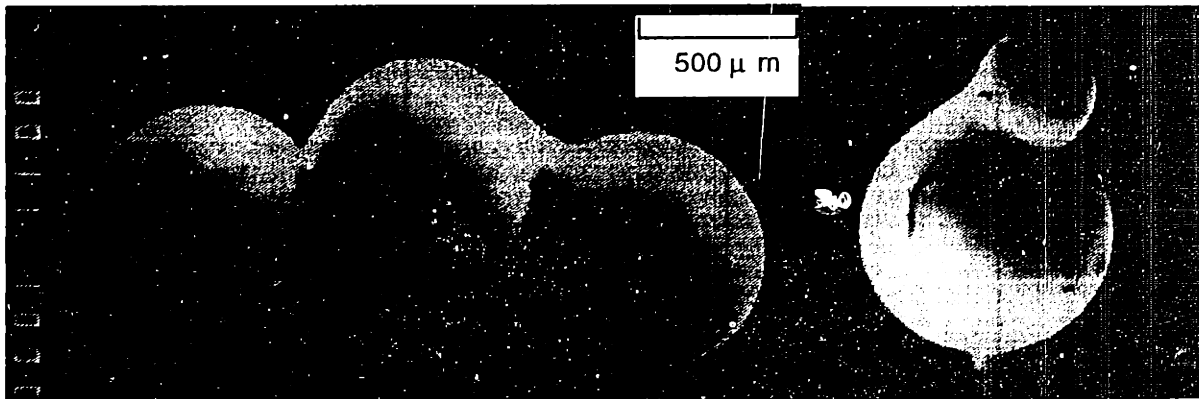
can be improved to 100% by further optimizing the break-up, charging, and quenching processes.



Cylindrical



Dumb-bell



Triplet

Snowman

Figure 5.4 SEM picture of irregular-shaped particles at 40x magnification.

5.3.2 Size distribution and production yield

Figure 5.5 shows the size distribution of 150 balls picked randomly from one of the batches produced. Most of the balls are in the narrow distribution of $\pm 5\%$ of the mean diameter of $785 \mu\text{m}$ with a standard deviation of $26 \mu\text{m}$, although 16 balls fall outside the specified range. Powders in the range of 100 to $200 \mu\text{m}$ produced by the UDS process have shown to be within $\pm 3\%$ of the nominal size. The improvement in size distribution with smaller powders can be explained by the variation of processing conditions, in particular, the ejection pressure.

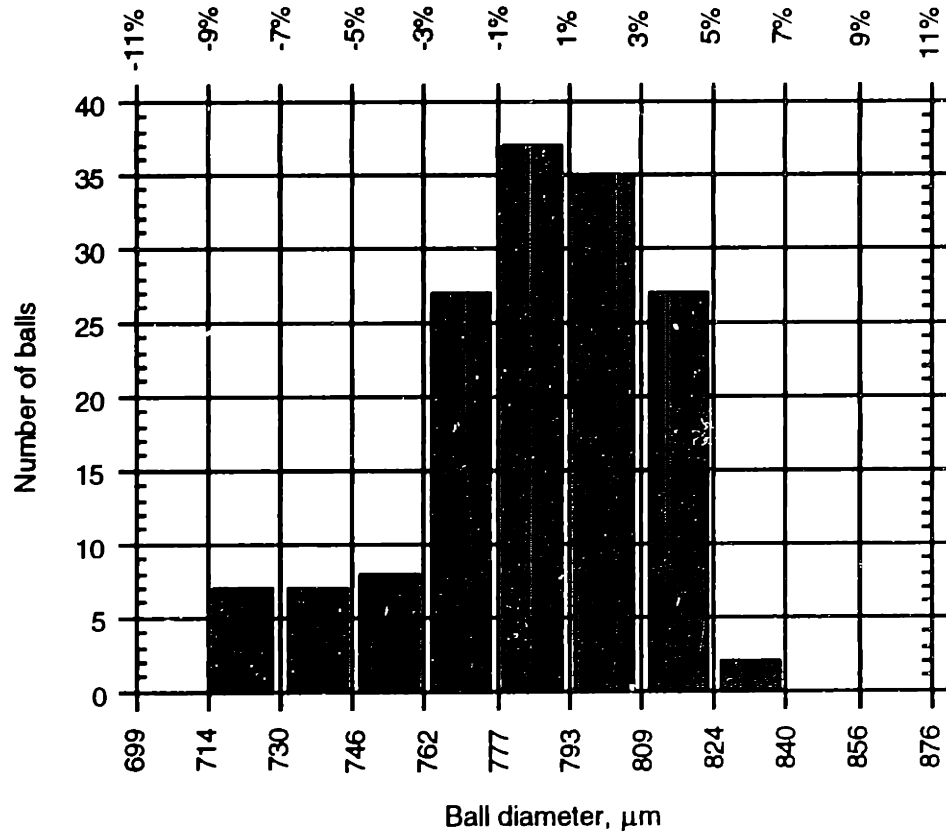


Figure 5.5 Size distribution of the Sn-38 wt.% Pb balls produced by the UDS process. The balls were produced with an orifice of diameter 402 μm , initial jet velocity 2 m/s and vibration frequency 1 kHz. The mean diameter is 785 μm .

The ejection pressure required to produce 785 μm balls ranges from 30 to 38 kPa. It is about 90 to 160 kPa for producing 200 μm powders. The jet velocity which determines powder size can be estimated by:

$$v_j = C_{noz} \sqrt{\frac{2 \cdot \Delta P}{\rho_l}} \quad (5.3.1)$$

As can be seen in equation (5.3.1), the ejection pressure has more influence on the jet velocity when producing larger diameter balls. Thus, variation in the ejection pressure creates more deviation in the size of larger balls. Variation of ejection pressure could come from three sources: pressure settings; pressure change due to the hydrostatic pressure; and pressure increase in the spray chamber during the run.

The hydrostatic pressure is caused by the height of the melt in the crucible. The inside diameter of the crucible was 38 mm, the density of the eutectic alloy in a liquid state was 8050 kg/m³, and the weight of the melt approximately 0.5 kg. Thus, the height of the melt inside the crucible was around 55 mm, which resulted in a hydrostatic pressure of 4.5 kPa. The chamber pressure typically rises by as much as 3.5 kPa during an experiment. If the gauge pressure of 72 kPa (10.5 psig) was applied to the crucible, the ejection pressure becomes about 38 kPa (5.5 psia). Thus, in the beginning of a run, the actual ejection pressure with the hydrostatic pressure was about 42.5 kPa (38+4.5). Near the end of a run, however, the actual ejection pressure became about 34.5 kPa (38-3.5). Thus, the pressure variation during an experiment could have been as much as 8 kPa.

Assuming a discharge coefficient of 0.63 (an averaged value from the runs), the jet velocity in the beginning and near the end of the spray were 2.05 and 1.84 m/s, respectively. Droplet diameters resulting from these jet velocities can be obtained as shown in equation (3.2.9):

$$d_d = d_j \left(1.5 \frac{v_j}{f d_j} \right)^{1/3} = d_j \left(1.5 \frac{\lambda}{d_j} \right)^{1/3} . \quad (5.3.2)$$

Thus, the diameters of droplets from these jet velocities, assuming the jet diameter of 406 μm and the frequency of 1 kHz, were 797 and 769 μm, respectively. If the average value of jet velocity, 1.95 m/s, or the dimensionless length of 4.80, is used, the droplet diameter becomes approximately 785 μm. Thus, the pressure variation due to the hydrostatic pressure and the pressure increase during run resulted in ±5% of jet velocity estimation, which can be translated into about ±1.5% droplet diameter variation.

This particular batch was produced by breaking up the jet in the oil at a vibration frequency of 1 kHz with an ejection pressure of 38 kPa (5.5 psia), resulting in an initial jet velocity of approximately 2 m/s. Other batches showed similar size distributions after irregular particles were removed from the batches. Again, the mean diameter can be varied by adjusting the process parameters.

The frequency response of the solenoid vibrator may not be as good as the piezoelectric crystals, which can contribute to the size variation. The formation of satellites during the jet break-up in the silicone oil can also contribute to the size variation. With further optimization, all balls can be produced to within ±5% of the mean diameter.

Controlling the diameter of solidified balls requires a correction for solidification shrinkage. For the Sn-38 wt.% Pb alloy, a volume shrinkage occurs upon solidification

because of the density change from 8050 kg/m³ in a liquid state to 8400 kg/m³ in a solid state. The resulting particle size upon solidification becomes:

$$d_{d,s} = \left(\frac{\rho_l}{\rho_s} \right)^{1/3} d_{d,l} = K_c d_{d,l}, \quad (5.3.3)$$

where ρ_l is the density of the alloy in a liquid state, ρ_s the density of the alloy in a solid state, and K_c is the correction factor. Thus, the correction factor should be 0.986. This translates into approximately a 1.4 % linear shrinkage, e.g., a 785 μm molten alloy droplet solidifies into a 774 μm solid particle. This is in a reasonable agreement with the observed mean diameter of 785 μm . Since the wavelength depends only on the vibration frequency and jet velocity, the droplet diameter can be controlled directly via these process parameters. Lower wavelengths and/or smaller orifice diameters can be used to precisely decrease the droplet diameter to a desired value; for example, 750 μm .

The production yield of the current procedure is listed in Table 5.2. This represents a total of 6 runs. Run numbers 3, 4, and 5 were divided into two batches for sorting. The balls collected in the silicone oil were cleaned in soapy water. They were then separated on a surface at a 5° angle, on which the balls were allowed to roll down about 300 mm. Spherical balls rolled down straight to the bottom where they were collected. The irregularly shaped balls as shown in Figure 5.4 were not able to roll down straight, rather they did not roll or they rolled to the side. These balls were then swept aside. This procedure was continued until all non-spherical balls were sorted out.

Table 5.2 Yield of mono-sized balls

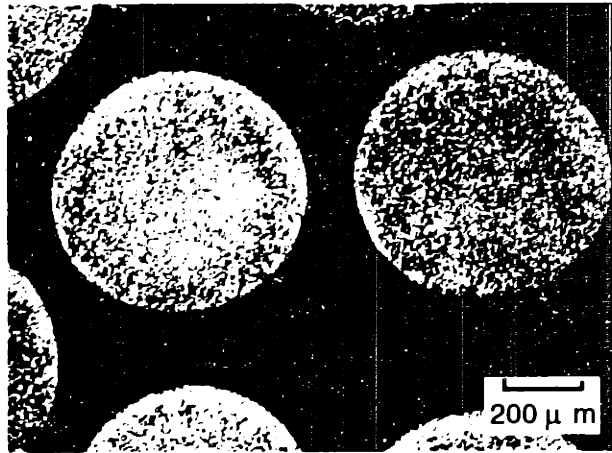
Batch number	total weight collected (g)	total weight of good balls (g)	percentage yield (%)
1	159	101	64
2	203	126	62
3A	196	144	73
3B	183	123	67
4A	193	136	70
4B	181	124	69
5A	147	88	60
5B	231	146	63
6	121	86	71
total	1614	1074	67

As shown in Table 5.2, the total weight collected was 1614 grams. The weight of spherical balls after the sorting was 1074 grams, resulting in the total percentage of yield at near 70%. This can, however, be improved to 100% with the further optimization of the system as discussed in the previous section.

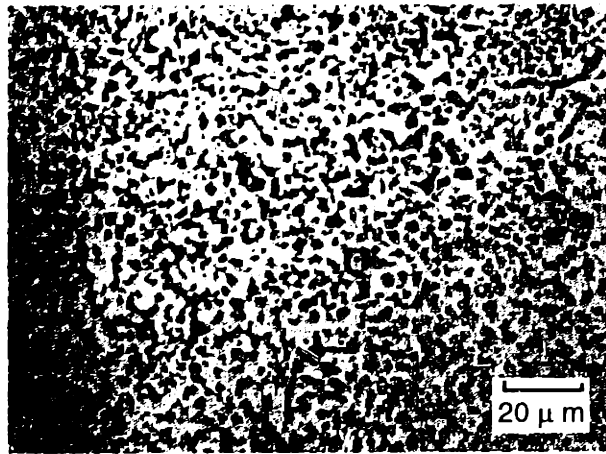
5.3.3 Microstructures and re-melting characteristics

Figure 5.6 shows optical micrographs of the cross-sections of uniform balls at low and high magnifications. A cross-section of a commercial ball of similar composition is shown for comparison. Both eutectic samples present an equiaxed two-phase microstructure. Back-scattered electron imaging (Figure 5.7) and EDX analysis confirm that the darker phase in Figure 5.6 is the Pb-rich phase and that the lighter phase is the Sn-rich phase. The UDS samples show finer grains and more uniform distributions of the two phases than the commercial ball, which shows a bimodal distribution of grain sizes of the Pb-rich phase. The equiaxed microstructures suggest that the commercial balls experienced undercooling before solidification. This is expected because molten alloy droplets emulsified in a non-oxidizing liquid may undercool substantially prior to solidification (Turnbull and Cech, 1950; Perepezko, 1980). Although the extent of the undercooling in the Sn-38 wt.% Pb droplets is not known, the mode of solidification in the droplets was most likely dendritic (Chu et al., 1984).

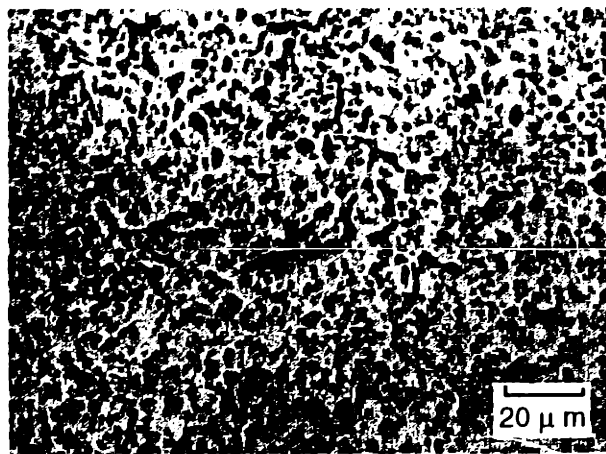
The dendrites in the Sn-38 wt.% Pb droplets are considered to be those of the Pb-rich phase (Chu et al., 1984). The dendrites, however, may have disintegrated and coarsened during solidification into the observed equiaxed spheroidized microstructures. The bimodal grain sizes of the Pb-rich phase in the commercial balls suggest that the mode of solidification in these balls was dendritic at first, producing the coarser Pb-rich grains, and eutectic in later stages, forming the eutectic microstructure containing the finer Pb-rich particles. This Pb-deficient, irregular eutectic microstructure resulted from Pb-depletion in the liquid caused by the formation of the primary Pb-rich dendrites. The absence of lamellar microstructures in the UDS balls suggests that the mode of solidification in these balls was almost entirely dendritic, reflecting the high quench rates caused by the cold silicone oil.



(a)



(b)



(c)

Figure 5.6 Optical micrographs of cross sections of solder balls. (a) 50x magnification view of 785 μm Sn-38 wt.% Pb balls produced by the UDS process, (b) 500x magnification view of (a), and (c) 500x magnification view of a 750 μm commercial solder ball.

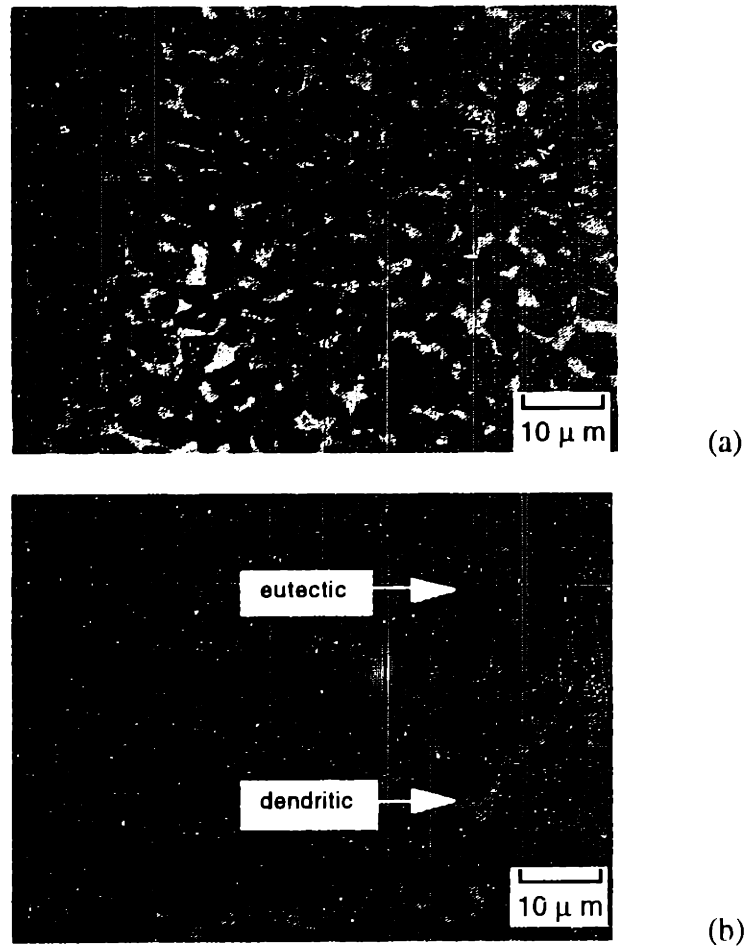


Figure 5.7 Back-Scattered electron images (1000x magnification) of cross sections of solder balls. (a) 785 μm Sn-38 wt.% Pb balls produced by the UDS process, (b) 750 μm commercial solder ball. The Pb-rich phase appears light and the Sn-rich phase dark.

Figure 5.8 shows the results of the DSC study performed on balls produced by the UDS and commercial processes. The UDS ball weighed 2.493 mg, which implied a diameter of 828 μm , assuming that the density of eutectic solder alloy is 8400 kg/m^3 . The commercial ball weighed 2.013 mg, which indicated a diameter of 771 μm . Only the heating portions of the DSC curves which show the eutectic melting are presented. Although the DSC curves are similar, the UDS balls produced a somewhat narrower exothermic peak. It suggests uniform re-melting characteristics and a slightly higher eutectic temperature of 455.9 K, indicating a higher binary purity.

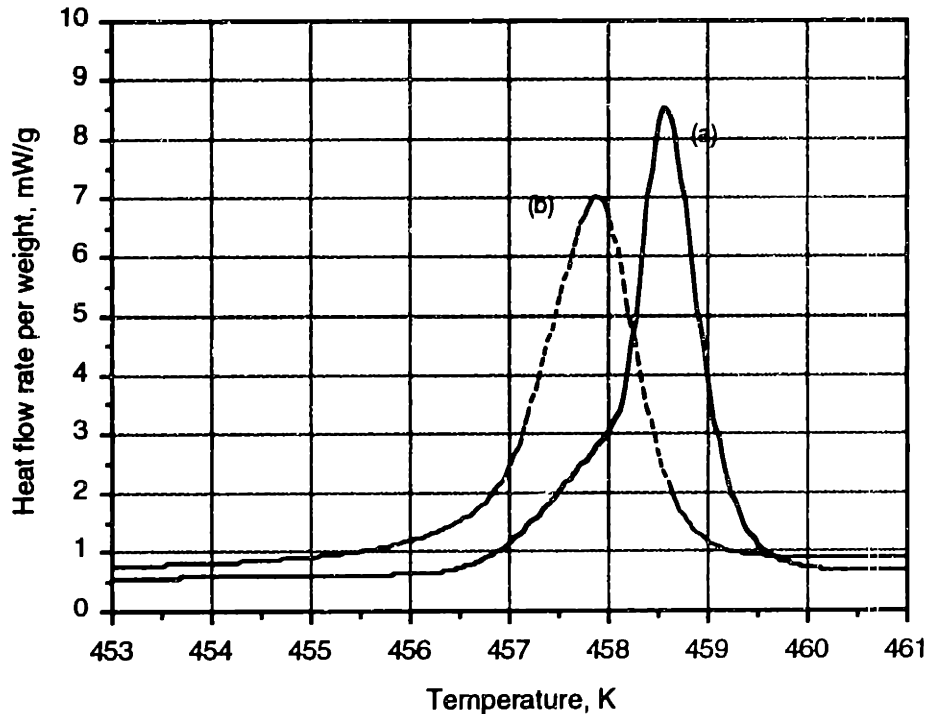


Figure 5.8 Heating DSC curves of solder balls. (a) 785 μm Sn-38 wt.% Pb ball produced by the UDS process, (b) 750 μm commercial solder ball.

The eutectic tin/lead alloy melts at 455.9 K as can be seen in Figure 5.9 (Barrett et al., 1973). The gradual heat generation prior to the eutectic melting of the UDS sample is probably due to grain coarsening. Such uniform re-melting characteristics should ensure the improved reflowing characteristics preferred in solder applications such as BGA IC packaging.

5.4 Process Viability

For the production of large ($> 500 \mu\text{m}$) balls, the jet break-up and oil quench process has an advantage over the jet-break up process in gaseous atmosphere in that the former does not require a long, wide chamber for in-flight droplet solidification. This translates directly into a lower capital cost. The quality of the balls is also improved by use of the oil quench which yields uniform microstructures, smooth surfaces, and minimum particle merging. The present results suggest that this process can readily incorporate a multiple-orifice approach without adversely affecting the break-up process; thus, large quantities of balls can be produced. For example, a 10-orifice apparatus may be used to produce 750 μm uniform solder balls at rates of up to about 75 kg/hr. Even the “one hour”

production from a single-orifice apparatus can provide enough balls for 15,000 BGA chips, each of which uses 225 solder balls.

While the UDS process is not temperature-limited, the wire-melting process is temperature-limited by the oil boiling temperature as the oil bath temperature is raised. Therefore, alloys with higher melting temperature cannot be transformed into balls when conventional wire-melting process is used. However, the UDS process can readily accommodate alloys with high melting temperatures (e.g., lead-free alloys).

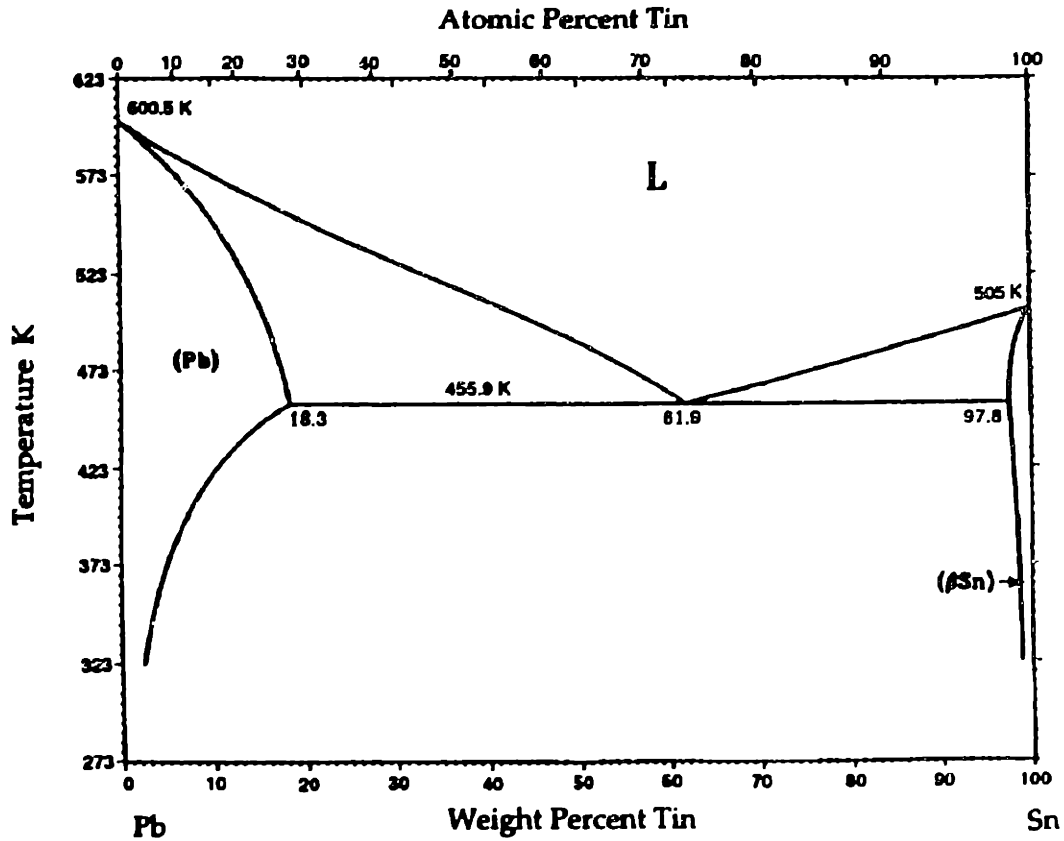


Figure 5.9 Phase diagram of lead-tin alloy system.

5.5 Conclusions

Uniform Sn-38 wt.% Pb alloy balls with 785 μm diameters have been produced by the controlled break-up of a laminar jet and quenching in silicone oil. The balls produced in this study showed a smooth surface, a high degree of sphericity, narrow size distributions (within 5% of nominal diameter), fine, uniform microstructures, and uniform re-melting

characteristics. Ways to optimize the process conditions to improve further these properties were discussed. This jet break-up (UDS) process potentially offers an efficient and economical means for producing uniform alloy powders, particles, and balls.

Nomenclature

C_{noz}	discharge coefficient of a nozzle
d_d	droplet diameter
$d_{d,l}$	droplet diameter in a liquid state
$d_{d,s}$	droplet diameter in a solid state
d_j	initial jet diameter, $2a$
f	frequency of imposed vibration
K_c	correction factor for shrinkage due to solidification
v_j	Jet velocity
L_j	jet break-up length
ΔP	ejection pressure, or pressure difference, $P_c - P_o$
P_c	pressure of crucible
P_o	pressure of spray chamber (i.e., ambient pressure)
γ	dimensionless wave number, $\frac{\pi d_j}{\lambda}$
δ	amplitude of disturbance applied to nozzle area
λ	wavelength, $\frac{v_j}{f}$
λ/d_j	dimensionless wavelength
μ_l	viscosity of liquid
ρ_l	density of liquid
ρ_s	density of solid
σ_l	surface tension of liquid

Chapter 6 EFFECTS OF OXIDATION ON JET BREAK-UP BEHAVIOR: THEORY

6.1 Introduction

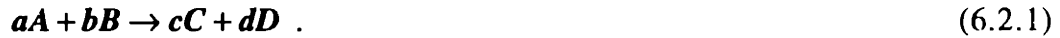
Successful generation of uniform droplets is imperative in the UDS process. If a molten metal as opposed to non-oxidizing liquid is to be used as the spraying material, it is important to understand the role of metallurgical reactions on the jet break-up process. Most metals react with oxygen to form oxide layers on the surface. Material properties on the jet surface may change as a result of the reaction. For example, the surface tension of molten metal may decrease, while the viscosity may increase. Such changes in material properties will retard the jet break-up process, that is, the break-up length of jet will increase. Even worse, an oxide layer may form on the molten metal jet surface, which may cause the jet to form fibers as shown in Figure 1.5. For the UDS process to be viable and reliable, effects of the chemical reactions between metal and ambient gas in the spray chamber have to be identified, investigated, and accounted for.

There are many possible reactions on the surface of a metal jet while it is breaking into a train of uniform droplets. For example, molten aluminum reacts with oxygen in air to form aluminum oxide and with nitrogen to form aluminum nitride. The formation of aluminum nitride on the jet surface can prevent jet break-up, much as aluminum oxide does. Though results of aluminum jet break-up will not be discussed in this thesis, it has been observed that consistent break-up of laminar aluminum jets can be better attained if they are sprayed into an argon environment rather than into a nitrogen environment. In this thesis, investigation will be limited to how the surface reaction between molten tin and oxygen, i.e., how surface oxidation of pure liquid tin, affects jet break-up.

In this chapter, theories of oxidation from the literature are briefly reviewed. Thermodynamic equilibrium calculation shows that oxidation takes place under typical UDS experimental conditions. The oxidation rates are reviewed and used to calculate the oxide layer thickness. A hypothesis on the change of material properties as a result of surface oxidation is suggested and discussed. Conclusions based on the review of oxidation theories are drawn to shed light on the effects of surface oxidation and to direct experimental approaches and techniques.

6.2 Thermodynamic Equilibrium Conditions for Oxidation

As the molten metal jet issues from the orifice, it comes in contact with gases in the spray chamber. This section investigates whether a chemical reaction between the metal and gas is favorable. The thermodynamic equilibrium condition shows whether a certain chemical reaction is favorable under certain conditions, such as pressure or temperature. The equilibrium condition can be determined by calculating the Gibbs free energy of reaction. Consider the following gas-phase chemical reaction:



The Gibbs free energy associated with the above reaction becomes:

$$\begin{aligned} \Delta G &= G_{\text{products}} - G_{\text{reactants}} \\ &= (G_C + G_D) - (G_A + G_B) \\ &= [(G_C^\circ + G_D^\circ) - (G_A^\circ + G_B^\circ)] + RT \ln P_C^c P_D^d - RT \ln P_A^a P_B^b \\ &= \Delta G^\circ + RT \ln \frac{P_C^c P_D^d}{P_A^a P_B^b} \end{aligned} \quad (6.2.2)$$

At equilibrium, $\Delta G = 0$. Thus, equation (6.2.2) becomes:

$$\Delta G^\circ = -RT \ln \frac{P_C^c P_D^d}{P_A^a P_B^b} \quad (6.2.3)$$

The equilibrium reaction constant, K , is defined as:

$$K = \frac{P_C^c P_D^d}{P_A^a P_B^b} \quad (6.2.4)$$

Combining equations (6.2.3) and (6.2.4), the standard Gibbs free energy of the reaction can be written as:

$$\Delta G^\circ = -RT \ln K \quad (6.2.5)$$

Consider the equilibrium between a metal, M , to form oxide M_xO_2 , and a gaseous oxygen of potential, P_{O_2} :



Assuming that the metal and its oxide are in their standard states (i.e., 1 atmospheric pressure), the equilibrium constant, K , corresponding to this reaction is simply the reciprocal of P_{O_2} :

$$K = \frac{1}{P_{O_2}} \quad (6.2.7)$$

and:

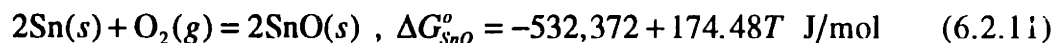
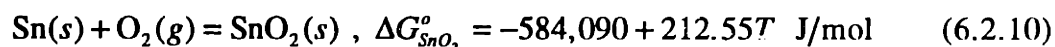
$$\Delta G^\circ = RT \ln P_{O_2} , \quad (6.2.8)$$

or

$$P_{O_2} = \exp\left(\frac{\Delta G^\circ}{RT}\right). \quad (6.2.9)$$

If the oxygen potential is lower than $1/K$, the metal is not oxidized (or any oxide decomposes); if it is higher, the metal is oxidized. Figure 6.1 shows a plot of the standard free energies of formation of various oxides vs. temperature (Lupis, 1983). Though the diagram gives equilibrium data, it is useful for the conditions at which oxidation takes place.

The reaction between tin and oxygen may result in two different oxides, stannic oxide (SnO_2) and stannous oxide (SnO):



Equations (6.2.10) and (6.2.11) show the free energy of formation of stannic and stannous oxides, respectively (Jacob and Jeffes, 1971; Hasouna et al., 1983; Prabhakar and Kapoor, 1993).

Thus, the equilibrium partial pressure of oxygen can be calculated from the free energy formations for stannic and stannous oxides, equations (6.2.10) and (6.2.11), and the temperature at which the reaction takes place.

The equilibrium partial pressures of oxygen at 553 K are 8.4×10^{-45} atm and 6.6×10^{-42} atm for stannic and stannous oxides, respectively. At 298 K, they are 5.2×10^{-92} atm and 6.2×10^{-85} atm. The equilibrium partial pressures for the formation of stannous oxide can also be obtained from Figure 6.1. The partial pressures of oxygen

listed above are not attainable in practice. Thus, oxidation will take place under the UDS experimental conditions.

The thermodynamics of equilibrium only indicate whether oxidation is likely to take place under certain conditions. It does not address, however, how fast the oxide layer grows. The growth of the oxide layer can be estimated by investigating the kinetics of oxidation.

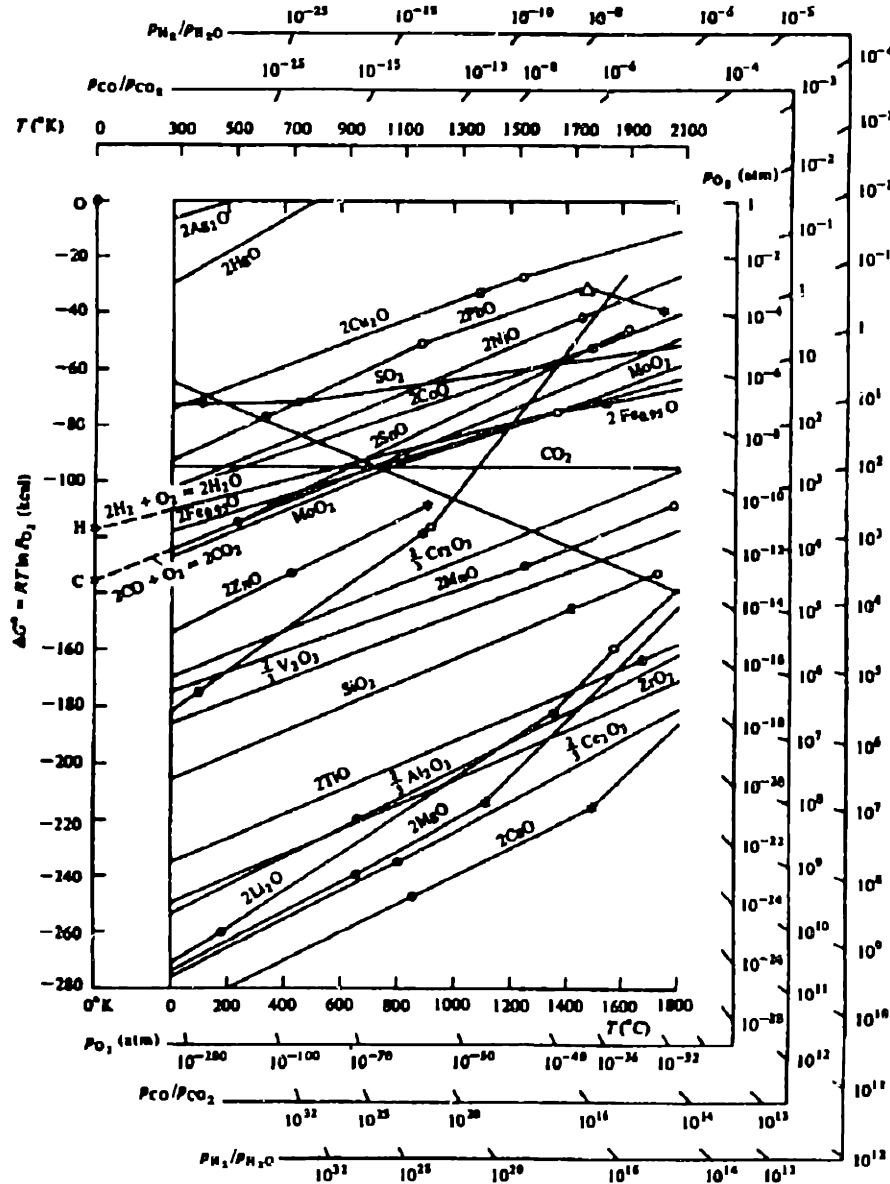


Figure 6.1 Standard free energy of formation of some selected oxides. ΔG° corresponds to the reaction $(2x/y)M + O_2 = (2/y)M_xO_y$. The symbol • and * identify the melting and boiling points, respectively, of the metals; o and Δ identify the melting and boiling points, respectively, of the oxides (Lupis, 1983).

6.3 Oxidation of Metals

Oxidation takes place when the oxygen molecules in the gaseous environment arrive at the surface of molten metal, where they react to form metal oxide. The previous section showed that it takes place under the typical UDS operating conditions. This section discusses how the oxygen molecules may be transported to the surface, how they react to form metal oxide and how fast the oxide layer grows. Possible mechanisms of oxidation are also discussed.

Figure 6.2 shows the break-up process of a laminar jet as it exits from the orifice. Assuming that the oxygen molecules on the metal surface are completely consumed in the reaction, the concentration of oxygen molecules on the metal will be smaller than that in the ambient environment. Thus, the oxygen molecules in the bulk state will move to the surface, where further oxidation takes place. Unlike the initial oxidation step, the oxygen molecules now come in contact with the oxide layer instead of pure metal. For further oxidation to occur, oxygen has to diffuse through the oxide layer to the metal-metal oxide interface, where the reaction occurs.

Initial oxidation in which the oxide layer is not present will be discussed as schematically shown in Figure 6.2. By investigating the parameters which affect the growth of the oxide layer, it can be determined whether oxidation is limited by the transport of oxygen molecules in the gas phase, or by transport of oxygen in the oxide phase, or by the consumption of oxygen molecules at the oxide-metal interface due to the reaction. Although the oxidation problem in the initial stage is highly transient, steady state assumptions will be utilized to identify the possible limiting cases. It will be assumed that the concentration of oxygen molecules in the bulk remains constant, and it will be further assumed that the temperature of the molten metal jets does not change with distance from the nozzle.

In the following model, the transport of oxygen molecules in the oxide layer will be excluded. As shown in Figure 6.2, oxygen molecules are transported from the bulk of gas phase to the surface with flux j_1 , where the number of atoms or molecules crossing a unit area in a unit time. The gas phase flux j_1 can be approximated by assuming that the flux of oxygen from the bulk of the gas phase to the gas-oxide interface is proportional to the difference between the oxygen concentration in the bulk of the gas c_g and the oxygen concentration adjacent to the oxide surface c_s :

$$j_1 = h_g(c_g - c_s), \quad (6.3.1)$$

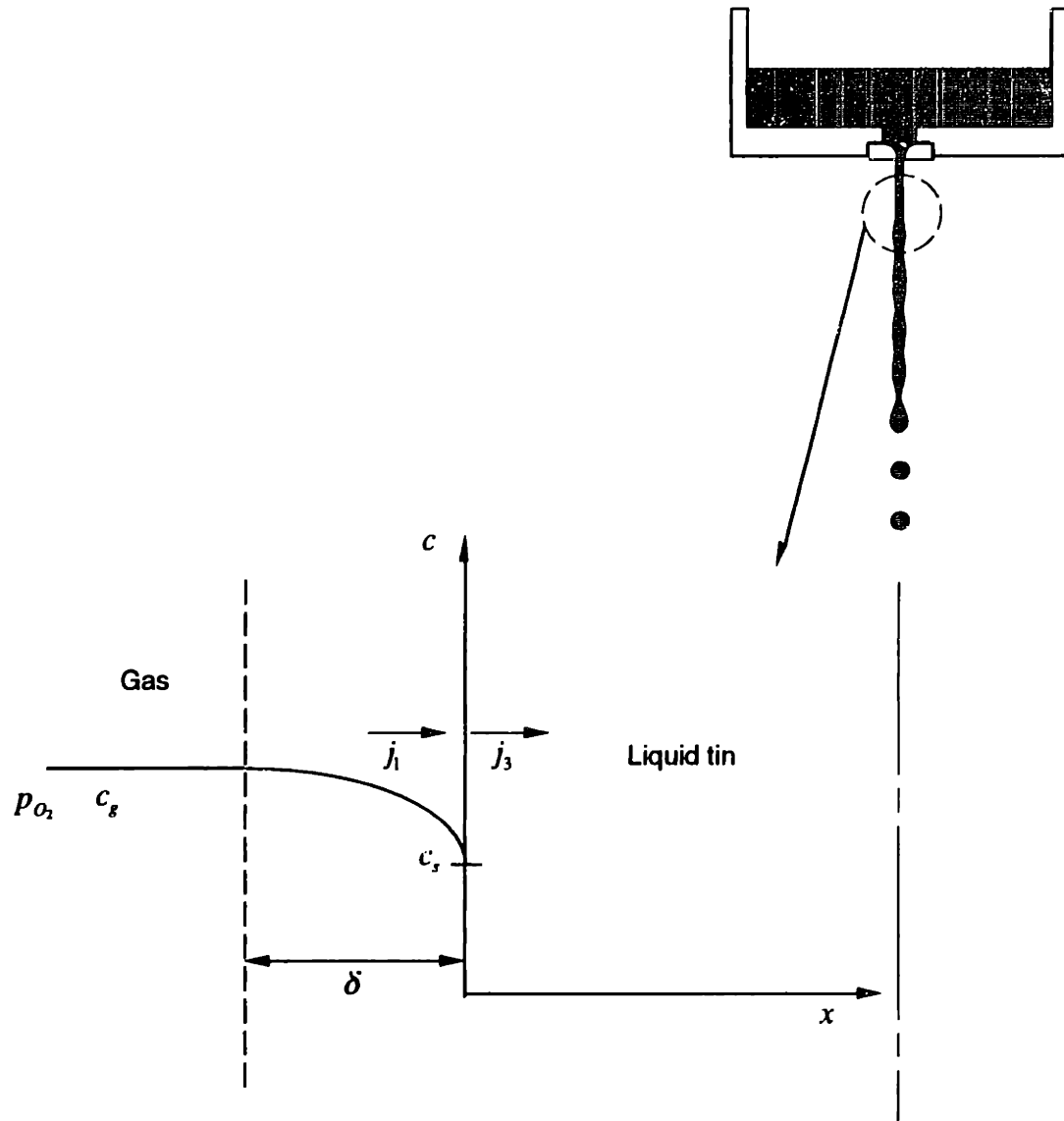


Figure 6.2 Schematic of oxygen transport in the absence of oxide layer.

where h_g is the gas-phase mass-transfer coefficient. The flux through the surface, j_3 , is assumed to be achieved through the reaction with the metal. Thus, it can be written as:

$$j_3 = k_s c_s, \quad (6.3.2)$$

where k_s is the reaction coefficient on the surface on molten metal. For steady state, i.e., $j_1 = j_3$, the following relation can be derived by combining equations (6.3.1) and (6.3.2):

$$c_s = \frac{c_g}{1 + \frac{k_s}{h_g}} \quad (6.3.3)$$

From equation (6.3.3), two limiting cases can be obtained. If $k_s \gg h_g$, i.e., mass transfer controlled case in the gas phase, $c_s \rightarrow 0$. If $k_s \ll h_g$, i.e., surface reaction controlled case, $c_s \rightarrow c_g$. Thus, for the number of oxygen molecules, N_1 , incorporated into a unit volume of the sub-surface region, the growth of the oxide layer can be written as:

$$N_1 \frac{d\xi}{dt} = j = \frac{k_s h_g}{k_s + h_g} c_g \quad (6.3.4)$$

Equation (6.3.4) can be re-written as:

$$\frac{d\xi}{dt} = \frac{k_s h_g}{k_s + h_g} \frac{1}{N_1} c_T \cdot X_{O_2} \quad (6.3.5)$$

where c_T is the total concentration of all molecules in the bulk, and X_{O_2} the molar fraction of oxygen molecules in the bulk. Equation (6.3.5) can be approximated for two limiting cases:

$$\frac{d\xi}{dt} \cong h_g \frac{c_T}{N_1} X_{O_2} \quad \text{for the mass controlled case } (k_s \gg h_g), \quad (6.3.5a)$$

and:

$$\frac{d\xi}{dt} \cong k_s \frac{c_T}{N_1} X_{O_2} \quad \text{for the surface reaction controlled case } (k_s \ll h_g). \quad (6.3.5b)$$

This model is over-simplified in that it does not consider reaction products, and the linear approximation that describes the surface reaction is valid only for low values of X_{O_2} . The actual case is more complicated since the temperature gradient present in the wall of the molten metal jet is steep, which may change gas properties. There also may be a depletion of oxygen molecules as the molten metal jet continues to exit from the nozzle and consumes them.

The detailed view of the surface of a metal jet in Figure 6.3 assumes that the metal oxide has grown to a certain thickness, although the oxide layer thickness is zero at the orifice. The following model discusses the kinetics of oxidation in which the oxide layer is already present on the surface of metal. This model is more involved since the transport of oxygen molecules through the oxide layer has to be considered. As shown in Figure 6.3,

the oxygen molecules are transported from the bulk of the gas phase to the gas-oxide interface with flux j_1 . The oxygen molecules are then transported across the existing oxide toward the tin with flux j_2 . The oxygen molecules react with tin at the tin oxide-tin interface with flux j_3 . Deal and Grove (1965) investigated the kinetics of the oxidation process by assuming that (i) the oxidizing species must be transported from the bulk of the gas to the oxide-gas interface, (ii) they as oxygen molecules must be transported across the oxide layer already present, and (iii) they must react with metal at the oxide-metal interface (Grove, 1967; Katz, 1988).

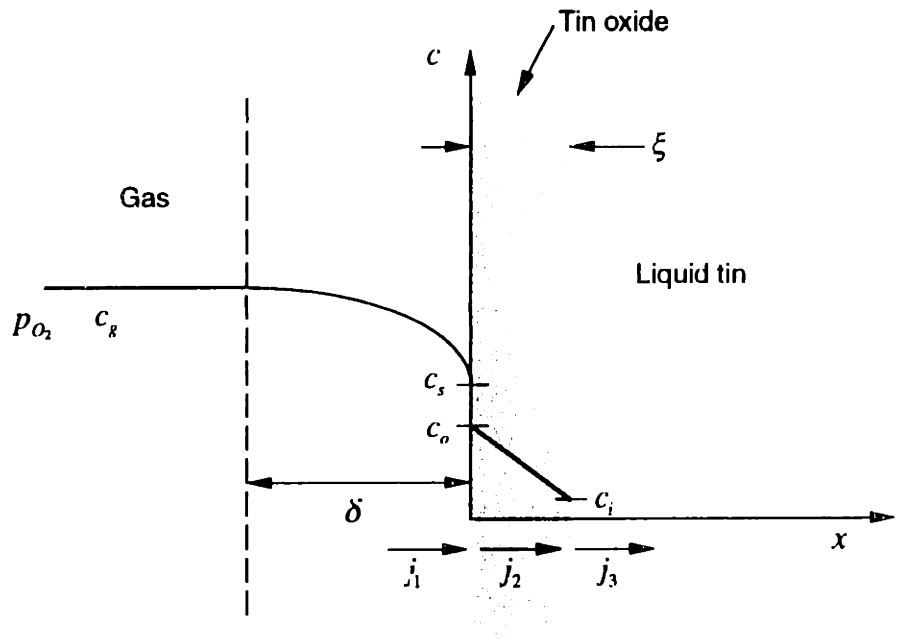


Figure 6.3 Schematic of transport of oxygen molecules.

For a quasi-steady state, $j_1 = j_2 = j_3$. The gas phase flux, j_1 , can be approximated by assuming that the flux of oxygen from the bulk of the gas phase to the gas-oxide interface is proportional to the difference between the oxygen concentration in the bulk of the gas c_g and the oxygen concentration adjacent to the oxide surface c_s :

$$j_1 = h_g(c_g - c_s), \quad (6.3.6)$$

where h_g is the gas-phase mass-transfer coefficient. To relate the equilibrium concentration of oxygen molecules in the oxide to that in the gas phase, it can be assumed that at equilibrium the concentration of a species within a solid is proportional to the partial

pressure of that species in the surrounding gas. Thus, it can be assumed that the equilibrium concentration in the oxide at the outer surface, c_o , is proportional to the partial pressure of the oxidant, P_s , immediately adjacent to the oxide surface, whose relationship can be written as follows:

$$c_o = HP_s, \quad (6.3.7)$$

where H is a constant. Furthermore, the equilibrium bulk concentration in the oxide, c^* , can be written as:

$$c^* = HP_g, \quad (6.3.8)$$

where P_g is the partial pressure in the bulk of the gas. Since $c_g = P_g/kT$ and $c_s = P_s/kT$ according to the ideal gas law, and using equations (6.3.7) and (6.3.8), equation (6.3.6) can be rewritten as:

$$j_1 = h(c^* - c_o), \quad (6.3.9)$$

where h is the gas-phase mass-transfer coefficient in terms of concentration in the solid given by:

$$h = \frac{h_g}{HkT}, \quad (6.3.10)$$

where k is the Boltzmann constant.

The flux of these oxidizing molecules across the oxide is taken into Fick's Law at any point in the oxide layer. Following the quasi-steady state assumption, the flux through the oxide is given by:

$$j_2 = \frac{D_{oxide}(c_o - c_i)}{\xi}, \quad (6.3.11)$$

where D_{oxide} is the diffusion coefficient of oxygen molecules in the oxide layer, c_i the oxidizing species concentration in the oxide adjacent to the tin oxide-tin interface, and ξ the oxide layer thickness. Assuming that the flux corresponding to the tin oxide-tin interface reaction is proportional to c_i , the flux through the interface becomes:

$$j_3 = k_3 c_i, \quad (6.3.12)$$

where k_s is the reaction constant at the metal oxide-metal interface. Due to the steady state assumption, $j_1 = j_2 = j_3$. Thus, the concentrations of oxygen molecules at the gas-oxide interface and the metal oxide-metal interface can be obtained as:

$$c_i = \frac{1}{1 + \frac{k_s}{h} + \frac{k_s \xi}{D_{oxide}}} c^* \quad (6.3.13)$$

$$c_o = \frac{1 + \frac{k_s \xi}{D_{oxide}}}{1 + \frac{k_s}{h} + \frac{k_s \xi}{D_{oxide}}} c^* \quad (6.3.14)$$

Equations (6.3.13) and (6.3.14) can be examined for two limiting cases. If the diffusion coefficient is very small, i.e. the diffusion-controlled case, $c_i \rightarrow 0$ and $c_o \rightarrow c^*$. On the other hand, if the diffusion coefficient is very large, i.e., the reaction controlled case, $c_o = c_i$ and is given by:

$$c_o = c_i = \frac{c^*}{1 + \frac{k_s}{h}} \quad (6.3.15)$$

Figure 6.4 shows the distributions of the concentration of the oxidizing species in the oxide layer for these two limiting cases.

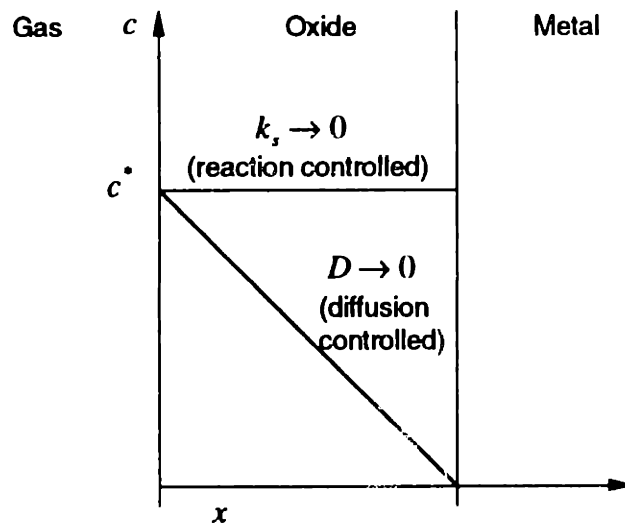


Figure 6.4 Distribution of the oxidizing species in the oxide layer for the two limiting cases of oxidation.

If N_1 is the number of oxidant molecules incorporated into a unit volume of oxide layer, the rate of growth of the oxide layer can be described by the following differential equation:

$$N_1 \frac{d\xi}{dt} = j = \frac{k_s}{1 + \frac{k_s}{h} + \frac{k_s x}{D_{oxide}}} c^* , \quad (6.3.16)$$

For dry oxygen, there are 2.2×10^{22} SnO_2 molecules/ cm^3 . Equation (6.3.16) can be solved with the initial condition, $\xi(t=0) = \xi_o$. This general initial condition allows the consideration of two or more successive oxidation steps. The quantity ξ_o can also be regarded as the thickness of oxide that is present at the end of an initial period of oxidation during which the assumptions involved in this oxidation model may not have been valid. Nevertheless, the solution of the differential equation (6.3.16) can be written as follows (Grove and Deal, 1965; Grove, 1967; Katz, 1988):

$$\xi^2 + A\xi = B(t + \tau) , \quad (6.3.17)$$

where:

$$A = 2D_{oxide} \left(\frac{1}{k_s} + \frac{1}{h} \right) \quad (6.3.17a)$$

$$B = \frac{2D_{oxide}c^*}{N_1} , \quad (6.3.17b)$$

and:

$$\tau = \frac{\xi_o^2 + A\xi_o}{B} . \quad (6.3.17c)$$

Equations (6.3.17a, b, c) can be solved for the oxide thickness as a function of time, resulting in the following relationship:

$$\xi = \frac{A}{2} \left(1 + \frac{t + \tau}{A^2/4B} \right)^{1/2} - 1 \quad (6.3.18)$$

For long time scales, i.e., $t \gg A^2/4B$ and also $t \gg \tau$, the following relationship can be found:

$$\xi \equiv \frac{A}{2} \left(\frac{t}{A^2/4B} \right)^{1/2}, \quad (6.3.19)$$

or:

$$\xi^2 \equiv Bt. \quad (6.3.19a)$$

Thus, for a relatively long time scale, the general relation, equation (6.3.18), reduces to equation (6.3.19a), which is the well-known parabolic oxidation law with B as the parabolic rate constant. For a short time scale, i.e., $(t + \tau) \ll A^2/4B$, the following relation can be obtained:

$$x \equiv \frac{A}{2} \cdot \frac{1}{2} \left(\frac{t + \tau}{A^2/4B} \right), \quad (6.3.20)$$

or:

$$x \equiv \frac{B}{A} (t + \tau) \quad (6.3.20a)$$

Thus, for short time scales, the linear rate law is obtained as shown in equation (6.3.20), where the linear constant can be written as:

$$\frac{B}{A} = \frac{k_p h}{k_p + h} \frac{c^*}{N_1} \quad (6.3.21)$$

Coefficients A and B for silicon oxidation have been obtained experimentally by many researchers (Grove and Deal, 1965; Grove, 1967; Katz, 1988); however, there are no such data for tin oxidation. The time scale for investigation on silicon oxidation was in the range of hours, making it difficult to apply directly to tin oxidation in the time scale of milliseconds, the typical time for uniform droplet break-up in the UDS process.

6.4 Gas Phase Mass Transfer

In the previous section, two limiting cases for oxidation were discussed. In this section, mass transfer in the gas phase to the surface of molten metal jets will be discussed. Simple calculations will be done to calculate the oxide layer thickness assuming that all oxygen molecules within the boundary layer are converted into the metal oxide.

6.4.1 Gas phase mass transfer using stagnant film theory

Figure 6.5 shows the stagnant film theory to calculate the flux of oxygen molecules in the gas phase. Assuming that the flux is driven by the concentration differences in the bulk phase and on the surface of metal, the flux in the gas phase, j , can be written as:

$$j = D_g \frac{c_g - c_s}{\delta}, \quad (6.4.1)$$

where D_g is the diffusion coefficient in the gas phase, c_g , the concentration of oxygen molecules in the bulk, c_s , the concentration of oxygen molecules on the surface and δ the diffusion length. The coefficient of mass transfer, h_g , is thus defined as:

$$h_g = \frac{D_g}{\delta}. \quad (6.4.2)$$

Equations (6.4.1) and (6.4.2) can be combined, resulting in:

$$j = h_g (c_g - c_s) \quad (6.4.3)$$

However, the coefficient of mass transfer needs to be determined experimentally, which makes the stagnant film theory impractical.

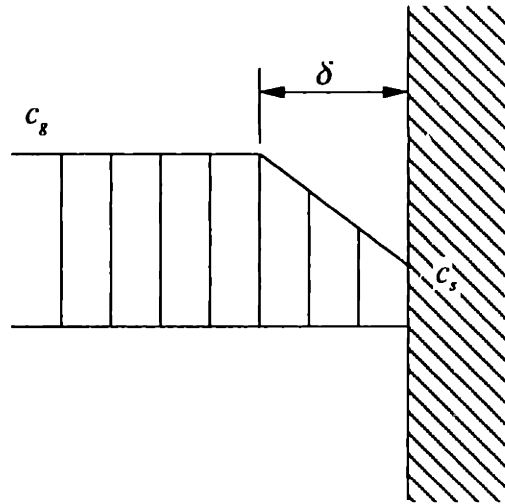


Figure 6.5 Gas phase mass transfer in stagnant film theory.

6.4.2 Gas phase mass transfer using boundary layer theory

Figure 6.6 schematically shows gas flowing over a flat surface at the velocity of U . The boundary layer line is drawn where the local velocity is about $0.99U$. The friction, F_{fric} , on the wall per unit area due to the viscous flow in the boundary layer is given by:

$$F_{fric} = \mu \frac{\partial u}{\partial y}, \quad (6.4.4)$$

where μ is the gas viscosity. The inertia force of elemental mass, $F_{inertia}$, in the boundary layer can be written as:

$$F_{inertia} = m_g a_x = m_g \frac{du}{dt} \quad (6.4.5)$$

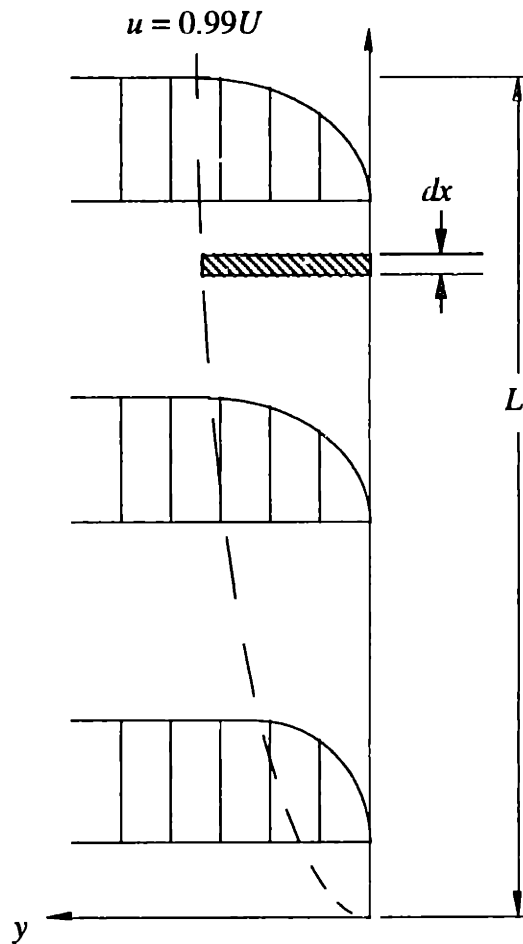


Figure 6.6 Gas phase mass transfer using boundary layer theory.

The velocity change with respect to time can approximately be transformed to:

$$\frac{du}{dt} = \frac{du}{dx} \frac{dx}{dt} = \frac{du}{dx} u . \quad (6.4.6)$$

The mass of element per unit area in the boundary can be represented by:

$$m_g = \rho_g \delta(x). \quad (6.4.7)$$

Substituting equations (6.4.6) and (6.4.7) into equation (6.4.5) results in:

$$F_{inertia} = \rho_g \delta(x) u \frac{du}{dx} \quad (6.4.8)$$

Thus, the boundary layer thickness (or diffusion length) as a function of x can be derived by combining equations (6.4.4) and (6.4.8):

$$\mu \frac{\partial u}{\partial y} = \rho_g \delta(x) u \frac{du}{dx} \quad (6.4.9)$$

The above equation can be approximated as:

$$\mu \frac{U}{\delta(x)} \approx \rho_g \delta(x) U \frac{U}{x} , \quad (6.4.9a)$$

which can be simplified to:

$$\delta(x) = \sqrt{\frac{\mu x}{\rho_g U}} . \quad (6.4.9b)$$

Thus, the average diffusion length can be obtained by integration over a distance of L :

$$\bar{\delta} = \frac{1}{L} \int_0^L \delta(x) dx = \frac{1}{L} \int_0^L \sqrt{\frac{\mu x}{\rho_g U}} dx = \frac{2}{3} L \sqrt{\frac{\mu}{\rho_g U L}} = \frac{2}{3} \frac{L}{\sqrt{Re}} , \quad (6.4.10)$$

where

$$Re = \frac{\rho_g U L}{\mu} = \frac{U L}{\nu} .$$

Since $h_g = D/\bar{\delta}$, the coefficient of mass transfer in the gas phase can be found using equation (6.4.10):

$$h_g = \frac{3D}{2L} \sqrt{\text{Re}} \quad (6.4.11)$$

Assuming that the diffusion coefficient of oxygen molecules in the gas phase, D , is similar to the kinetic viscosity of gas, ν , (of the order of $1.7 \times 10^{-5} \text{ m}^2/\text{s}$ for air at 298 K), and the bulk velocity is 5 m/s, the length L should be 0.015 m. (Justifications for these parameters will be discussed in detail in Chapter 7.) Thus, the coefficient of mass transfer in the gas phase becomes 0.113 m/s.

Using equation (6.4.10) and the above parameters, the average boundary layer thickness (or diffusion length) is found to be about 150 μm .

6.4.3 Diffusion length in the gas phase using the kinematic viscosity of gas

The boundary layer thickness, δ , can be calculated using the following equation:

$$\delta = \sqrt{D_g t} \quad (6.4.12)$$

where D_g is the diffusion coefficient in the gas phase and t the time. It will be assumed that the diffusion coefficient is roughly equal to the kinematic viscosity of air at 298 K ($= 1.7 \times 10^{-5} \text{ m}^2/\text{s}$). It will be further assumed that the diffusion time is about 3 ms. Thus, the diffusion length scale in the gas phase is about 225 μm , which is about twice the size of the jet diameter than the one obtained by the boundary layer theory. In the next section, the diffusion length in the gas phase using the boundary layer theory will be discussed.

6.4.4 Estimation of tin oxide layer thickness using the diffusion length in the gas phase

To calculate the thickness of the oxide layer from the diffusion length in the gas phase, it may be assumed that every oxygen molecule in the diffusion layer is consumed to form a metal oxide layer on the surface of a molten metal jet. Let the diameter of the jet be d_j , and the thickness of diffusion length in the gas phase be δ_{diff} , as shown in Figure 6.7. The volume of gas in the diffusion layer, V_{gas} , can be estimated as:

$$V_{gas} = \pi \left[\left(\delta_{diff} + \frac{d_j}{2} \right)^2 - \left(\frac{d_j}{2} \right)^2 \right] L_{diff} \quad (6.4.13)$$

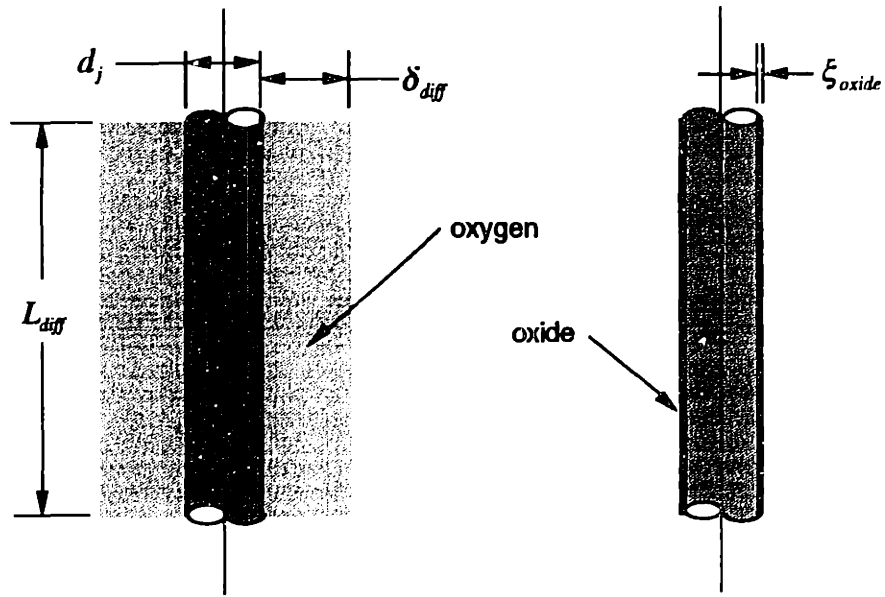


Figure 6.7 Schematic of conversion of oxygen molecules in the boundary layer to metal oxide.

or:

$$V_{gas} = \pi \delta_{diff} (\delta_{diff} + d_j) L_{diff} . \quad (6.4.14)$$

The number of gas molecules, n_{gas} , in this confined volume can be obtained using the ideal gas law:

$$n_{gas} = \frac{PV_{gas}}{RT} \quad (6.4.15)$$

Knowing the mole fraction of oxygen, X_{O_2} , the number of oxygen molecules can be obtained by:

$$n_{oxygen} = n_{gas} X_{O_2} . \quad (6.4.16)$$

The weight of oxygen in the gas phase can also be obtained by:

$$m_{oxygen} = n_{oxygen} M_{oxygen} , \quad (6.4.17)$$

where M_{oxygen} is the molecular weight of oxygen. Combining equations (6.4.14) through (6.4.17) results in:

$$m_{\text{oxygen}} = X_{\text{O}_2} M_{\text{oxygen}} \frac{P}{RT} \pi \delta_{\text{diff}} (\delta_{\text{diff}} + d_j) L_{\text{diff}} \quad (6.4.18)$$

Because the thickness of the oxide layer is very thin compared with the jet diameter, the volume of oxide scale on the jet surface can be estimated as:

$$V_{\text{oxide}} = \pi d_j L_{\text{diff}} \xi_{\text{oxide}} \quad (6.4.19)$$

The weight of the oxide is:

$$m_{\text{oxide}} = \rho_{\text{oxide}} V_{\text{oxide}} \quad (6.4.20)$$

The mass of oxygen molecules in the oxide can be obtained as:

$$m_{\text{oxygen}} = m_{\text{oxide}} \left(\frac{M_{\text{oxygen}}}{M_{\text{oxide}}} \right) \quad (6.4.21)$$

Substituting equations (6.4.19) and (6.4.20) into equation (6.4.21) results in the weight of oxygen molecules in the oxide scale and is as follows:

$$m_{\text{oxygen}} = \pi d_j L_{\text{diff}} \rho_{\text{oxide}} \xi_{\text{oxide}} \left(\frac{M_{\text{oxygen}}}{M_{\text{oxide}}} \right) \quad (6.4.22)$$

By combining equations (6.4.18) and (6.4.22), the thickness of the oxide layer formed as a result of the conversion of oxygen molecules to the oxide scale is:

$$\xi_{\text{oxide}} = X_{\text{O}_2} \frac{P}{RT} \delta_{\text{diff}} \left(1 + \frac{\delta_{\text{diff}}}{d_j} \right) \frac{M_{\text{oxide}}}{\rho_{\text{oxide}}} \quad (6.4.23)$$

Equation (6.4.23) assumes that the reaction between the pure metal and the oxygen diffusion coefficient in the oxide scale is very fast. Thus, if the oxidation is limited by the supply of oxygen molecules in the gas phase, equation (6.4.23) can be used to obtain the oxide layer thickness for various oxygen concentrations. Table 6.1 shows the thickness of the oxide layer assuming that every oxygen molecule in the diffusion boundary layer is converted into the oxide scale.

The ionic radius of chemical elements is typically in the range of 0.1 nm. However, the oxide layer calculated using 5 ppm is less than the ionic radius. The calculated oxide layer thickness for 200,000 ppm is about 0.2 μm . From this preliminary calculation, it seems that the estimation using the boundary layer thickness underestimates

the oxide layer thickness for low oxygen concentration levels and overestimates for high oxygen concentration levels.

Table 6.1 The thickness of tin oxide layer with respect to the oxygen content in the spray chamber. The pressure of spray chamber is assumed to be 135 kPa (5 psig), temperature 298 K, molecular weight of stannic oxide, SnO_2 , 150.7 kg/kmol, and density of SnO_2 7000 kg/m³. The jet diameter is assumed to be 100 μm .

Oxygen content (ppm)	Oxide layer thickness (nm), if $\delta=150 \mu\text{m}^*$	Oxide layer thickness (nm), if $\delta=225 \mu\text{m}^{**}$
5	0.0032	0.0043
250	0.16	0.21
500	0.32	0.43
750	0.47	0.64
1,000	0.63	0.85
1,250	0.80	1.07
1,500	0.95	1.28
1,750	1.10	1.50
2,000	1.26	1.71
200,000	126.00	171.00

* Using the diffusion boundary layer thickness

** Using the kinematic viscosity of gas as diffusion coefficient

6.5 Possible Oxidation Mechanisms and Oxide Layer Thickness

As shown in equation (6.2.6), the formation of metal oxide as a chemical reaction appears to be a simple reaction; this is not actually the case. The reaction product frequently appears as a compact phase with the reacting substances spatially separated from each other. Further reaction is then possible only if at least one of the reactants diffuses through the scaling layer to the other reactant. In such cases, the course of the reaction is determined no longer by the overall chemical process described in equation (6.2.6), but by diffusion processes and phase-boundary reactions. Hauffe (1965) lists following possible processes. One of these processes is the slowest and therefore the rate-determining, or rate-controlling, step (Hauffe, 1965):

1. Phase-boundary reactions (of the nonmetal molecules with simultaneous electron exchange and splitting of the molecules at the gas/oxide interface and transfer of the metal from the metallic phase, in the form of ions and electrons, to the scale at the metal/oxide interface with further reaction of the individual

reactants and formation of the reaction products), nucleation, and crystal growth.

2. Diffusion transport of cations, anions, and electrons through the scale complicated by a special migration mechanism because of chemical and electrical potential gradients in the scaling or tarnishing layer.
3. Predominant transport processes in space-charge boundary layers in the case of thin tarnishing layers, especially at low temperatures.

He further lists the following factors that are significant for the formation, composition, and structure of the scaling layer:

4. The thermodynamic stability of the oxide formed.
5. The crystal structures of the scaling layer and of the metal or the alloy, which determine the adhesion between the scaling layer and the underlying metals.

The oxidation of metals and alloys may take various laws such as linear, parabolic, cubic, or logarithmic as follows:

$$\Delta m = k_l t, \quad (6.5.1)$$

$$(\Delta m)^2 = k_p t, \quad (6.5.2)$$

$$(\Delta m)^3 = k_c t, \quad (6.5.3)$$

or:

$$\Delta m = k_r \log(1 + at), \quad (6.5.4)$$

where Δm is the mass gain per unit area of scale, t is the oxidation time, and a is a constant. k_l , k_p , k_c , and k_r are the reaction constants for the linear, parabolic, cubic, and logarithmic rate laws, respectively, which generally vary with temperature in the Arrhenius form:

$$k \sim A_a \exp\left(-\frac{E_a}{RT}\right), \quad (6.5.5)$$

where A_a is a constant associated with the diffusion coefficient and the partial pressure of oxygen and E_a is the activation energy. As the partial pressure of oxygen increases, the constant A_a increases, thus, Δm increases as well.

Typically, the linear rate law is observed when the diffusion and the transport process are sufficiently rapid. At high temperatures and high gas pressures, oxidation follows a parabolic rate. At intermediate temperatures, a cubic rate law of oxidation is often observed. At low temperatures, the oxidation follows a logarithmic rate law, and thin to very thin layer frequently forms. After attaining a critical thickness, the thin layer practically stops growing; the growth of oxide is asymptotic (Hauffe, 1965).

The weight increase, Δm , can be written as (Schmalzreid, 1974):

$$\Delta m = \Delta \xi \rho_{oxide} \frac{M_{oxygen}}{M_{oxide}}, \quad (6.5.6)$$

where $\Delta \xi$ is the growth of the oxide layer as a result of oxidation, ρ_{oxide} the density of oxide, M_{oxygen} the molecular weight of oxygen, and M_{oxide} the molecular weight of the oxide. M_{oxygen} and M_{oxide} for SnO_2 are 32 kg/kmol and 150.7 kg/kmol, respectively. The above equation can be rewritten as:

$$\Delta \xi = \frac{\Delta m}{\rho_{oxide}} \frac{M_{oxide}}{M_{oxygen}}, \quad (6.5.7)$$

which can be written in terms of the molar volume of the metal oxide as (Kubaschewski and Hopkins, 1962):

$$\Delta \xi = \Delta m \frac{\bar{V}_{oxide}}{M_{oxygen}}, \quad (6.5.8)$$

where \bar{V}_{oxide} is the molar volume of metal oxide. The molar volumes of selected metals are listed in Table 6.2. If the parabolic reaction is considered, equation (6.5.2) can be converted to the following form:

$$(\Delta \xi)^2 = k'_p t$$

where $k'_p = k_p \left(\frac{\bar{V}_{oxide}}{M_{oxygen}} \right)^2$.

Table 6.2 Structures and atomic volumes of selected materials*

Metal	Melting point (K)	Boiling point (K)	Molar volume, solid (cm ³)	Molar volume, liquid (cm ³)
Al	933	2773	10.00	11.27
Cu	1356	2843	7.1	7.95
In	430	2348	15.65	15.75
Pb	599.7	2013	18.2	19.5
Sn	504.9	3023	16.25	17.05
Zn	692.5	1180	9.1	9.85

* Adapted from Kubaschewski and Hopkins (1962)

Kubaschewski and Hopkins (1962) found that pure tin follows a parabolic oxidation rate law. They give the parabolic oxidation rate constant for pure tin for the temperature ranges 598 to 723 K as:

$$k'_p = 4.97 \times 10^{-10} \exp\left(-\frac{80000}{RT}\right) \frac{\text{m}^2}{\text{s}}. \quad (6.5.9)$$

At 553 K, the parabolic reaction constant is $1.38 \times 10^{-17} \text{ m}^2/\text{s}$. Thus, the oxide growth in 3 ms of oxidation time is expected to be 0.2 nm.

Miller and Bowles (1990) looked at the oxidation of 63Sn/37Pb at typical soldering temperatures. They also found that the oxidation follows a parabolic form. While they did not give their results in the form of reaction constants, their experimental results can be interpreted to yield the reaction constants of 5.0×10^{-15} and $1.6 \times 10^{-15} \text{ m}^2/\text{s}$ at 523 K and 477 K, respectively. (The melting point of eutectic solder is 456 K.) Typically, oxidation is faster in the pure metal than in the alloy. Although the above listed reaction constants do not give accurate results to calculate the oxide layer thickness of pure tin, they may be used to obtain a rough estimate for comparison to the experimental results from the UDS processes. If the oxidation time is assumed to be 3 ms, the thicknesses of the oxide layer are 0.07 and 0.06 nm, respectively. The extrapolation of the relationship does not give a meaningful answer since the calculated values are smaller than the ionic diameter of tin, which is about 0.14 nm.

6.6 Property Changes as a Result of Oxidation

It has been shown in Chapter 2 that liquid metal properties such as density, surface tension, and viscosity affect jet break-up length. Because it is not possible to measure these properties of liquid tin directly at the time of the break-up, the following hypothesis on how surface properties change as a result of oxidation is made. As shown in Figure 6.8, three possible morphologies are presented.

In mechanism I, particles of oxide form in the sub-surface region of the liquid jet, which behaves like a dilute suspension. In this case, the material properties should be similar to those of pure liquid tin. The jet should break into a train of uniform droplets; this mechanism may be ruled out as a possible cause for the jet to stabilize.

When there are two phases in a liquid state as shown in Figure 6.9, the following linear relationships can be used to calculate the density and surface tension:

$$\rho_c = \phi_1 \rho_1 + \phi_2 \rho_2$$

$$\sigma_c = A_1 \sigma_1 + A_2 \sigma_2 ,$$

and:

$$\mu_c = \mu_o \left(1 + \frac{\phi}{\phi_m} \right)^n ,$$

where ρ is the density, ϕ the volume fraction, σ the surface tension, A the area fractions, μ_o the bulk viscosity of liquid, ϕ_m the maximum volume fraction, and n an empirical constant. It should be noted that this is only a linear approximation. In most cases, the relationship is not linear.

In mechanism II, the oxygen reacts with the metal, thereby forming an oxide layer on the surface, while the surface remains as mushy solid-liquid or as a liquid with solid oxide floating on the surface. In this case, the density should more or less remain the same as that of pure liquid tin. The surface tension may decrease as a result of oxide on the surface, while the viscosity may increase. Thus, the combination of the increase of viscosity and the decrease of surface tension may be sufficient to retard the break-up process and eventually to form fibers instead of droplets. However, by increasing the amplitude of perturbation on the jet surface, the molten tin jet can be broken into a train of uniform droplets.

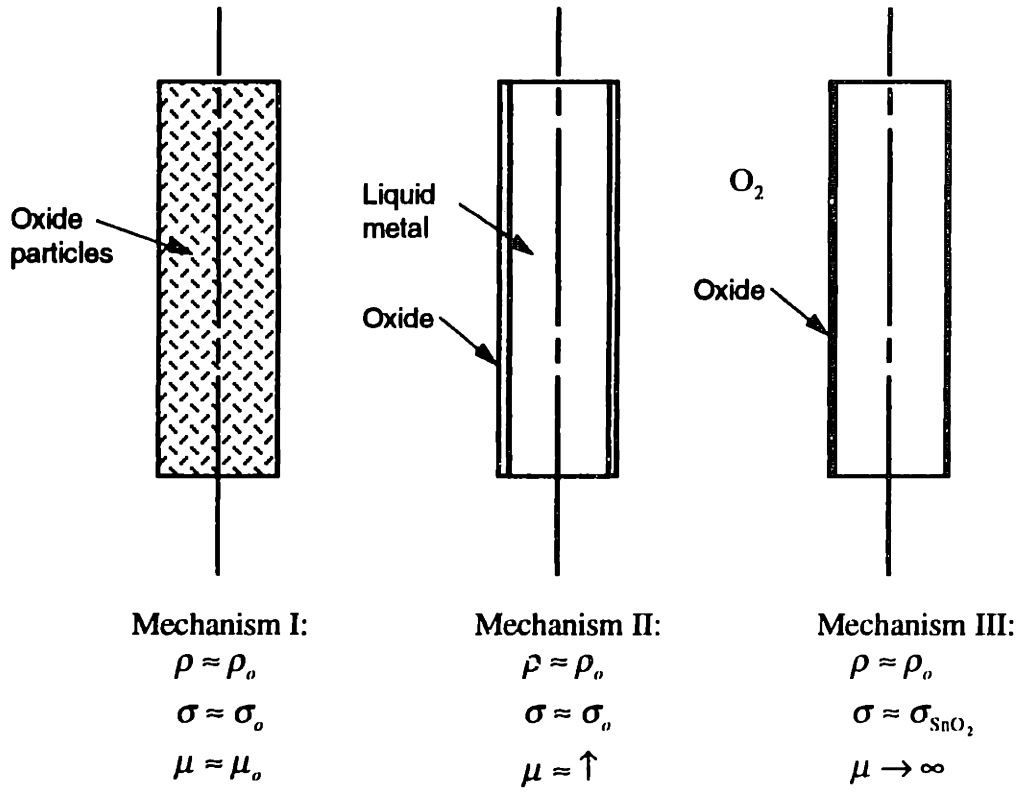


Figure 6.8 Possible mechanisms of surface oxidation and the resulting changes in material properties.

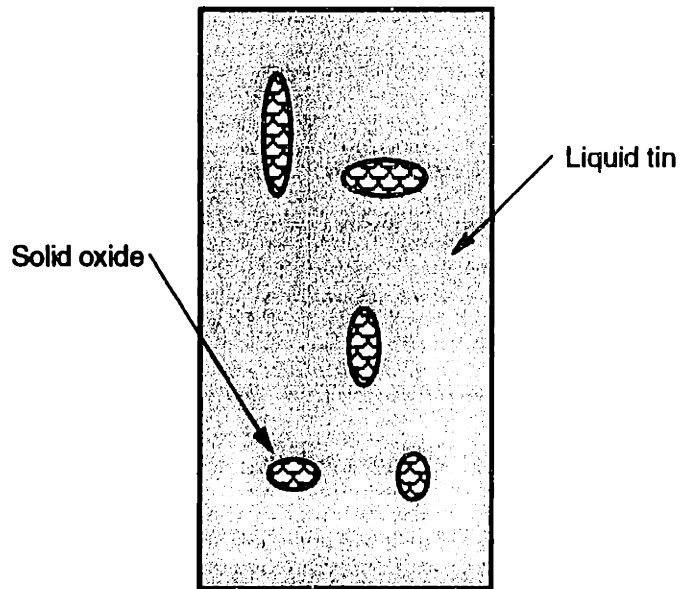


Figure 6.9 Solid oxide particles in liquid tin.

In mechanism III, the reaction between oxygen and metal forms an oxide layer on the jet surface. The oxide layer on the surface becomes solid since the melting temperature of metal oxide is higher than that of pure metal. The melting points of stannic (SnO_2) and stannous (SnO) oxides are 1898 and 1315 K whereas the melting point of tin is 505 K (Shackelford and Alexander, 1992). The density of the jet should not change significantly since the thickness of the oxide layer is very small in comparison to the diameter of the tin jet. If the jet surface becomes solid, it should be very difficult for the jet to break into a train of uniform droplets due to the action of surface tension of a solid layer of oxide. The viscosity of a solid oxide layer becomes so high that the jet should be stabilized. For example, as seen in Chapter 2, the jet break-up length of a 100 μm glycerin jet is 432 mm, whereas that of tin jet is about 7 mm. By the time the tin jet travels 432 mm, the jet should have solidified completely. Thus, the jet remains stable to form fibers when a solid layer is formed on the surface of molten tin.

It can be assumed, however, that the force (or pressure) caused by the action of the liquid surface tension on the surface of the molten tin jet may allow the jet to break into a train of droplets. The contribution of the force due to the liquid surface tension on the break-up of tin covered with a solid layer is presented in section 7.2.6 of Chapter 7.

6.7 Conclusions

This chapter briefly discussed theories of oxidation. The thermodynamics of equilibrium analysis clearly showed that oxidation took place under typical UDS operating conditions. The oxidation reaction on the surface of molten metal tin was discussed. It is apparent that there is insufficient data to determine whether the oxidation of the molten tin jet is controlled by the transport of oxygen molecules to the surface of molten tin (i.e., mass transfer in the gas phase controlled), or by the transport of oxygen molecules through the oxide layer (i.e., diffusion controlled), or by the transport of oxygen molecules across the oxide-metal interface (i.e., reaction controlled).

The diffusion length in the gas phase was calculated by the boundary layer theory. Calculations were carried out to estimate the oxide layer thickness assuming all oxygen molecules in the diffusion boundary layer were converted into the tin-oxide. The results seem to underestimate for low oxygen concentrations and overestimate for high oxygen concentrations.

The break-up time of the molten tin jets with a diameter of 100 μm is on the order of milliseconds. However, many oxidation studies were for the time scale of hours, days,

months, and, in some cases, years. Thus, there is doubt whether the conventional oxidation rate laws for tin can accurately predict the oxide layer thickness for the short time scale as discussed in section 6.5.1. Section 6.6 discussed possible material property changes, which affect the break-up behavior of continuous laminar jets, as a result of surface oxidation.

The literature review revealed that an oxidation study of molten metal tin at the time of break-up is needed. As will be discussed in Chapter 7, it is necessary to eliminate the further oxidation of molten tin droplets after the break-up by quenching the droplets and shielding them from the environment. The thickness of the oxide layer on the surface of tin droplets then can be measured and used to investigate how the oxide formation on the surface affects the break-up behavior of molten metal tin.

Nomenclature

<i>a</i>	stoichiometric constant of a reactant
a_x	acceleration in the <i>x</i> -direction
<i>a</i>	constant used in the logarithmic rate law of oxidation
<i>A</i>	constant defined as $2D_{oxide} \left(\frac{1}{k_s} + \frac{1}{h} \right)$
A_1	area fractions
A_2	area fractions
A_a	constant for an Arrhenius equation
<i>A</i>	a reactant species
<i>b</i>	stoichiometric constant of a reactant
<i>B</i>	constant defined as $\frac{2D_{oxide}c^*}{N_1}$
<i>B</i>	a reactant species
<i>c</i>	stoichiometric constant a product
c_g	oxygen concentration in the bulk of the gas
c_i	oxidizing species concentration in the oxide adjacent to metal oxide interface
c_o	equilibrium concentration in the oxide at the outer surface
c_s	oxygen concentration adjacent to the surface of metal
c_T	concentration of all molecules in the bulk
c^*	equilibrium bulk concentration in the oxide
<i>C</i>	a product species

d	stoichiometric constant of a product
d_j	jet diameter
D_g	diffusion coefficient in the gas phase
D_{oxide}	diffusion coefficient of oxygen molecules in the oxide layer
D_{Sn}	diffusion coefficient of oxygen molecules in the pure liquid tin
D	a product species
E_a	activation energy
F_{fric}	friction force on the wall per unit width
$F_{inertia}$	inertia force of elemental mass in the boundary layer
G	Gibbs free energy
ΔG°	Gibbs free energy change at standard state
h	gas-phase mass-transfer coefficient in the solid phase, $\frac{h_g}{HkT}$
h_g	mass transfer coefficient in the gas phase
H	a constant
j_1	oxygen molecule flux in the gas phase
j_2	oxygen molecule flux in the metal oxide phase
j_3	oxygen molecule flux at the metal surface of at the metal-metal oxide interface
k	reaction constant
k_s	reaction constant at the metal surface or at the metal-metal oxide interface
k_c	reaction constant for cubic rate law of oxidation
k_e	reaction constant for logarithmic rate law of oxidation
k_l	reaction constant for linear rate law of oxidation
k_p	reaction constant for parabolic rate law of oxidation
k'_p	reaction constant for parabolic rate law of oxidation, $k_p \left(\frac{\bar{V}_{oxide}}{M_{oxygen}} \right)^2 \left[\frac{\Gamma_d^2}{s} \right]$
K	equilibrium constant
L	distance along the x -direction
L_{diff}	diffusion length along the x -direction
m_g	mass of an element in boundary layer
m_{oxide}	mass of metal oxide
m_{oxygen}	mass of oxygen
Δm	mass gain per unit area of scale due to oxidation
M_{oxide}	molecular weight of metal oxide
M_{oxygen}	molecular weight of oxygen
n	constant

n_{gas}	number of gas molecules
n_{oxygen}	number of oxygen molecules
N_1	number of oxygen molecules incorporated into a unit volume of the surface
P	pressure
P_g	partial pressure in the bulk of the gas
P_{O_2}	partial pressure of oxygen
P_s	partial pressure of oxidant immediately adjacent to the oxide surface
R	universal gas constant, $1.987 \frac{\text{cal}}{\text{K} \cdot \text{mol}}$ or $8.3143 \frac{\text{J}}{\text{K} \cdot \text{mol}}$
Re	Reynolds number, $\frac{\rho_s UL}{\mu}$
t	time
T	temperature
u	local velocity
U	velocity
V_{gas}	volume of gas in the diffusion length layer
V_{oxide}	volume of metal oxide on the surface of molten metal jet
\bar{V}_{oxide}	molar volume of metal oxide
x	x-axis
X	molar fraction
X_{O_2}	molar fraction of oxygen
y	y-axis
δ	boundary layer thickness or diffusion length
$\bar{\delta}$	average boundary layer thickness or diffusion length
δ_{diff}	diffusion length
μ	viscosity
μ_g	gas viscosity
μ_o	bulk viscosity of liquid
ν	kinematic viscosity of gas
ξ_{oxide}	oxide layer thickness
ξ_o	initial oxide layer thickness
ρ	density
ρ_g	gas density
ρ_{oxide}	density of metal oxide
σ	surface tension

τ constant defined as $\frac{\xi_o^2 + A\xi_o}{B}$

ϕ volume fraction

ϕ_m maximum volume fraction

Chapter 7 EFFECTS OF OXIDATION ON JET BREAK-UP BEHAVIOR: EXPERIMENTAL

This chapter will establish the criteria under which a jet breaks into a train of uniform droplets. As discussed earlier, when there are sufficient oxygen molecules in the spray chamber, the jet forms a fiber instead. Chapter 6 analyzed the theoretical aspects of the role of surface oxidation on break-up behavior. This chapter briefly describes the experimental apparatus and procedures. The results of the break-up length of jets and the thickness of the oxide layer with respect to various oxygen levels in the spray chamber will be presented and discussed. As discussed in Chapter 6, the activity of oxidation increases with the increase of oxygen molecules, i.e., the partial pressure of oxygen, which leads to the increase of oxide layer thickness. Thus, from the outset, it is assumed that the jet does not break into a train of droplets because the oxide layer builds up to a certain critical thickness.

7.1 Experimental Apparatus and Procedure

7.1.1 Experimental apparatus for the investigation of jet break-up

The experimental apparatus was modified to investigate the effects of oxidation in the break-up of molten tin jets as shown in Figure 7.1. Rotameters (OMEGA, Model No. FL3405ST) and an oxygen analyzer (Illinois Instruments, Model No. 2550) were added. A tank of nitrogen containing 2000 ppm oxygen was connected to the spray chamber through the rotameters to vary the flow rate of nitrogen. The oxygen analyzer measured the oxygen content in the spray chamber by sampling the gases.

The oxygen analyzer was neither flow sensitive nor pressure sensitive. The manufacturer, however, recommended that the input gauge pressure be less than 1 MPa (145 psig) or more than 10 kPa (0.1 psig). If the input gauge pressure is less than 10 kPa, installation of a small pump is recommended. Since the spray chamber was filled to the gauge pressure of 35 kPa (5 psig) in the typical experimental conditions, a pump was unnecessary. The recommended range of temperatures of sample gases was from 268 to 308 K (-5 to 35 C). Since the sample gas was at room temperature, it was not cooled.

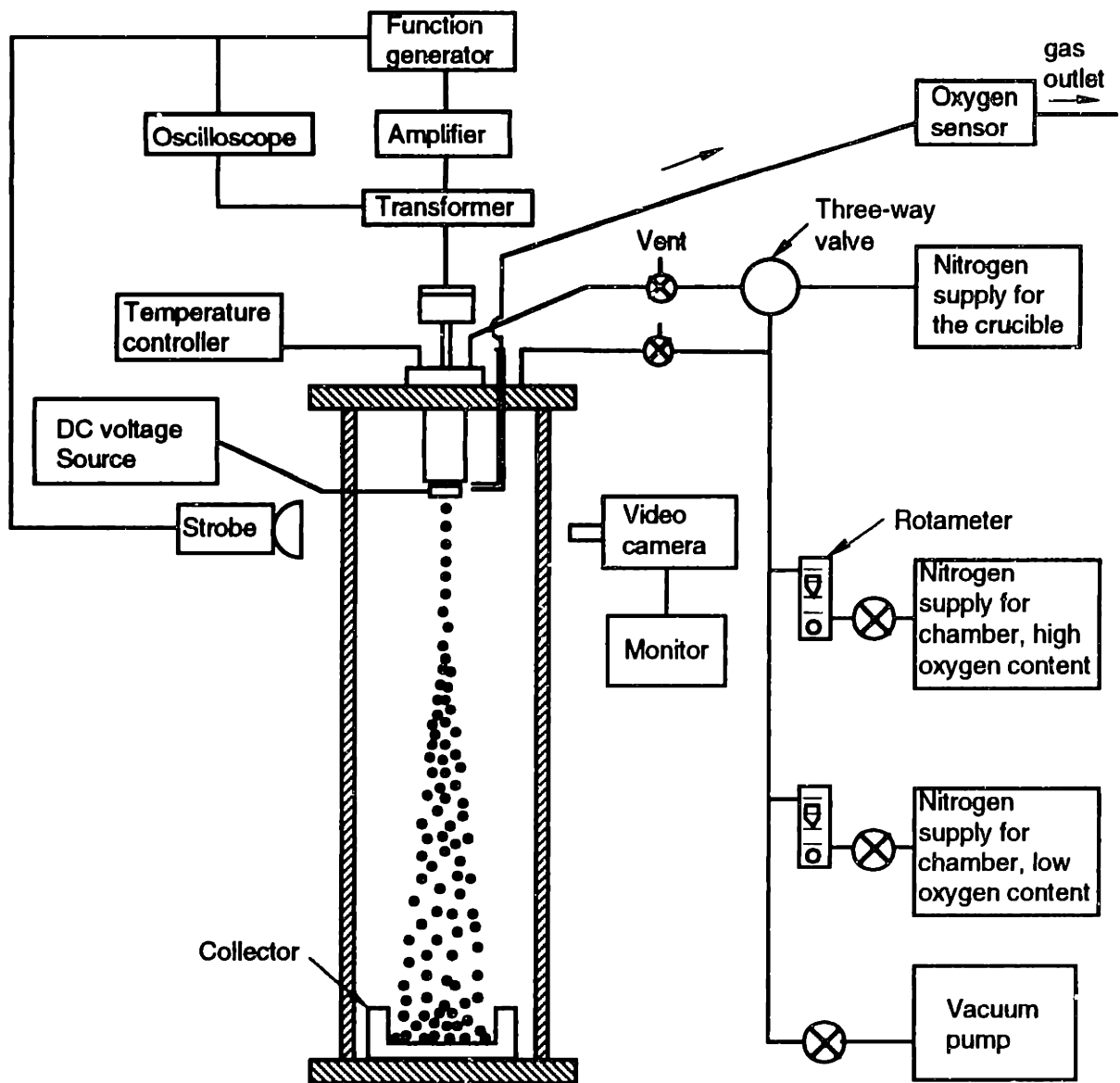


Figure 7.1 Schematic diagram of the UDS apparatus for studying the effects of oxidation on the jet break-up behavior.

7.1.2 Experimental procedure for the investigation of jet break-up

The experimental procedures were similar to those described in Chapter 4 with some modifications. Since the goal of this investigation was to show the effects of oxygen contents in the break-up of molten tin jets, it was necessary to add a scheme to vary oxygen content.

Pure tin was heated to 553 K in the crucible as described in Chapter 4. Before the melting, the spray chamber and crucible were vacuumed to 50 mTorr. They then were filled with pure nitrogen containing less than 5 ppm oxygen. This was repeated two more

times. After the melting of the tin, the spray chamber was filled to the gauge pressure of 35 kPa (5 psig) with nitrogen to the appropriate oxygen content. This was achieved by allowing the nitrogen gases from two tanks containing 5 and 2000 ppm of oxygen to flow through rotameters at a desired volumetric flow rates. By filling the spray chamber with nitrogen from the two tanks of nitrogen supplies at the same flow rate, the oxygen content of the spray chamber was brought to approximately 1000 ppm. The oxygen content was measured then by allowing the gases to pass through the fuel cell in the oxygen analyzer at a low flow rate. Similar procedures obtained desired oxygen contents ranging from 5 to 2000 ppm.

After the oxygen reading stabilized, the molten tin was ejected through an orifice to form a continuous laminar jet with the ejection pressure of 125 kPa (18 psi). When the jet was stabilized, the molten metal was collected in a container to measure the mass flow rate, which then was used to calculate the jet velocity of molten tin as described in Chapter 4.

Perturbation was applied to the molten tin jet to form a train of uniform droplets. The frequency of perturbation was adjusted using a function generator (BK PRECISION, 2 MHz, Model No. 3011B) connected to an audio amplifier (Radio Shack, 20 Watts, Model No. MAP-30) and an oscilloscope (BK PRECISION, 2 MHz, Model No. 2120), which is used to measure the frequency and voltage from the function generator. The signal from an audio amplifier is connected to an audio transformer to increase the voltage to a stack of two piezoelectric crystals (PZT-5A/Navy Type). The voltage to the piezoelectric crystals is attenuated 100 times and connected to the oscilloscope to measure the voltage to the crystals. The amplitude of perturbation was linearly proportional to the voltage to the crystals.

The break-up of the molten tin jet was captured by a CCD video camera (Techni-Quip) and observed by using a monitor (SONY, Model No. PVM-1390). At the same time, the break-up process of molten tin jet was recorded by a VCR (Mitsubishi, Model No. HS-U34). The flashes of a strobe light (Quadtech, Model No. 1538-A) were synchronized with the frequency from the function generator, which was reduced ten times before connecting the strobe light since the range used was 5 to 15 kHz, too high for the strobe light to handle.

The break-up length of the molten tin jet was measured from the screen of the monitor. It was necessary to put a scale (with 18x magnification, for example) on the screen to measure the length. The thickness of the ceramic insulator and the slot distance in the charging ring serve as reference lengths for the scale attached to the screen.

7.1.3 Experimental apparatus and procedures for the investigation of oxide layer thickness

Auger spectroscopy analysis using a Perkin-Elmer Model No. 660 spectroscope measured the oxide layer thickness of tin samples: tin powders produced at 5, 500, 2000 and 200,000 ppm; and tin fiber produced at 200,000 ppm¹. It was crucial to observe the thickness of the oxide layer at the time of the jet break-up rather than the thickness of the oxide that may have grown after the jet had broken into droplets.

As shown in Figure 7.2, the oxide layer continues to grow even though it may slow down over time because of solidification. Two main reasons explain how further oxidation decreases. One is the temperature decrease. As discussed in Chapter 6, oxidation slows down with a decrease in temperature. The temperature decrease also implies that the droplets change from the liquid state to the solid state. Since the diffusion of gas into the solid state is much lower than into the liquid state, the decrease in the activity of oxidation is expected. The other main reason is the formation of the oxide layer on the surface. While oxygen may continue to diffuse into tin, the tin oxide formed on the jet surface acts as a barrier to further oxidation. For example, aluminum has a high affinity for oxygen. However, as soon as aluminum oxide is formed on the surface, it acts as an excellent barrier to further oxidation.

Collection of tin samples

While the oxidation activity of the molten tin decreases with time, it is important that it should not be allowed to continue after the jet break-up. In this experiment, collecting the droplets in silicone oil retarded further oxidation by the rapid decrease in temperature and the shield formed on the surface of droplets by the silicone oil. As noted above (see Figure 7.3, the kinetics of oxidation decreases with the temperature. By quenching the samples in silicone oil, the temperature of droplets is reduced from 553 K to 298 K. At the same time, the droplets are shielded from the ambient air which may contain various levels of oxygen. Thus, oxidation after break-up is prevented. Further oxidation or the chemical reaction between the tin and the silicone oil, $C_{28}H_{32}O_2Si_3$, may result if the silicone oil were to decompose. However, this is unlikely since silicone oil is a very stable compound.

¹ The ejection pressure for all samples was 125 kPa (18 psia). The tin fiber, however, was produced by spraying the tin jet into an atmospheric condition. Since the gauge pressure in the spray chamber was zero, the pressure in the crucible was reduced by 35 kPa (5 psi) to produce tin fibers.

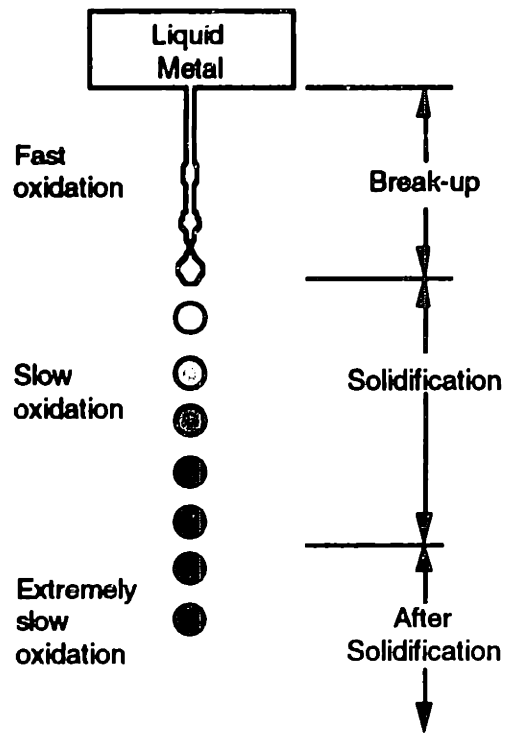


Figure 7.2 Change of oxidation rates with respect to the solidification of droplets.

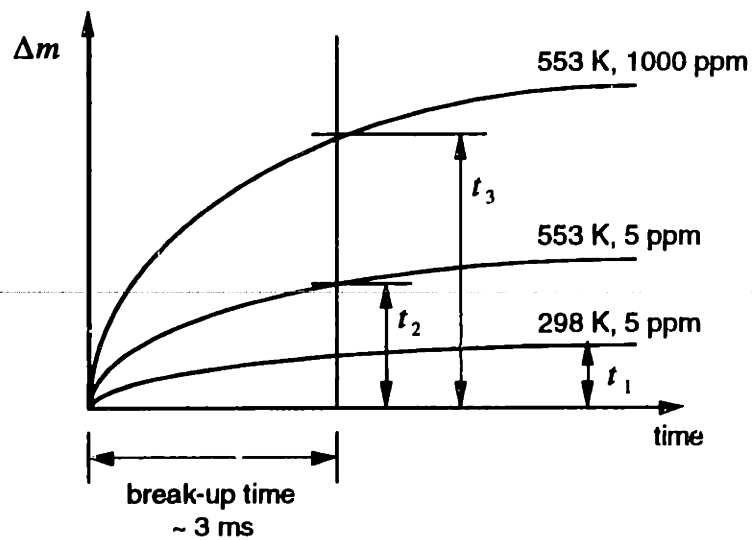


Figure 7.3 Schematics of oxidation curves under different operating conditions.

The distance between the nozzle and the silicon oil was about 15 ms. Since the jet velocity was approximately 5 m/s, the tin jet was exposed to the ambient air for approximately 3 ms. Normally spraying the tin into an atmospheric condition results in fiber formation. However, even in these conditions, the tin jet breaks into droplets as it hits the silicone oil. The tin fibers were collected below 2 m from the orifice, the distance at which the tin jet should have solidified completely, resulting in the exposure time of approximately 400 ms.

Cleaning of droplets

The tin samples collected for the measurement of oxide layer thickness were kept in silicone oil to protect them from the air. While this was useful in retarding further oxidation, it left a very thin film of oil on the surface which had to be removed before the samples were introduced in the vacuum chamber of the Auger spectroscopy machine. The oil had to be removed without exposing the sample to air to avoid further oxidation.

Tin samples were cleaned using three different solvents; 111 trichloroethane (CH_2Cl_2), acetone ($(\text{CH}_3)_2\text{CO}$), and methanol (CH_3OH). Six glass cups filled with solvents—two cups for each solvents—were placed in an ultrasonic cleaner. The oil covered samples were placed on and wrapped inside of a paper sheet. They were agitated in the cup filled with 111 trichloroethane. They were rinsed in another cup filled with the same solvent. They were cleaned in acetone, followed by a rinsing in another cup filled with acetone. They were cleaned finally in methanol, again followed by a rinsing in another cup filled with methanol. The cleaned samples were sealed in a jar filled with methanol while the samples were being transported to the Auger Spectroscopy machine. To prevent any possibility of further surface oxidation of the samples by inadvertent exposure to air, they were transferred to the next cup while they were covered with solvents.

Sample preparation before introduction into the chamber

The samples were mounted on a substrate before introducing them into the vacuum chamber of the Auger Spectroscopy instrument. The mounting was done in a glove bag which was flushed out with and filled, i.e., inflated, with nitrogen which typically contained less than 5 ppm of oxygen.

The mounting accessories were placed in the inflated bag. The nitrogen flush continued to remove any oxygen molecules that may have been left in the bag. Work within the bag then commenced. A thin coat of silver paint was applied to a thin metal sheet. Tin samples were scooped up from the jar filled with methanol. After the methanol

evaporated, the samples were placed on the sheet while the paint was still tacky. After the silver paint dried, the sheet was mounted on a substrate, which was placed inside a transfer chamber. The transfer chamber was sealed inside the globe bag. The transfer chamber was transported from the bag to the introduction chamber in the Auger Spectroscopy instrument. Although the mounting and transfer of samples were done in a globe bag to eliminate further oxidation, this procedure may not have eliminated further oxidation completely. This possibility will be addressed later.

7.2 Results and Discussion

7.2.1 Effect of oxygen content on the jet break-up length

Experiments determined the effect of oxygen levels in the spray chamber on the break-up behavior of molten tin jets. Figure 7.4 shows the break-up of molten tin jets as the oxygen content increases from 5 to 1595 ppm.

Tin was heated to 553 K. The molten tin was forced through a orifice with the diameter of 100 μm . The gauge pressure applied to the crucible was 160 kPa (18 psig) with the spray chamber pressure of 35 kPa (5 psig), resulting in the ejection pressure of 125 kPa (18 psia). As the laminar jet formed, perturbation was applied at the frequency of 11.34 kHz and amplitude of 4.12×10^{-7} m, which resulted from applying 400 V to the piezo-electric crystals. The relationship given in Chapter 4 is as follows:

$$\ln \delta = 1.46 \cdot \ln V_{\text{piezo}} - 23.45 , \quad (7.2.1)$$

where δ is the amplitude of perturbation and V_{piezo} the applied voltage to the piezo-electric crystals. The jet break-up length was measured initially at 5 ppm oxygen. The tin was collected at this oxygen content for 120 to 180 seconds. The spray chamber was evacuated to 50 mTorr and filled to a different oxygen content as described in section 7.1.2. This procedure was repeated until the oxygen content reached the critical limit.

As discussed in Chapter 4, this ejection pressure of 125 kPa (18 psi) should have resulted in a nominal jet velocity of 4.64 m/s. However, the jet velocity was 4.39 m/s. This may have been due to the decrease in nozzle diameter with increasing oxygen content while the tin is collected. Prior experimentation have shown that the jet diameter becomes smaller under atmospheric conditions. Eventually, the jet becomes completely clogged.

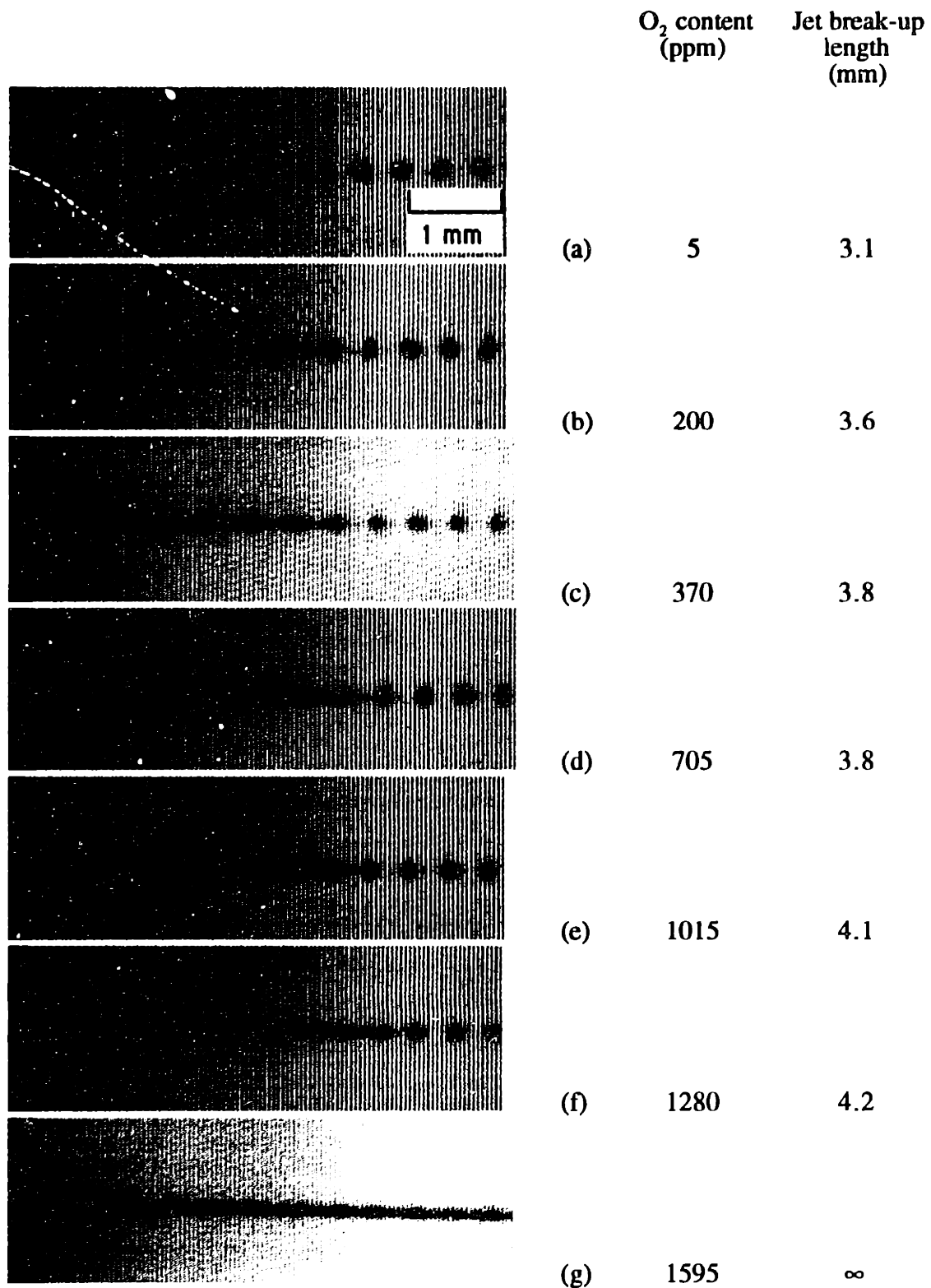


Figure 7.4 Effects of oxygen content on the jet break-up length. The orifice diameter is 100 μm and the perturbation frequency 11.34 kHz. The voltage input to the piezoelectric crystal was 400 V, which translates to a perturbation amplitude of approximately 4.12×10^{-7} m.

The molten tin jet breaks into a train of uniform droplets if the oxygen level is less than approximately 1600 ppm as shown in Figure 7.4, which is represented as run #2 in Figure 7.5. The jet velocity measured for run #1 was 4.56 m/s, a little higher than that of the run #2. Figures 7.5 represents two experiments under the same conditions even though they have slightly different jet velocities. The break-up lengths for both runs increase moderately until the jet does not break into droplets. Figures 7.5 shows that the jet break-up length is weakly dependent on the oxygen levels until the critical oxygen level. In the case of run #1, the jet fails to break at near 1800 ppm, slightly higher than for run #2.

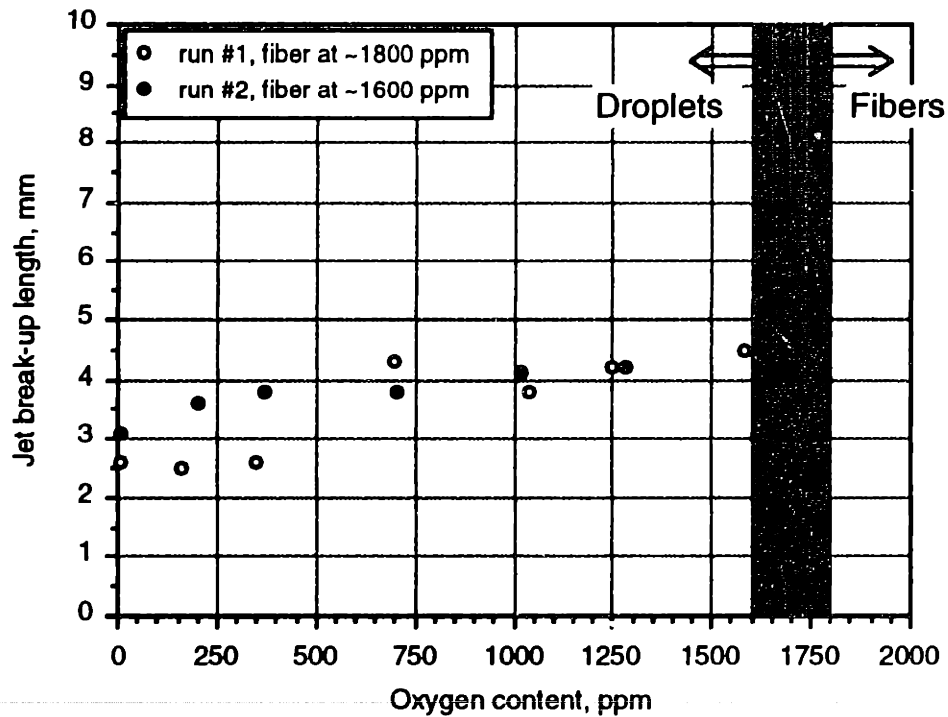


Figure 7.5 The jet break-up length of liquid tin versus oxygen concentration in the spray chamber. The orifice diameter is 100 μm , the perturbation frequency 11.34 kHz. The voltage input to the piezoelectric crystal was 400 V, which translates to a perturbation amplitude of approximately 4.12×10^{-7} m.

7.2.2 Effect of amplitude on the jet break-up length

Figure 7.6 shows the effect of amplitude on the jet break-up length. The experimental conditions were the same as described in Section 7.2.1, except that the oxygen content was held at 1595 ppm while the amplitude of perturbation varied. The voltages applied to the piezo-electric crystals were 0, 400, and 600 V, which translated into amplitudes of perturbation at 6.5×10^{-11} , 4.12×10^{-7} , and 7.46×10^{-7} m. As shown in Figure 7.6, the contour of the jet surface seemed to be very smooth when no perturbation, i.e., at zero voltage to the piezo-electric crystals, was applied.

The jet surface seemed to have ripples on the surface as the perturbation amplitude was increased to 4.12×10^{-7} m (400 V); however, the amplitude was not big enough to overcome the surface changes which may have taken place due to the surface chemical reaction at 1595 ppm of oxygen. When the amplitude was nearly doubled to 7.46×10^{-7} m (600 V), the amplitude was big enough to overcome the surface changes and break the molten tin jet into a train of uniform droplets.

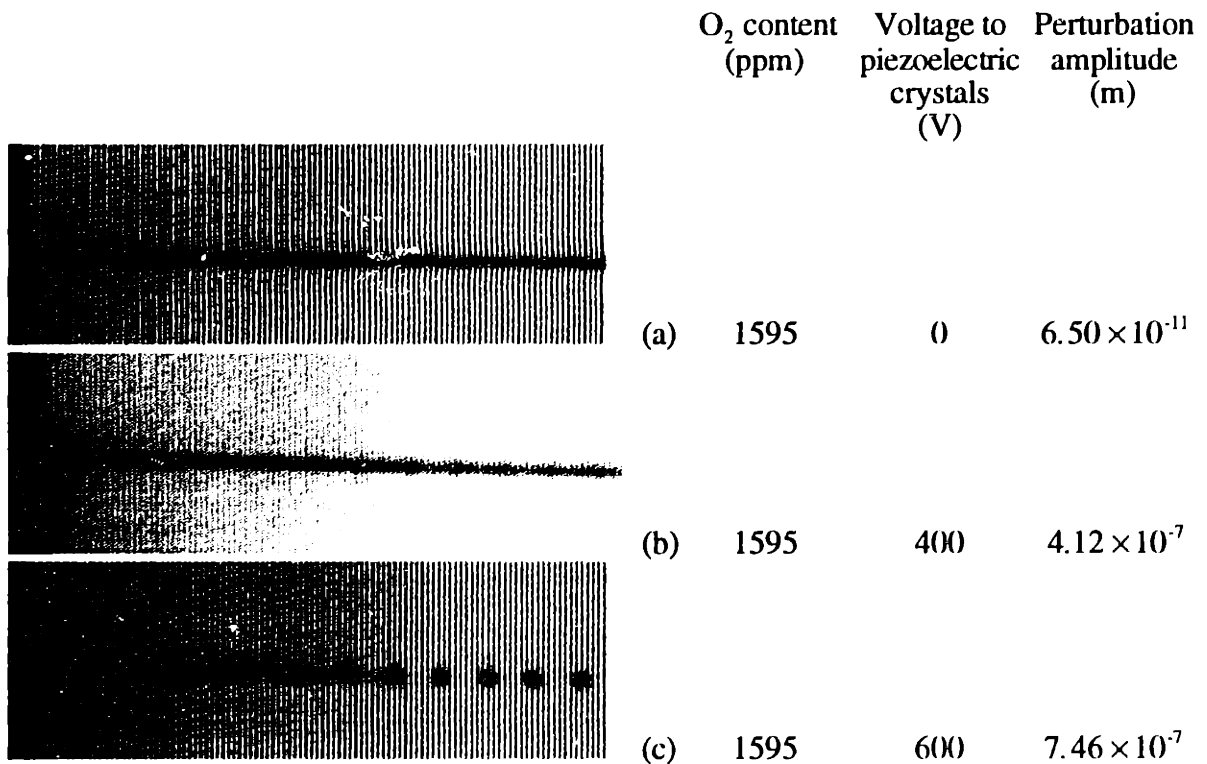


Figure 7.6 Effect of perturbation amplitude on the jet break-up length. The diameter of the orifice used was 100 μm . The frequency applied was 11.34 kHz.

This result implies that even if the oxygen content is more than 1600 or 1800 ppm, i.e., the critical oxygen content at the perturbation amplitude of 400 V, the molten tin jets can be broken into a train of uniform droplets by increasing the perturbation amplitude. It also implies that if the perturbation amplitude is not high enough, the jet will not be broken into a train of uniform droplets at 1600 to 1800 ppm.

7.2.3 Effect of dimensionless wavelength on the jet break-up length at various partial pressures of oxygen

Figure 7.7 shows the effect of the dimensionless wavelength on the jet break-up length at various partial pressures of oxygen. Section 2.2 describes the dimensionless wavelength, λ/d_j , at which the maximum growth rate occurs is:

$$\frac{\lambda}{d_j} = \pi \sqrt{2 + \frac{3\mu_l}{\sqrt{\rho_l \sigma_l d_j}}} = \pi \sqrt{2 + 3\text{Oh}}, \quad (7.2.2)$$

where λ is the wavelength between two neighboring droplets, d_j the jet diameter, μ_l the viscosity of liquid, ρ_l the density, σ_l the surface tension, and Oh the Ohnesorge number, defined as $\text{Oh} = \mu_l / \sqrt{\rho_l d_j \sigma_l}$. As written in equation (7.2.2), the dimensionless wavelength at which the maximum growth rate occurs should increase with the increase in the Ohnesorge number as shown in Figure 2.6. The increase in the Ohnesorge number also indicates the decrease in the growth rate, i.e., the increase in the jet break-up length. As described earlier, the jet break-up length is at a minimum when the dimensionless wavelength is at the maximum growth rate.

The dimensionless wavelength changes at which the minimum jet break-up length occurs, and the decrease in the break-up length indicate that there may have been the material property changes. The material property changes would be the increase in the viscosity and/or the decrease in the surface tension. The oxygen contents used in this case were 5 and 500 ppm. The jet velocities measured for 5 and 500 ppm were 4.76 and 4.69 m/s, respectively.

For both cases, the jet break-up length is lowest when the dimensionless wavelength is 4.10. The dimensionless wavelength in Figure 7.7 was calculated using the average velocity (4.64 m/s) for the ejection pressure of 125 kPa (18 psia). The break-up lengths for both cases at other dimensionless wavelengths are similar although the break-up lengths of 500 ppm are slightly lower than that of 5 ppm. The differences insignificant. Figure 7.7 implies that the material property changes from 5 to 500 ppm oxygen content are

not sufficient to change the dimensionless wavelength at which the maximum growth rate occurs, or that the effects due to the increase in viscosity and/or the decrease in the surface tension cancel out each other.

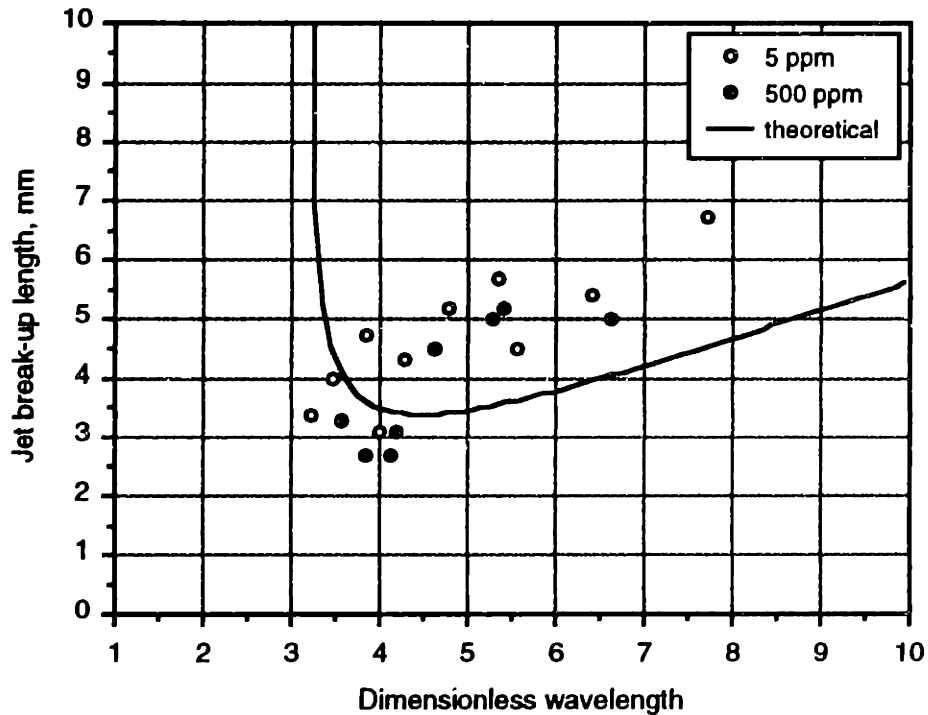


Figure 7.7 Effect of frequency and dimensionless wavelength on the jet break-up length due to oxygen content. Orifice diameter is 100 μm and ejection pressure 125 kPa. An average velocity of 4.64 m/s was used. 400 V was applied to the piezoelectric crystal to provide the perturbation amplitude to the nozzle area.

7.2.4 Oxide layer thickness measurement by the Auger Electron Spectroscopy

The powders and fibers produced were examined for their oxide layer thickness by AES. The samples were collected, cleaned, and placed in the transfer chamber as described in Section 7.1.3. After preparation, the transfer chamber was put into the chamber of the AES instrument. The surface of the samples was examined for chemical elemental compositions through the AES chemical elemental survey.

A typical result of the survey is shown in Figure 7.8, which represents the initial survey of tin powder produced at 5 ppm oxygen. The figure shows the oxygen peaks in the kinetic energy ranges 495 to 520 eV, the carbon peaks in 245 to 285 eV, and the tin

peaks in 415 to 445 eV. Only traces of oxygen and tin were expected. However, the survey also showed traces of carbon, which could have come from residues of the silicone oil or methanol. There is no traces of silicone (at near 1620 eV) in Figure 7.8, indicating that silicone oil was completely removed from the sample. Other samples showed some traces of silicone, though they were hardly detectable.

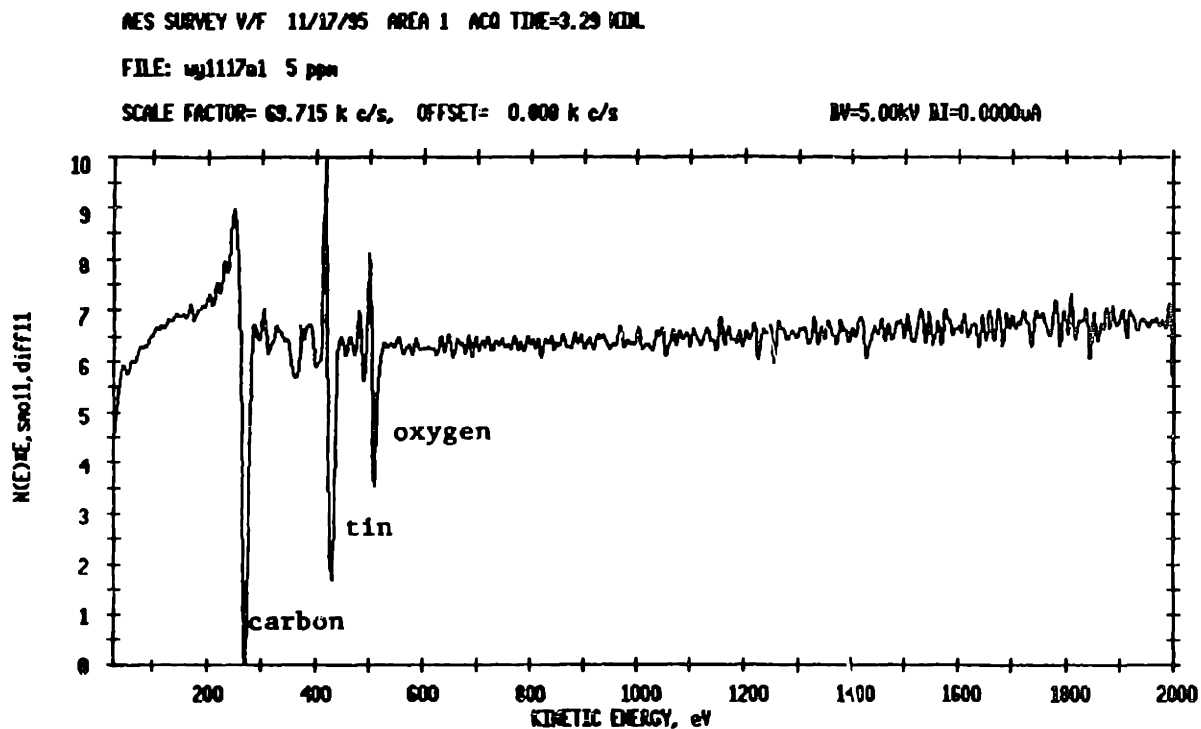


Figure 7.8 Auger electron spectroscopy survey for chemical elements on the surface of a sample.

Figures 7.9 to 7.11 show the montages of the oxygen, carbon, and tin intensities, respectively, for tin powder produced at 2,000 ppm oxygen¹. Figure 7.12 shows the montage of the oxygen intensities for tin fiber produced at 200,000 ppm². In the first two cycles, the surface composition of a tin sample was examined to check its chemical stability. The montages for oxygen intensities in Figures 7.9 and 7.12 show that the elemental analysis is stable for the first two non-sputtering cycles. The montages for the carbon and tin in Figures 7.10 and 7.11 also show that they are stable for the first two non-sputtering cycles.

The surface of the sample were sputtered away with argon ion gun settings of 2 kV and 10 $\mu\text{A}/\text{cm}^2$ until oxygen could not be detected. The sputtering period was six seconds. The "sputtered-away" surface was analyzed by the electron beam. The sputtering cycle was repeated until no traces of oxygen was detected. The procedure was repeated for tin powders produced at 5, 500, 2,000, and 200,000 ppm and tin fibers produced at 200,000 ppm. The montages shown in Figures 7.9 to 7.12 represent only the 2,000 ppm powder and the 200,000 ppm fiber. Although the montages from other samples are not provided, the results of the oxygen, carbon, and tin intensities for tin powders produced at 5, 500, 2000, and 200,000 ppm, and tin fibers produced at 200,000 ppm, respectively, are summarized and graphically shown in Figures 7.13 to 7.17, respectively.

As shown in Figures 7.13 to 7.17, no oxygen is detectable in any sample after the three sputtering cycles (18 seconds). It was expected that it would take more cycles to remove oxygen from the samples produced at a higher oxygen content, i.e., the oxide layer was expected to be thicker for the samples produced at higher oxygen contents. However, since all samples took only three sputtering cycles, the oxide layer for all samples was more or less the same.

¹ Section 7.2.1 concluded that the jet did not break into a train of uniform droplets if the oxygen content in the spray chamber was higher than 1,600 to 1,800 ppm. Thus, it seems peculiar that the tin powders were produced at 2,000 ppm. The results are actually not contradictory. Since the tin powders for the oxide layer thickness measurement were collected in silicone oil to prevent further oxidation, the disturbance created as the jet entered the oil was sufficient enough to break the jet into droplets. The droplets so created at 2,000 ppm or even at 200,000 ppm (atmospheric condition), however, were not spherical but rather like tear-drops. Nonetheless, they are categorized as droplets for the purposes of this study.

² The tin fiber was exposed to the gas in the spray chamber for approximately 400 ms before immersion in silicone oil. Tin droplets were exposed for approximately 3 ms as discussed in Section 7.1.3.

NES PROFILE 12/27/95 START=0, END=0, NTH=1
FILE: wj1227a10 2000 ppm

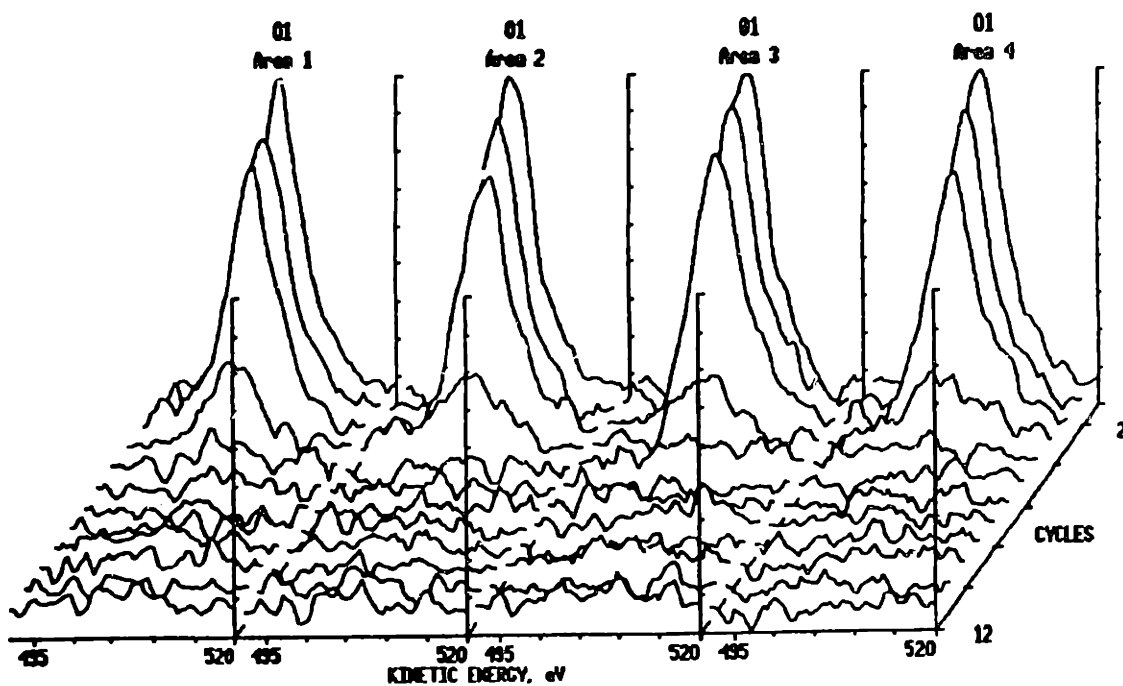


Figure 7.9 Montage of oxygen traces at four different places on the tin powder produced at 2,000 ppm oxygen.

NES PROFILE 12/27/95 START=0, END=0, NTH=1
FILE: wj1227a10 2000 ppm

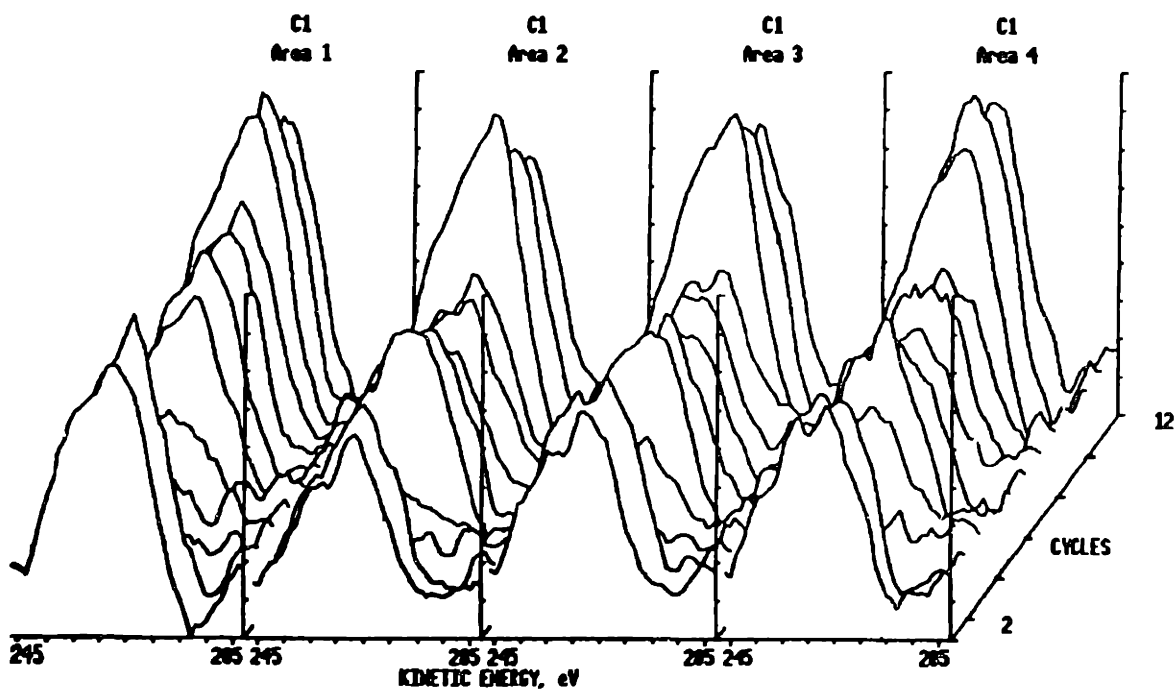


Figure 7.10 Montage of carbon traces at four different places on the tin powder produced at 2,000 ppm oxygen.

AES PROFILE 12/27/95 START=0, END=0, NTH=1
FILE: wj1227a10 2000 ppm

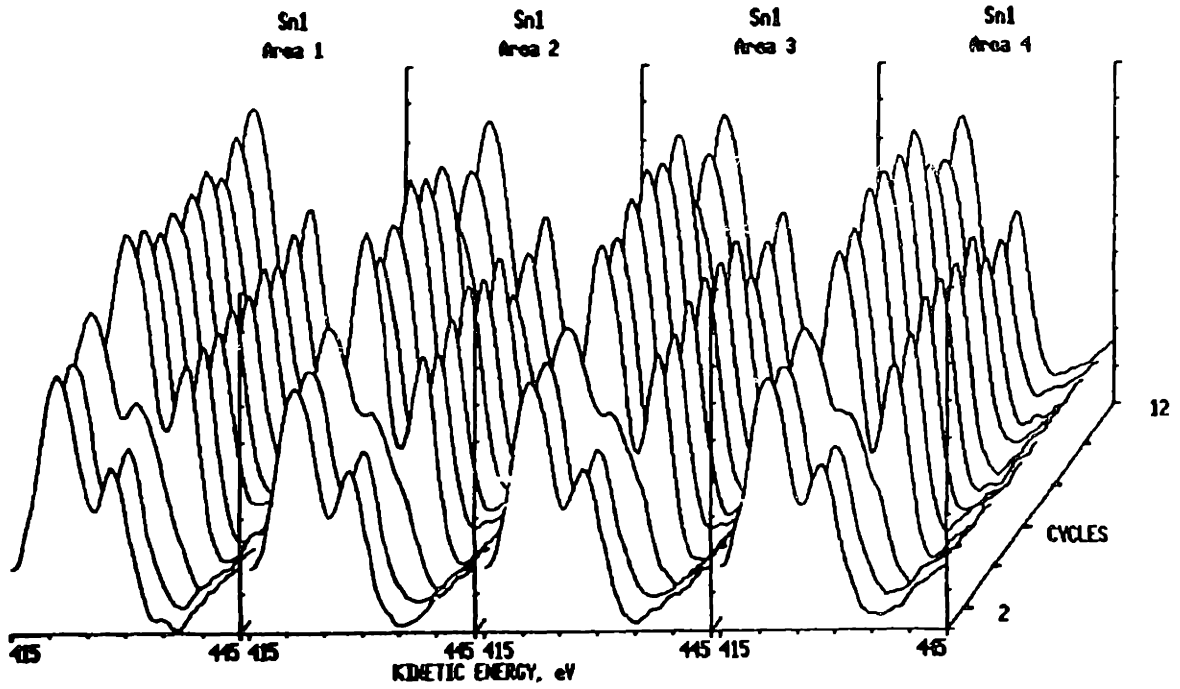


Figure 7.11 Montage of tin traces at four different places on the tin powder produced at 2,000 ppm oxygen.

AES PROFILE 12/28/95 START=0, END=0, NTH=1
FILE: wj1228b2 ata fiber

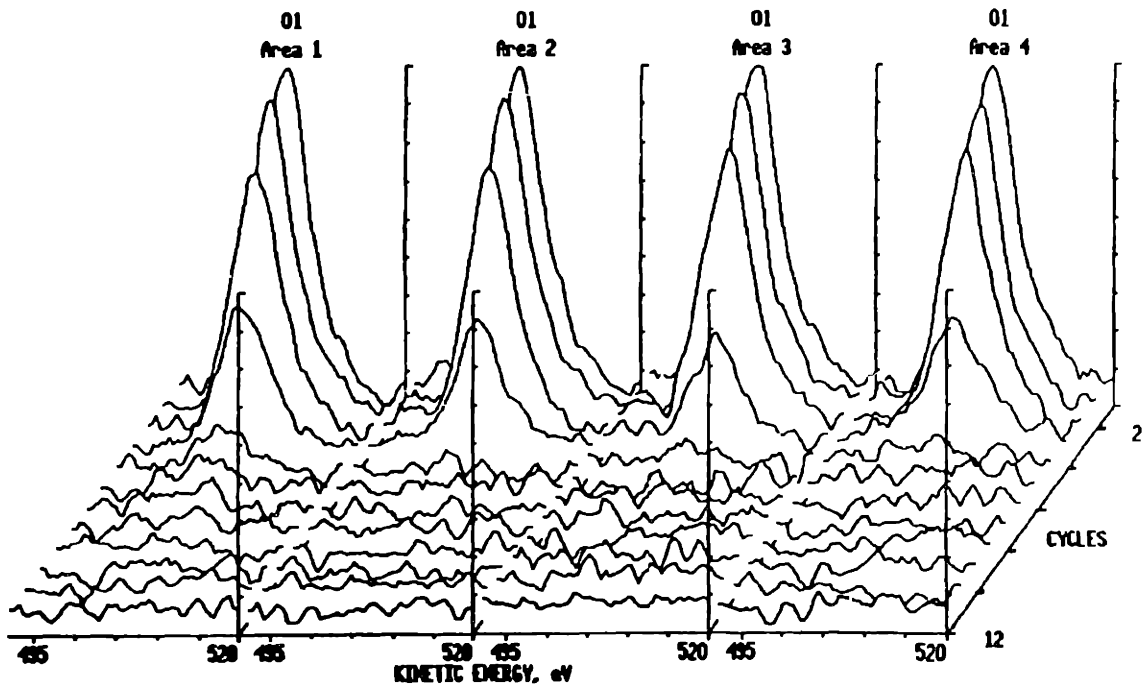


Figure 7.12 Montage of oxygen traces at four different places on the tin fiber produced at 200,000 ppm oxygen.

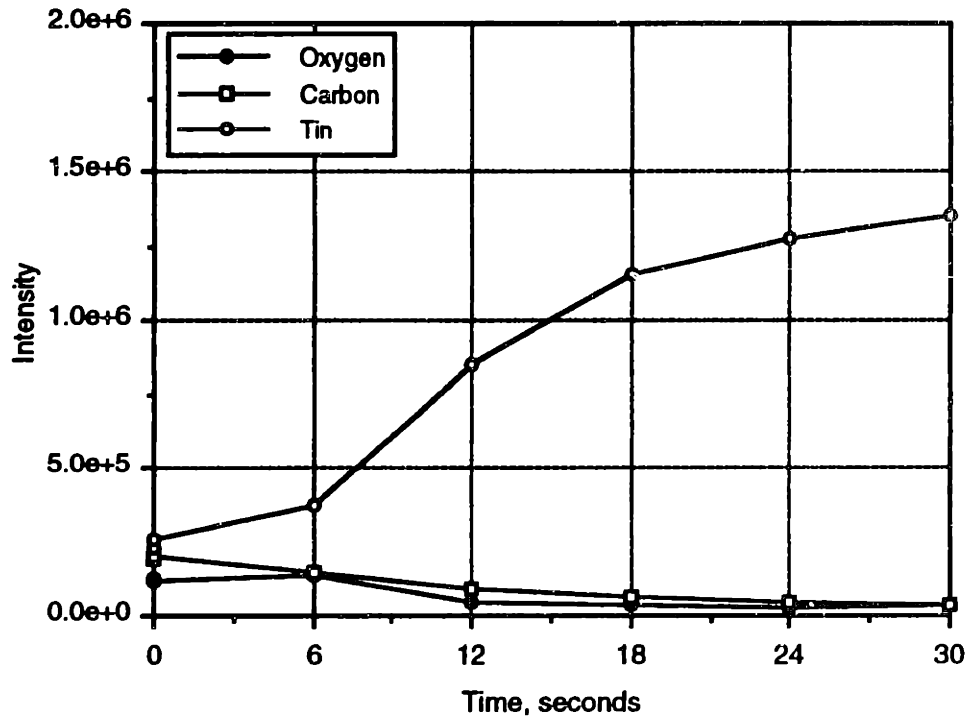


Figure 7.13 Intensity of oxygen, carbon, and tin of tin droplets produced at the oxygen level of 5 ppm.

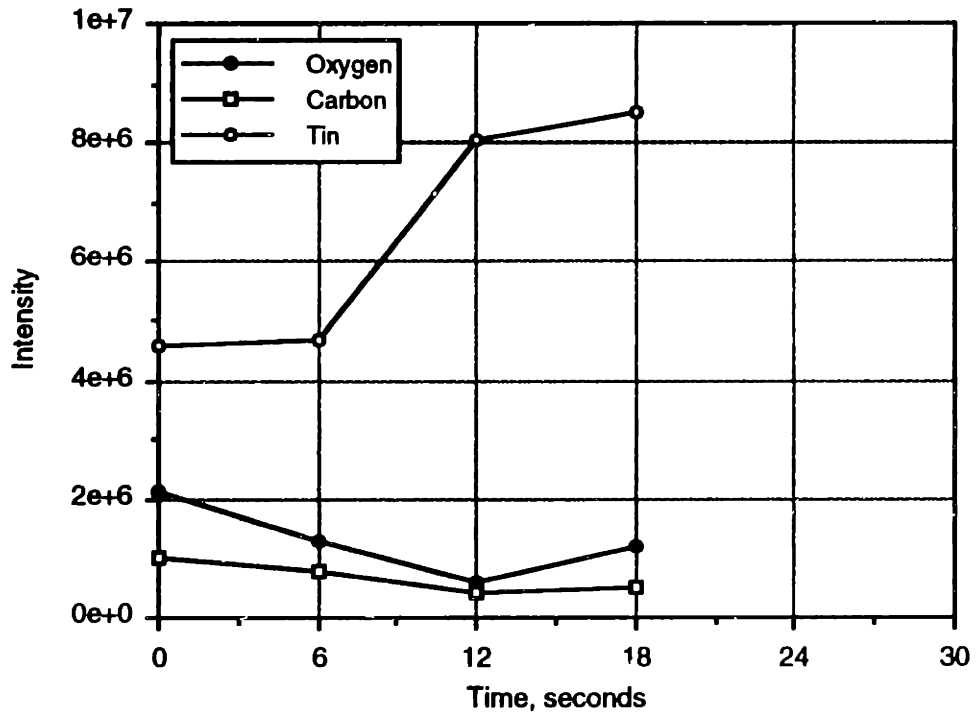


Figure 7.14 Intensity of oxygen, carbon, and tin of tin droplets produced at an oxygen level of 500 ppm.

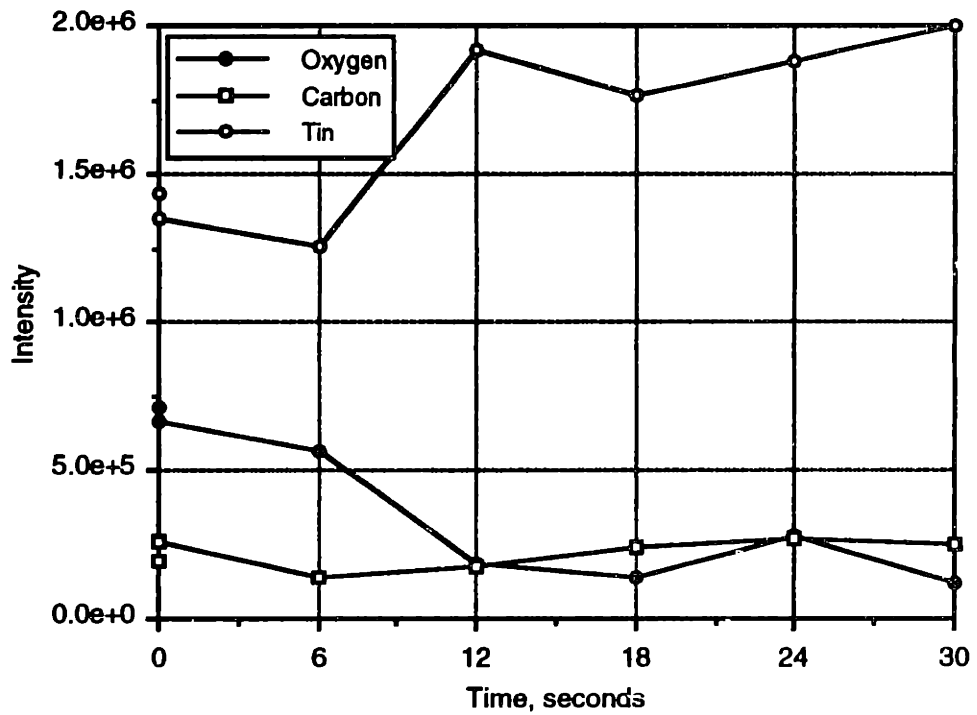


Figure 7.15 Intensity of oxygen, carbon, and tin of tin droplets produced at an oxygen level of 2,000 ppm.

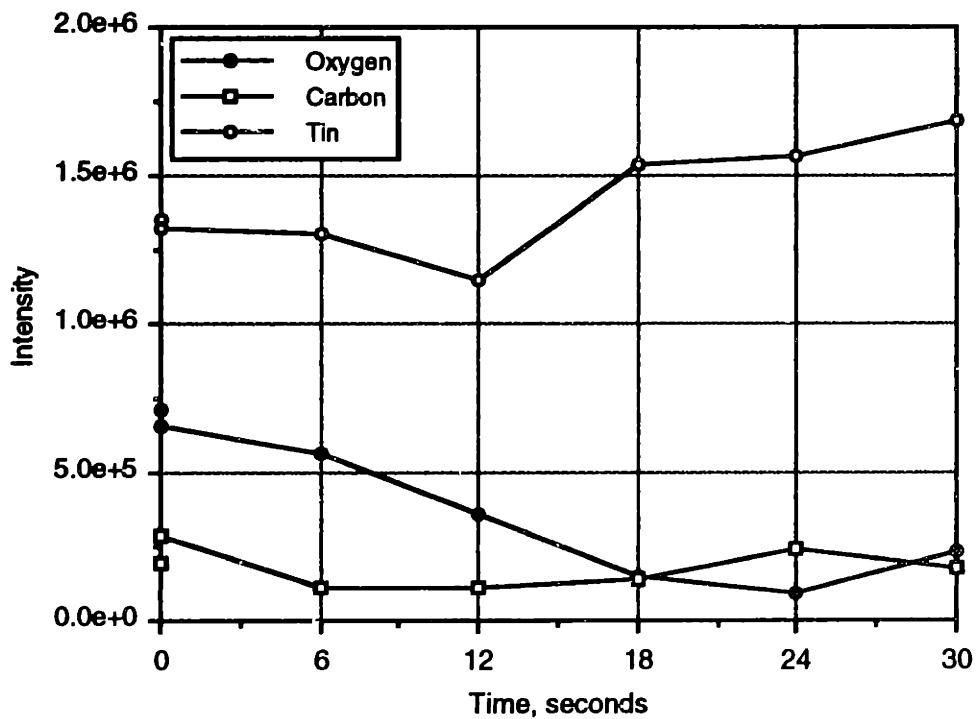


Figure 7.16 Intensity of oxygen, carbon, and tin of tin droplets produced at an oxygen level of 200,000 ppm.

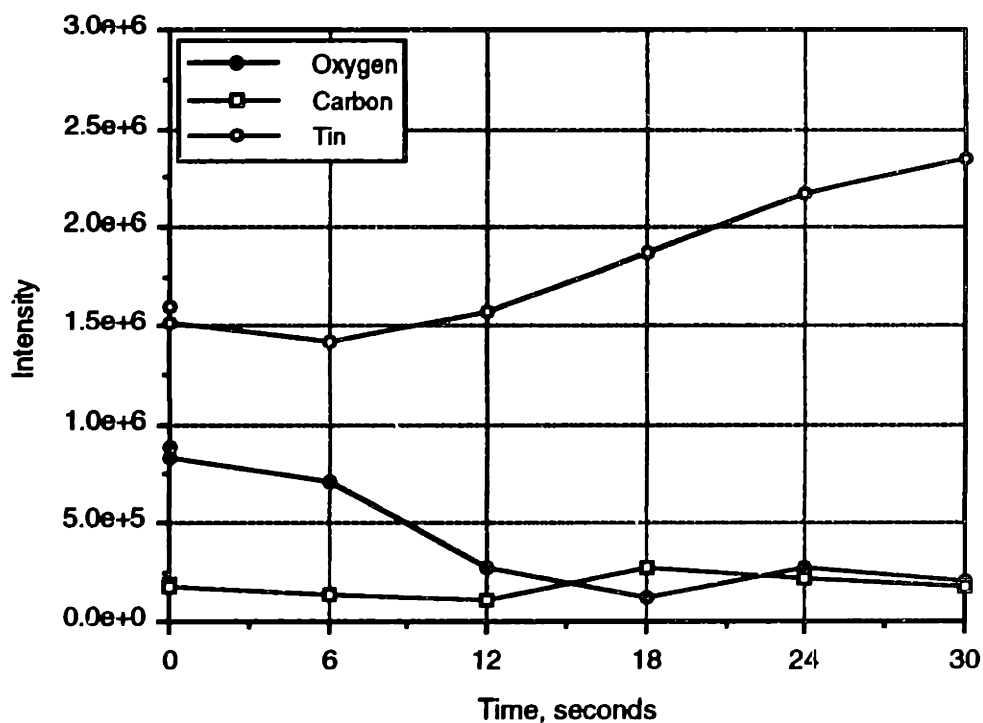


Figure 7.17 Intensity of oxygen, carbon, and tin of tin fiber produced at an oxygen level of 200,000 ppm.

It can be argued that the oxygen intensity for the 500 ppm tin powder is increasing as shown in Figure 7.14; however, this can be attributed to the noise factor. As can be seen in the montage graphs for the oxygen intensities in Figures 7.9 (2,000 ppm powder) and 7.12 (200,000 ppm fiber), there is noticeable noise after the third sputtering cycle. Thus, the intensity of oxygen must be examined carefully to determine if the reading truly represents the actual intensity. Figures 7.9 and 7.12 also reveal that, after the second sputtering cycle, the oxygen intensities for the 200,000 ppm tin fiber seem little higher than those of the 2,000 ppm tin powder. However, after the third sputtering cycle, there are negligible traces of oxygen for both cases. This was the case with all the samples.

To estimate the thickness of the tin oxide layer from the AES measurement, the procedure was repeated on a tantalum sample with an oxide thickness of 100 nm using the same argon ion settings of 2 kV and $10 \mu\text{A}/\text{cm}^2$ as mentioned previously. As shown in Figure 7.18, it takes about 200 cycles (1200 seconds) to remove the traces of oxygen from the surface of tantalum. By comparing the sputtering times for tantalum and tin, the relative thickness of tin samples could be determined.

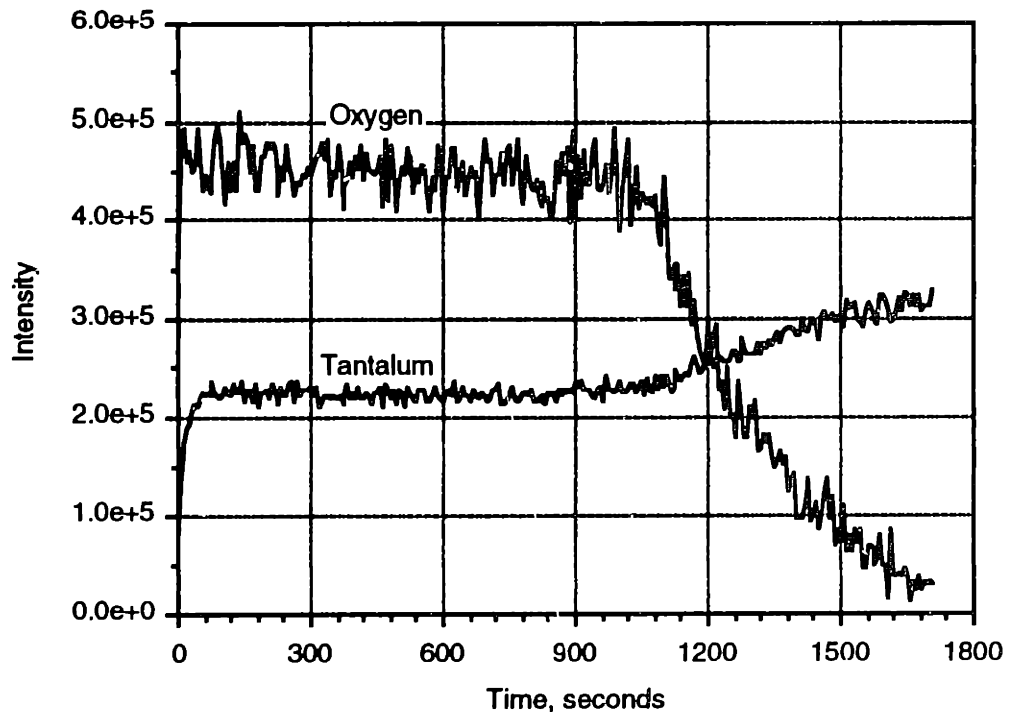


Figure 7.18 Intensity of oxygen and tantalum for tantalum with 100 nm oxide layer thickness.

Since approximately 200 cycles were necessary for sputtering the 100 nm tantalum oxide layer, it can be estimated that 0.5 nm of oxide layer was removed in a single sputtering cycle. Thus, the oxide layer thickness of tin for all cases was estimated to be about 1.5 nm, since it took three sputtering cycles.

The sputtering of atoms depends on the hardness of the material. It typically is easier to sputter away softer materials, although hardness is not the only criterion. Since tin is a softer metal than tantalum, the actual thickness of tin oxide should be higher than the estimate (Shaw, 1996). However, direct comparison can estimate the oxide layer thickness within $\pm 20\%$ error (Moulder, 1996). Even if the errors associated with the comparison between two different metals were considered, the tin oxide for all cases should be greater than 1.5 nm but less than 2.0 nm (1.8 nm, to be more precise).

These results are not what had been expected. It had been expected that the oxide layer thickness increased with the increase in the oxygen contents in the spray chamber. The following arguments explain why the oxide layer thicknesses for all samples were more or less the same:

- (i) The oxide layer was formed as soon as the jet came into the spraying chamber, and the layer on the surface acted as a barrier against further oxidation into the pure metal. Thus, the thickness measured was the terminal thickness for the relatively low temperature oxidation under a wide ranges of oxygen levels.
- (ii) Though oxygen molecules reacted with the surface of the molten tin, the nucleated sites may have taken some time to grow and cover the surface, resulting in a sheath of oxide film covering the droplet surface in the silicone oil.
- (iii) It is possible that the tin may have reacted with the oxygen in the air during the sample cleaning using the solvents.
- (iv) The oxygen molecules in the silicone oil or the methanol could have decomposed, thereby reacting with the tin to form an oxide layer.
- (v) Though the transfer of the samples to the transfer chamber was done in a inflatable globe bag filled with nitrogen containing less than 5 ppm oxygen, it is possible that this transferring time (typically about 300 seconds) and the 5 ppm oxygen content were sufficient enough to oxidize the surface of samples.

It can be concluded, therefore, that there are still many possible reasons why the oxide layer thickness at the time of the jet break-up is not accurately estimated with the currently experimental procedures. *In-situ* measurements of oxide layer thickness would be ideal in this case; however, they are not practically possible in the current UDS apparatus.

7.2.5 Area mapping of oxide layer surface by the Auger Electron Spectroscopy

Although there was no extensive area mapping on the tin samples, it was performed on the tin powder produced at 2,000 ppm to observe the variations in the oxide layer thickness in depth wise along the surface, the oxide islands formation on the surface, or the continuity of oxide layer. The area mapping was done on the 20 by 20 μm area and with the resolution of 32 pixels in each direction. The size of the electron beam (which detects the chemical elements on the surface) was about 500 nm (5000 Å). The area mapping revealed that there were traces of oxygen on the surface after one sputtering cycle and there

were no traces of oxygen after seven sputtering cycle. (No area mapping was performed in between one and seven sputtering cycle.)

White dots in the area mapping picture show oxygen, and black no oxygen. The picture is not shown in this thesis since it does not augment the results presented in Section 7.2.4. The area mapping was performed with the resolutions of 128 pixels in each direction on the 20 by 20 μm area, increasing the sampling time by 16 times. Increasing the number of pixels did not reduce the beam size, however. The result was more or less the same as with 32 pixels, that is, it was inconclusive.

The area mapping performed with the electron beam size of 500 nm was not promising enough to proceed further with the investigation on the variations on the oxide layer surface. For results of the area mapping to be meaningful, it is recommended that the beam size be less than the thickness of the oxide layer, about 2 nm in this case.

The AES instrument used in this study has only a single channel. If the sampling time is high, it allows the sputtered-away surface to react with oxygen present in the AES chamber even though the chamber contains very few oxygen molecules. (A typical operating vacuum in the AES chamber is 10^{-10} to 10^{-9} Torr.). Thus, it is recommended that a multi-channel instrument, which should increase the sampling rate, thereby decreasing the sampling time between the sputtering cycles.

7.2.6 Effect of oxide film thickness and its ultimate strength on the jet break-up

Assuming that the oxide layer of a certain thickness is formed instantaneously, it is desirable to see whether the oxide layer (or sheath) can withstand the force due to the surface tension of liquid. Figure 7.19 shows the force balance on a thin-walled, cylindrical pressure vessel. Assume that the vessel is subjected to a pressure differential, ΔP . The force due to fluid per unit length, F_{fluid} , tending to separate two halves of the cylinder is given by:

$$F_{fluid} = \Delta P \cdot 2r_j = \Delta P \cdot d_j, \quad (7.2.3)$$

where r_j is the inside radius. The force acting on the wall, F_{wall} , is given by:

$$F_{wall} = \sigma_h \cdot t, \quad (7.2.4)$$

where σ_h is the hoop stress on the wall and t the wall thickness of cylinder.

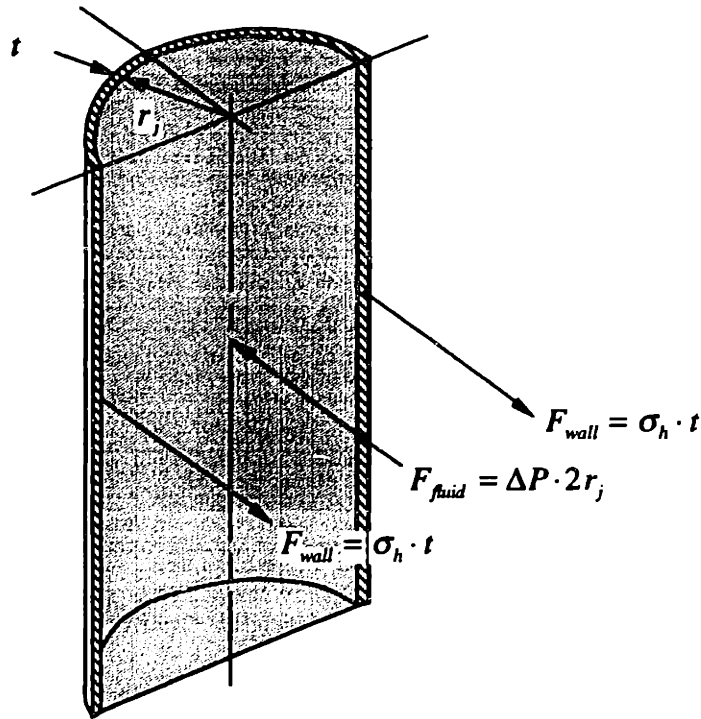


Figure 7.19 Free-body diagram.

Force balance on the thin-walled cylindrical vessel yields the following relationship:

$$F_{fluid} = 2 \cdot F_{wall} . \tag{7.2.5}$$

Combining equations (7.2.3), (7.2.4), and (7.2.5) results in the thickness which can withstand the pressure difference between the inside and outside of the jet:

$$t = \frac{\Delta P \cdot d_j}{2\sigma_h} . \tag{7.2.6}$$

Figure 7.20 shows the flow of liquid inside of the column of jet due to the pressure caused by the surface tension. Pressures in the valley area, the peak area, and the outside of jet are represented by P_v , P_p , and P_o . The radii are represented by r_1 , r_2 , r_3 , and r_4 as shown in the figure. The pressure differences between P_p and P_o ; and P_v and P_o can be written as:

$$P_p - P_o = \sigma_l \left(\frac{1}{r_1} + \frac{1}{r_2} \right), \tag{7.2.7}$$

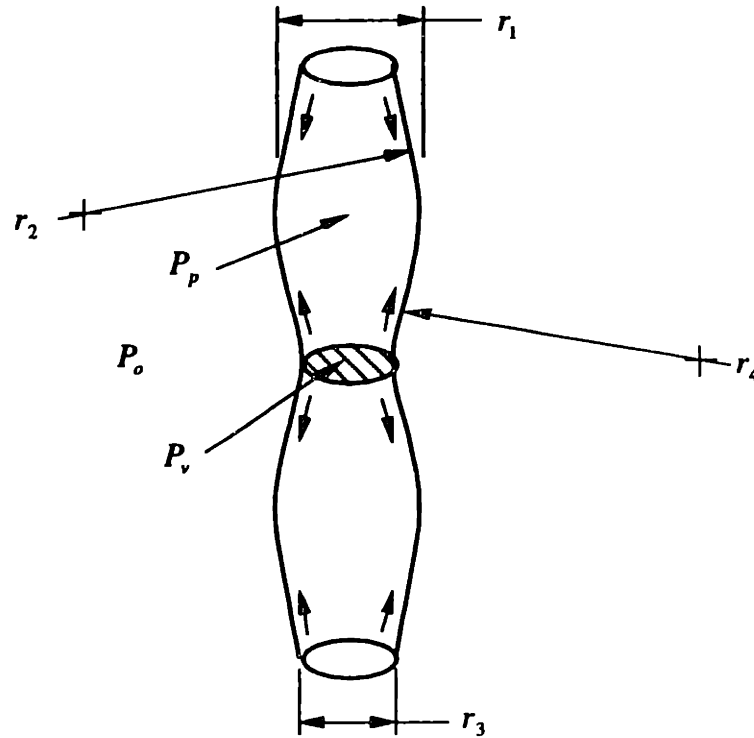


Figure 7.20 Flow of liquid inside of the column of jet due to the pressure caused by surface tension.

and:

$$P_v - P_o = \sigma_l \left(\frac{1}{r_3} - \frac{1}{r_4} \right). \quad (7.2.8)$$

It can be assumed that $r_1 \ll r_2$ and $r_3 \ll r_4$ as the liquid is beginning to break into droplets, making the second terms in the bracket for (7.2.7) and (7.2.8) negligible. Since $r_1 > r_3$, the pressure relationships can be written as:

$$P_v > P_p > P_o \quad (7.2.9)$$

Thus, the flow as indicated by the arrows in Figure 7.20 is justified by the above equation. Assuming that $r_1 = r_3 = r_j$, the pressure differences from equations (7.2.7) and (7.2.8) can be reduced to the following:

$$\Delta P \approx P_v - P_o \approx P_p - P_o \approx \frac{\sigma_l}{r_j} = \frac{2\sigma_l}{d_j} \quad (7.2.10)$$

Substituting the above equation into equation (7.2.6) yields:

$$t = \frac{\sigma_l}{\sigma_h} = \frac{\sigma_l}{\sigma_{UTS}} \quad (7.2.11)$$

Equation (7.2.11) shows the minimum thickness required to resist the collapse of a thin wall. The relationship is the ratio of the surface tension of fluid to the hoop stress, or the yield fracture strength of the oxide film. The equation is valid when the oxide film is continuous and the surface properties are not degraded by cracks or pores.

Assume that the yield strength of tin oxide at room temperature is 13 MPa and that the surface tension of tin at its melting point is 0.544 N/m. (Typically, the ultimate tensile strength of oxides ranges from 10 to 100 MPa where as that of engineering metals ranges from 100 to 1000 MPa.) Substituting these values into equation (7.2.11) yields the minimum thickness of oxide that would prevent thin wall collapse to be 42 nm. This value is very high compared with the oxide layer thickness of 1.8 nm measured by the AES.

Table 7.1 shows oxide film thickness calculated for corresponding values of ultimate tensile strengths. For example, the surface tension of a liquid should be able to collapse a 1.8 nm thin wall that has an UTS of up to 300 MPa, which is in the range of wrought aluminum alloys. However, if the oxide film is formed on the liquid metal surface, it should be noted that the interfacial energy (between the oxide and the liquid metal) may decrease drastically. Thus, the surface tension value used for calculations in Table 7.1 may be too high. If lower surface tension is used for the calculation, the oxide film thickness capable of withstanding the pressure should decrease.

Table 7.1 Thickness of oxide film capable of withstanding the pressure caused by the surface tension of a liquid of 0.544 N/m

Ultimate tensile strength (MPa)	Oxide film thickness (nm)
13	41.8
100	5.4
300	1.8
1000	0.54

7.3 Conclusions

The oxide layer on the metal surface should increase in thickness with the increase of the oxygen content. It has been observed that sufficiently high oxygen concentration in the spray chamber causes a continuous laminar jet of molten tin to form a fiber rather than a train of droplets. Thus, the hypothesis of the study on the role of surface oxidation was that the molten metal jets do not break into a train of uniform droplets due to the formation of an oxide layer build-up to a certain critical thickness. The jet break-up lengths under a wide range of oxygen concentrations were observed and measured as a means by which to check the critical concentration level under which the jets do not break. It was observed that when the spray chamber contained the oxygen concentration levels of 1600 to 1800 ppm at 35 kPa (5 psig), the 100 μm tin jet did not break under the conditions described in Section 7.2.1.

The tin droplets and fiber were produced and collected in silicone oil for their thickness measurement at the time of break-up. The samples were measured with the AES instrument after being cleaned in the solvents. However, the oxide layer thickness of tin powders produced at 5, 200, 2,000, and 200,000 ppm and tin fibers produced at 200,000 ppm oxygen were more or less the same, about 1.8 nm. This unexpected result is attributed to further oxidation that may have occurred after the jet break-up. If the oxide layer were thicker for higher oxygen concentration in the spray chamber, the thickness differences were less than the sputtering depth used in the AES measurement which was about 0.5 nm. It may have been possible that the oxide initially grows in depth wise to a certain terminal thickness, and grows laterally after the jet break-up, making it difficult to assess whether the measurements by the AES instrument represent the thickness at the time of break-up.

Although *in-situ* measurements of liquid tin material properties and the tin oxide layer thickness at the time of a jet break-up could have shed some light on the effects of oxygen concentrations, they were not practical. Microstructural changes, i.e., from amorphous to crystalline structures, which could have taken place as the jet broke into a train of uniform droplets in the UDS apparatus could not have been observed. The phase changes that might have occurred with the increase in the oxygen concentration could not have been observed with the video monitor.

The area mapping was performed on tin droplets produced at 2,000 ppm to investigate the variations of the thickness depth-wise, the oxide islands formation on the surface, and the continuity of the oxide layer. However, the results were inconclusive. The electron beam diameter of 500 nm (5,000 Å) may have been too large to detect the

variations of the thickness depth wise, oxide islands formation, or the continuity of oxide layer.

The effect of a thin oxide film on the jet break-up was estimated by assuming that the film was solid and continuous. It was further assumed that such a jet breaks under the force from only the surface tension of the molten metal. This resulted in the critical thickness of the solid oxide layer, which was determined by the ratio of the surface tension of molten metals to the ultimate tensile strength of the surface metal oxide.

Nomenclature

d_j	jet diameter
F_{fluid}	force due the internal pressure of fluid
F_{wall}	force acting on the wall
Oh	Ohnesorge number, $\mu_l/\sqrt{\rho_l d_j \sigma_l}$
P_o	ambient pressure
P_p	pressure inside the peak area of fluid
P_v	pressure inside the valley area of fluid
ΔP	pressure difference between the inside the jet and the outside
$r_{1,2,3,4}$	radii as defined in Figure 7.20
r_j	radius of the cylindrical shell
t	wall thickness of a cylindrical shell
V_{piezo}	applied voltage to the piezo-electric crystals
δ	amplitude of perturbation
λ	wavelength between two neighboring droplets
λ/d_j	dimensionless wavelength
μ_l	viscosity of liquid
ρ_l	density of liquid
σ_h	hoop stress on the wall
σ_l	surface tension of liquid

Chapter 8 SUMMARY

The Uniform Droplet Spray (UDS) process, developed in the Laboratory for Manufacturing and Productivity at MIT, has many advantages such over conventional metal droplet production processes as gas atomization. The UDS process exploits the acoustically-amplified capillary instability phenomena of laminar liquid jets to produce uniform droplets. The principal advantage of the UDS process is the facility to produce uniform liquid droplets, which allows for greater control of the thermal state and mass flux of the droplet spray than other conventional methods.

This three-part thesis attempted to augment the understanding of the UDS process: (i) by studying the basic principles of jet break-up behavior of molten metal, (ii) by investigating the feasibility of the UDS process in production of balls usable in electronics packaging and in large production scale, and (iii) by investigating the effect of oxygen concentration in the spray chamber on the break-up of molten metal jets.

Chapter 1 discussed the background and motivation for this research. Also discussed were the objectives and an overview of the present investigation. Chapter 2 reviewed and examined the linear theories of jet break-up of liquid jets in a quiescent environment developed by Rayleigh and Weber. The effects of material properties such as density, surface tension, and viscosity were addressed. The importance of preventing the formation of satellites was mentioned, but not reviewed in detail. Also discussed was the liquid jet break-up in another liquid medium.

Chapter 3 discussed other important parameters affecting the UDS process. How the ejection pressure determines the jet velocity was discussed, as was the trajectory model of droplets with the modified drag coefficient for aligned droplets. The solidification model of droplets based on the assumption of Newtonian cooling was reviewed. The trajectory and solidification model is important in the design of the UDS apparatus and its process control parameters.

Chapter 4 discussed the break-up behavior of molten metal jets. The experimental apparatus and procedure were discussed. Jet velocities were measured for different ejection pressures and for repeatability from run-to-run. The sensitivity of jet velocity with respect to different measurement techniques was described. It was shown that the velocity was mostly affected by the uncertainty in the jet diameter, i.e., orifice diameter, and the break-up length of tin was affected by the perturbation frequency and amplitude. Maximum growth rate (or minimum jet break-up length) occurred at a dimensionless wavelength (the ratio of the wavelength to the jet diameter) of 4.10 as opposed to 4.51

predicted by Rayleigh. This discrepancy could have been remedied by more accurate measurement of jet velocity as well as the jet diameter. The break-up length was inverse-logarithmically related to the perturbation amplitude which was predicted by Rayleigh. It was shown that the liquid tin broke into a train of uniform droplets like a inviscid flow, which implies that the break-up behavior of a molten metal jet can be explained by Rayleigh's theory, provided that there is a sufficiently low oxygen concentration in the spray chamber.

Chapter 5 investigated the feasibility of using the UDS process for producing large solder balls that can be used for the BGA electronic packaging. Experimental apparatus and procedure of the UDS process were slightly modified to produce large solder balls and the modifications were discussed. The balls produced by the UDS process were spherical in shape and within a narrow dimensional tolerance. The UDS processed balls were compared with those produced by the conventional processes. The optical micrographs and back scattered electron images showed that the UDS produced balls had more uniform microstructures. This resulted in a narrow exothermic peak, showing better remelting characteristics.

Chapter 6 reviewed the theory of oxidation. Thermodynamic equilibrium conditions for surface oxidation of the molten tin was shown to be favorable under typical operating conditions. Oxidation kinetics of metals was reviewed. However, there were insufficient data to estimate the tin oxide thickness for the given conditions. The diffusion boundary layer thickness in the gas phase was estimated by using the theory of gas mass transfer, and it resulted in a thickness of 150 μm . The diffusion boundary layer thickness was also estimated by assuming the diffusion coefficient equals to the kinetic viscosity of air, which resulted in the thickness of 225 μm . It was further assumed that every oxygen molecule in the diffusion boundary layer was converted into tin oxide. The results are listed in Table 8.1. These results seem to underestimate the thickness at low oxygen concentrations and overestimate for high oxygen concentrations.

Possible oxidation mechanisms were also discussed. Tin oxide was assumed to grow by parabolic rate law. The oxide growth was estimated by the data in the literature. The tin oxide layer thickness was estimated to be 0.2 nm for an oxidation time of 3 ms at 555 K, as listed in Table 8.1 for comparison.

Table 8.1 The thickness of tin oxide layer with respect to the oxygen content in the spray chamber. The pressure of spray chamber is assumed to be 135 kPa (5 psig), temperature 298 K, molecular weight of stannic oxide, SnO₂, 150.7 kg/kmol, and density of SnO₂, 7000 kg/m³. The jet diameter is assumed to be 100 μm.

Oxygen content (ppm)	Oxide layer thickness (nm) if $\delta=150\ \mu\text{m}^*$	Oxide layer thickness (nm) if $\delta=225\ \mu\text{m}^{**}$	Oxide layer thickness (nm) From literature data ^{***}	Oxide layer thickness (nm) From AES measurements
5	0.0032	0.0043	n/a	1.8
250	0.16	0.21	n/a	n/a
500	0.32	0.43	n/a	1.8
750	0.47	0.64	n/a	n/a
1,000	0.63	0.85	n/a	n/a
1,250	0.80	1.07	n/a	n/a
1,500	0.95	1.28	n/a	n/a
1,750	1.10	1.50	n/a	n/a
2,000	1.26	1.71	n/a	1.8
200,000	126.00	171.00	0.2	1.8 ^{****}

* Using the diffusion boundary layer thickness

** Using the kinematic viscosity of gas as diffusion coefficient

*** From Kubaschewski and Hopkins (1962)

**** Represents the tin powder and fiber measurements

Chapter 7 discussed experimental results of the jet break-up length of molten tin and the oxide layer thickness at various oxygen concentrations in the spray chamber. It was observed that tin fiber formed instead of uniform droplets when oxygen concentration in the spray chamber was higher than 1,600 to 1,800 ppm for 100 μm tin jet. By increasing the perturbation amplitude to the orifice area, the tin jet was broken into droplets even at oxygen concentration of 1,600 ppm.

Experimental procedures for the measurement of oxide layer thickness were also discussed. The measurement was made with Auger Electron Spectroscopy. Tin powders produced at 5, 500, 2,000, and 200,000 ppm and tin fiber produced at 200,000 ppm were measured for their oxide layer thickness. It was discovered that they were approximately 1.8 nm for all the samples. Again, these are listed in Table 8.1 for comparison.

Also discussed in Chapter 7 was the effect of thin oxide film on the jet break-up under the assumption that the film was continuous and that the liquid jet covered by the thin film broke into a droplet under the force of liquid surface tension only. It was determined that the film thickness that could withstand the surface tension force was the ratio of the surface tension of liquid to the ultimate tensile strength of the oxide. Considering the

ultimate tensile strength of tin oxide layer, the results indicate that the tin jet should have broken into droplets.

In conclusion, the objectives of this thesis have been (i) to investigate the break-up behavior of molten metal jets, (ii) to produce large powders, and (iii) to establish a non-break-up criterion of metal jets. This thesis satisfies two objectives: It shows that the molten tin jet behaves like an inviscid flow when it breaks into a train of uniform droplets in a sufficiently low oxygen concentration. In other words, the break-up of molten tin jet follows the Rayleigh's analysis on a cylindrical jet instability. It also shows that the UDS process can produce large uniform powders for uses in the BGA electronic packaging. The process has been proven to produce uniform and spherical powders with a close dimensional tolerance. This thesis partially satisfies the third objective in answering the role of surface oxidation in the break-up of laminar liquid metal jets. It shows that the 100 μm tin jet does not break into droplets when the spray chamber contains more than 1,600 to 1,800 ppm oxygen. The oxide layer growth is investigated under the hypothesis that the tin jet does not break into droplets because of the oxide layer growth to a certain critical thickness. There is a discrepancy between the oxide layer thickness predicted by the theoretical estimation and by the experimental measurement by AES. The experimental results are not conclusive enough to establish the non-break-up criteria of molten tin jets using the oxide layer thickness as a criterion.

Based on the results of the current investigation, possible future work is discussed in detail in Chapter 9.

Chapter 9 **RECOMMENDATIONS FOR FURTHER RESEARCH**

Chapter 5 discussed the production of large solder balls. To eliminate the need for a large spray chamber, the molten metal jet was broken into a train of uniform droplets and solidified in a silicone oil. Section 2.5 in Chapter 2 discussed the theory of liquid jet break-up in another liquid medium, and Section 5.2.2 in Chapter 5 further discussed the implications of such break-up on the dimensionless wavelength at which the maximum instability occurs. Though producing large balls using the UDS process was proven to be promising and viable, further investigation is needed to eliminate irregular balls such as merged droplets and satellites, thereby increasing the production yield. Future research efforts may be directed as follows:

- *Effect of air bubbles in the silicone oil*

When the molten metal jet enters the surface of a silicone oil, the friction between the jet and the silicone oil creates air bubbles at the interface, thus creating air cavities. This may change the break-up behavior of a molten metal jet in the silicone oil. A high-speed camera can be used to capture the effect of the air cavities on the jet break-up. Since the friction significantly reduces the jet velocity, viscous friction effects need to be addressed theoretically and experimentally.

- *Charging of droplets in the silicone oil*

To eliminate merging of droplets, they are electrostatically charged when they are sprayed into a gaseous environment. All droplets, therefore, remain mono-sized and uniform. Electrostatic charging was used for producing large balls in silicone oil; preliminary results showed no or limited success, however. This may have been caused by the relative decrease in the electrostatic force on the droplets because of the large size and the significant increase in the drag force. Investigation on the electrostatic charging of droplets in the silicone oil should be continued as the means to eliminate droplet merging.

The role of surface oxidation in the break-up of laminar molten metal jet was investigated with the hypothesis that the jet does not break into a train of uniform droplets because of the build-up of the oxide layer to a certain critical thickness. To test the hypothesis, a 100 μm tin jet was sprayed into a chamber at various concentrations of oxygen. It was observed that the jet did not break when the spray chamber contained more

than 1,600 to 1,800 ppm oxygen. This implies that surface oxidation of molten metal jet affects the break-up process and the jet forms a fiber instead of droplets. It was shown that the jet break-up length increased with the increase in oxygen concentrations. However, the increase was not significant as seen in Figure 7.5.

Tin droplets and fibers were produced and collected at various oxygen concentrations and measured for their oxide layer thickness using Auger Electron Spectroscopy. It was expected that the thickness would increase with the increase in the oxygen concentrations. AES measurement, however, showed that the thicknesses of all samples were the same, about 1.8 nm. It was not possible to draw a definitive relationship between the oxide layer thickness and the oxygen concentrations. Therefore, it was not possible to establish a non-break-up criterion of molten tin jets with respect to the thickness of oxide layer. To determine such a criterion, the following future research is recommended.

- *Oxidation of metals at short time scale*

Many data on metal oxide growth are available in literature; however, almost all the data are for a long time scale, such as minutes, days, months, and years. Once the oxide layer forms on the metal surface, it acts as a barrier to further oxidation. For most metals, the oxide grows by a parabolic rate law, although a cubic rate law and a logarithmic rate law are also possible. The limiting condition for a long time scale is the diffusion of oxygen molecules through the oxide layer, which may explain why the oxide follows a parabolic rate law. Also important is the reaction between the oxygen molecules and the metal at the metal oxide/metal interface.

However, under typical operating conditions for the UDS process, the jet breaks into droplets within a few milliseconds. It is therefore necessary to look at the oxidation mechanisms and the oxide layer growth in the millisecond time scale.

- *Lateral growth of oxide*

Though it is important to look at the oxide growth at a short time scale, it is equally important to investigate how the oxide evolves. For example, the oxide layer may penetrate the metal sub-surface to a certain thickness and grow laterally afterward to join with another oxide layer. Thus, the lateral growth rate of oxide may become more important since its lateral growth may depend on the oxygen concentration.

The lateral growth of oxide may explain why the jet did not break into droplets at a certain critical oxygen concentration even though the oxide layer thickness was the same for all the samples as measured by AES. The oxide layer may not have been continuous at the

critical oxygen concentration, thus the jet broke into droplets rather than forming a fiber. Even if the oxide were continuous, the jet could have been broken into droplets if the bond strength between the oxide layer was not strong enough. This may explain why the jet readily broke into droplets when the perturbation amplitude was increased, as discussed in Section 7.2.2 in Chapter 7.

- *Surface morphology and structure*

Surface morphology of oxide layer may be affected by the oxygen concentration, which in turn may affect the jet break-up behavior. The microstructure too may change from an amorphous structure to a crystalline structure as the oxygen concentration increases.

- *In-situ measurement of oxide layer thickness*

Tin droplets and fibers were collected in a silicone oil, cleaned in solvents, and mounted in the transfer chamber, as discussed in Section 7.1.3 in Chapter 7. A significant time elapsed, however, before their thickness was measured by AES, which may not reflect the thickness at the time of break-up. Therefore, *in-situ* thickness measurement of the oxide layer is desirable though it may not be attainable with current state-of-the-arts experimental technology.

- *Modification of Rayleigh's analysis for two-phase flow*

In Section 7.2.6 in Chapter 7, a simple pressure vessel model was used to estimate the effect of thin oxide film on the jet break-up by assuming that the film was continuous. Rayleigh, as discussed in Section 2.2 in Chapter 2, used an energy method to obtain the growth factor to analyze the break-up behavior of an inviscid flow. It may be desirable, therefore, to modify Rayleigh's analysis to include the effect of strain energy in the film.

BIBLIOGRAPHY

- Abel, G.K., 1994, "Characterization of Droplet Flight Path and Mass Flux in Droplet-Based Manufacturing," S.M. Thesis, Department of Mechanical Engineering, MIT, Cambridge, MA.
- Ando, T., Chun, J.-H. and Sahu, S., 1993, "In-Flight Solidification of Uniform Droplets of Sn-25%Pb and Sn-40%Pb Alloys," *Proc. 1993 Powder Metallurgy World Congress*, edited by Bando, Y. and Kosuge, K., Jap. Soc. Powder and Powder Metallurgy, Kyoto, Japan, pp. 971-974.
- Barrett, C.R., Nix, W.D. and Tetelman, A.S., 1973, *The Principles of Engineering Materials*, Prentice-Hall, Inc., NJ, p. 128.
- Bewlay, B.P. and Cantor, B., 1991, "The Relationship Between Thermal History and Microstructure in Spray-Deposited Tin-Lead Alloys," *J. Mater. Res.*, vol. 6, no. 7, pp. 1433-1454.
- Brandes, E. A., ed., 1983, *Smithells Metals Reference Book, 6th edition*, Butterworths, London, pp. 14-1 - 14-13.
- Chaudhary, K.C. and Maxworthy, T., 1980a, "The Nonlinear Capillary Instability of a Liquid Jet. Part 2. Experiments on Jet Behavior Before Droplet Formation," *J. Fluid Mech.*, vol. 96, no. 2, pp. 275-286.
- Chaudhary, K.C. and Maxworthy, T., 1980b, "The Nonlinear Capillary Instability of a Liquid Jet. Part 3. Experiments on Satellite Drop Formation and Control," *J. Fluid Mech.*, vol. 96, no. 2, pp. 287-297.
- Chaudhary, K.C. and Redekopp, L.G., 1980, "The Nonlinear Capillary Instability of a Liquid Jet. Part 1. Theory," *J. Fluid Mech.*, vol. 96, no. 2, pp. 257-274.
- Chen, C.-A., Chun, J.-H. and Ando, T., 1994a, "Microstructural Control by Uniform-Droplet Spray Forming," *Advances in Powder Metallurgy and Particulate Materials*, vol. 6, edited by Lall, S. and Neupaver, A. J., Metal Powder Industries Federation, Princeton, NJ, pp. 227-234.
- Chen, C.-A., Sahu, S., Chun, J.-H. and Ando, T., 1994b, "Spray Forming with Uniform Droplets," *Science and Technology of Rapid Solidification and Processing*, edited by Otonari, M. A., Proc. NATO Workshop, Westpoint, NY, pp. 123-134.
- Chou, H., Chow, T.C., Tsay, S.F. and Chen, H.S., 1995, "Diffusivity of Oxygen in Liquid Tin and Ba_{0.35}Cu_{0.65} Alloys," *J. Electrochem. Soc.*, vol. 142, no. 6, pp. 1814-1819.
- Chu, M.G., Shiohara, Y. and Flemings, M.C., 1984, "Solidification of Highly Undercooled Sn-Pb Alloy Droplets," *Metall. Trans. A*, vol. 15A, pp. 1303-1310.
- Chun, J.-H. and Passow, C.H., 1993, "Production of Charged Uniformly Sized Metal Droplets," U.S. Patent No. 5,266,098.

- Crowley, J.M., 1968, "Lateral Instability of a Stream of Charged Droplets," *The Physics of Fluids*, vol. 11, no. 6, pp. 1372-1374.
- Danner, P., 1994, "Ball Grid Array Ceramic Packages," *Proceedings of the 3rd International Conference on Multichip Modules, SPIE vol. 2256*, p. 510.
- Deal, B.E. and Grove, A.S., 1965, "General Relationship for Thermal Oxidation of Silicon," *J. Applied Physics*, vol. 36, no. 12, pp. 3770-3778.
- Erin, T. and Hendricks, C.D., 1968, "Uniform Charged Solid Particle Production," *The Rev. of Sci. Inst.*, vol. 39, no. 9, pp. 1269-1271.
- Evans, R.W., Leatham, A.G. and Brooks, R.G., 1985, "The Osprey Preform Process," *Powder Metallurgy*, vol. 28, no. 1, pp. 13-20.
- Fillmore, G.L., Buehner, W.L. and West, D.L., 1977, "Drop Charging and Deflection in an Electrostatic Ink Jet Printer," *IBM J. Res. Develop.*, vol. 21, no. 2, pp. 37-47.
- Foulke, R.F., 1995, Ultra Clean International Corp., Woburn, MA, private communication.
- Goedde, E.F. and Yuen, M.C., 1970, "Experiments on Liquid Jet Instability," *Journal of Fluid Mechanics*, vol. 40, pp. 495-511.
- Grant, R.P. and Middleman, S., 1966, "Newtonian Jet Stability," *A. I. Ch. E. Journal*, vol. 12, no. 4, pp. 669-678.
- Grove, A.S., 1967, *Physics and Technology of Semiconductor Devices*, John Wiley & Sons, New York.
- Gutierrez-Miravete, E., Lavernia, E.J., Trapaga, G.M., Szekeley, J. and Grant, N.J., 1989, "Mathematical Model of the Spray Deposition Process," *Metall. Trans. A*, vol. 20A, pp. 71-85.
- Haenlein, A., 1932, "Disintegration of a Liquid Jet," NACA Technical Memorandum No. 659.
- Hasouna, A.T., Nogi, K. and Ogino, K., 1988, "Effect of Temperature and Atmosphere on the Wettability of Solid Copper by Liquid Tin," *Transactions of the Japan Institute of Metals*, vol. 29, no. 9, pp. 748-755.
- Hauffe, K., 1965, *Oxidation of Metals*, Plenum Press, New York.
- Heinzl, J. and Hertz, C.H., 1985, "Ink-Jet Printing," *Advances in electronics and electron physics*, vol. 65, pp. 91-171.
- Hendricks, C.D. and Babil, S., 1972, "Generation of Uniform, 0.5-10 μm , Solid Particles," *J. Phys. E*, vol. 5, pp. 905-910.
- Hendricks, C.D., 1973, "Mathematical Formulation of Electric Field Analysis," *Electrostatics and Its Applications*, edited by Moore, A.D., John Wiley & Sons, New York.

- Hertz, C.H. and Månsson, Å., 1972, "Electric Control of Fluid Jets and Its Application To Recording Devices," *Rev. Sci. Instru.*, vol. 43, no. 3, pp. 413-416.
- Jacob, K.T. and Jeffes, J.H.E., 1971, "Thermodynamic study of oxygen in liquid lead-tin alloys," *Trans. Inst. Min. Metall., Sect. C*, vol. 80, pp. C79-C86.
- Kamphoefner, F.J., 1972, "Ink Jet Printing," *IEEE Transactions on Electron Devices*, vol. ED-19, no. 4, pp. 584-593.
- Katz, L.E., 1988, "Oxidation," *VLSI Technology, 2nd edition*, edited by Sze, S.M., McGraw-Hill Book Co., New York.
- Keller, J.B., Rubinow, S.I. and Tu, Y.O., 1973, "Spatial Instability of a Jet," *The Physics of Fluids*, vol. 16, no. 12, pp. 2052-2055.
- Kubaschewski, O. and Hopkins, B.E., 1962, *Oxidation of Metals and Alloys, 2nd edition*, Butterworths, London.
- Lafrance, P., 1975, "Nonlinear Breakup of a Laminar Liquid Jet," *The Physics of Fluids*, vol. 18, no. 4, pp. 428-432.
- Lavernia, E.J. and Grant, N.J., 1988, "Spray Deposition of Metals: A Review," *Materials Science and Engineering*, vol. 98, pp. 381-394.
- Lee, H.C., 1974, "Drop Formation in a Liquid Jet," *IBM journal of Research and Development*, vol. 18, pp. 364-369.
- Lindblad, N.R. and Schneider, J.M., 1965, "Production of Uniform-Sized Liquid Droplets," *J. Sci. Inst.*, vol. 42, pp. 635-638.
- Lupis, C.H.P., 1983, *Chemical Thermodynamics of Materials*, Elsevier Science Publishing, New York, pp. 132-137.
- Mason, B.J., Jayaratne, O.W. and Woods, J.D., 1963, "An Improved Vibrating Capillary Device for Producing Uniform Water Droplets of 15 to 500 μm Radius," *J. Sci. Instrum.*, vol. 40, pp. 247-249.
- Mathur, P., Apelian, D. and Lawley, A., 1989, "Analysis of the Spray Deposition Process," *Acta Metall.*, vol. 37, no. 2, pp. 429-443.
- McCarthy, M.J. and Molly, N.A., 1974, "Review of Stability of Liquid Jets and the Influence of Nozzle Design," *The Chemical Engineering Journal*, vol. 7, pp. 1-20.
- Miks, J., 1994, "Cost Effective Ceramic Surface Mount Packaging for High I/O Applications," *Proceedings of the 3rd International Conference on Multichip Modules, SPIE vol. 2256*, p. 504.
- Miller, R.G. and Bowles, C.Q., 1990, "The Oxidation of 63Sn/37Pb at Typical Soldering Temperatures," *Oxidation of Metals*, vol. 33, pp. 95-101.
- Moulder, J., 1996, Physical Electronics, Eden Prairie, MN, private communication.

- Mulholland, J.A., Srivastava, R.K., and Wendt, J.O.L., 1988, "Influence of Droplet Spacing on Drag Coefficient in Nonevaporating, Monodisperse Streams," *AIAA Journal*, vol. 26, no. 10, pp. 1231-1237.
- Ohnesorge, W.V., 1936, "Drop Formation at Nozzles and the Decomposition of Liquid Jets," *Zeitschrift fur Angewandte Mathematik und Mechanik*, vol. 16, pp. 355-358.
- Ozisik, N.M., 1985, *Heat Transfer: A Basic Approach*, McGraw-Hill Book Co., New York.
- Passow, C.H., 1992, "A Study of Spray Forming Using Uniform Droplet Sprays," S.M. Thesis, Department of Mechanical Engineering, MIT, Cambridge, MA.
- Passow, C.H., Chun, J.-H. and Ando, T., 1993, "Spray Deposition of a Sn-40 wt pct Pb Alloy with Uniform Droplets," *Metall. Trans. A*, vol. 24A, pp. 1187-1193.
- Perepezko, J.H., 1980, "Crystallization of Undercooled Liquid Droplets," *Rapid Solidification Processing: Principles and Technologies, II*, edited by Mehrabian, R., Kear, B. H. and Cohen, M., Claitors Pub., Baton Rouge, LA, p. 56.
- Pimbley, W.T. and Lee, H.C., 1977, "Satellite Droplet Formation in a Liquid Jet," *IBM J. Res. Develop.*, vol. 21, no. 2, pp. 21-30.
- Poirier, D.R., 1988, "Densities of Pb-Sn Alloys during Solidification," *Metallurgical Transactions*, vol. 19A, pp. 2349-2354.
- Prabhakar, S.R. and Kapoor, M.L., 1993, "Thermodynamic Behavior of Oxygen in Liquid Lead-Tin Alloys," *Z. Metallkd.*, vol. 84, pp. 358-364.
- Rayleigh, Lord, 1878, "On the Instability of Jets," *Proc. London Mathematical Society*, vol. 10, pp. 4-13.
- Rutland, D.F. and Jameson, G.J., 1971, "A Non-Linear Effect in the Capillary Instability of Liquid Jets," *Journal of Fluid Mechanics*, vol. 46, pp. 267-271.
- Schmalzreid, H., 1974, *Solid State Reactions*, Academic Press, Inc., New York.
- Schneider, J.M. and Hendricks, C.D., 1964, "Source of Uniform-Sized Liquid Droplets," *Rev. Sci. Inst.*, vol. 35, no. 10, pp. 1349-1350.
- Shackelford, J.F. and Alexander, W., ed., 1992, *The CRC Materials Science and Engineering Handbook*, CRC Press, Inc., Boca Raton, FL.
- Shames, I.H., 1982, *Mechanics of Fluids, 2nd edition*, McGraw Hill Co., New York, pp. 258-261.
- Shaw, L., 1996, MIT, Cambridge, MA, private communication.
- Shutts, C.J., 1995, "Development of a Reliable Electrostatic Multijet Printhead for Three Dimensional Printing," S.M. Thesis, Department of Mechanical Engineering, MIT, Cambridge, MA.

- Sterling, A.M. and Sleicher, C.A., 1975, "The Instability of Capillary Jets," *Journal of Fluid Mechanics*, vol. 68, pp. 477-495.
- Stricker, J. and D. Sofer, 1991, "Monosize Droplet Stream Generator," *Rev. Sci. Instru.*, vol. 62, no. 12, pp. 3047-3050.
- Sweet, R.G., 1965, "High Frequency Recording with Electrostatically Deflected Ink Jets," *Rev. Sci. Inst.*, vol. 36, no. 2, pp. 131-136.
- Taimatsu, H. and Sangiorgi, R., 1992, "Surface Tension and Adsorption in Liquid Tin-Oxygen System," *Surface Science*, vol. 216, pp. 375-381.
- Taub, H.H., 1976, "Investigation of Nonlinear Waves on Liquid Jets," *The Physics of Fluids*, vol. 19, no. 8, pp. 1124-1129.
- Tomotika, S., 1935, "On The Instability of a Cylindrical Thread of a Viscous Liquid Surrounded by Another Viscous Fluid," *Proceedings of Royal Society*, vol. 150, pp. 322-337.
- Turnbull, D. and Cech, R.E., 1950, "Microscopic Observation of the Solidification of Small Metal Droplets," *J. Appl. Phys.*, vol. 21, pp. 804-810.
- Tyler, E. and Watkin, F., 1932, "Experiments With Capillary Jets," *Philosophical Magazine*, vol. 14, pp. 849-881.
- Tyler, E., 1933, "Instability of Liquid Jets," *Philosophical Magazine*, vol. 16, pp. 504-518.
- Weber, C., 1931, "The Decomposition of a Liquid Jet," *Zeitschrift für Angewandte Mathematik und Mechanik*, vol. 11, pp. 136-154.
- Yim, P., Chun, J.-H., Ando, T. and Sikka, V.K., 1995, "Production and Characterization of Mono-Sized Sn-38 wt.% Pb Alloy Balls," 1995 International Conference on Powder Metallurgy & Particulate Materials (PM2TEC'95), May 14-17, 1995, Seattle, Washington.
- Yim, P., Chun, J.-H., Ando, T. and Sikka, V.K., 1996, "Production and Characterization of Mono-Sized Sn-Pb Alloy Balls," *Int. J. Powder Metallurgy*, vol. 32, no. 2, pp. 155-164.
- Yuen, M.C., 1968, "Non-Linear Capillary Instability of a Liquid Jet," *Journal of Fluid Mechanics*, vol. 33, pp. 151-163.

Appendix A PHYSICAL PROPERTIES OF SELECTED MATERIALS

Table A.1 Physical properties of pure metals at normal temperatures *

Metal	Melting point (K)	Density at 293 K $\left(\frac{\text{kg}}{\text{m}^3}\right)$	Mean specific heat 273 - 373 K $\left(\frac{\text{J}}{\text{kg} \cdot \text{K}}\right)$	Thermal conductivity 273 - 373 K $\left(\frac{\text{W}}{\text{m} \cdot \text{K}}\right)$	Resistivity at 293 K $(\mu\Omega \cdot \text{m})$
Al	933.4	2700	917	238	0.0267
Cu	1357.8	8960	386.0	96	0.0169
In	429.4	7300	243	80.0	0.0880
Pb	600.5	11680	129.8	34.9	0.2060
Sn	505	7300	226	73.2	0.1260
Zn	692.6	7140	394	119.5	0.0596

* Selected physical properties listed in Tables A.1 to A.4 were taken from *Smithells Metals Reference Book, 6th Edition*, edited by E.A. Brandes.

Table A.2 Physical properties of pure metals at elevated temperatures

Metal	Temperature (K)	Specific heat $\left(\frac{\text{J}}{\text{kg} \cdot \text{K}}\right)$	Thermal conductivity $\left(\frac{\text{W}}{\text{m} \cdot \text{K}}\right)$	Resistivity $(\mu\Omega \cdot \text{m})$
Al	293	900	238	0.0267
	373	938	238	0.0355
	473	984	238	0.0478
	573	1030	238	0.0599
	673	1076	238	0.0730
Cu	293	385	394	0.01694
	373	389	394	-
	473	402	389	0.0293
	773	(427)	341 (811 K)	0.046 (770 K)
	1273	(473)	244 (1310 K)	0.081 (1250 K)
Pb	293	130	34.8	0.206
	373	134	33.5	0.270
	473	134	31.4	0.360
	573	138	29.7	0.500
Sn	293	222	65	0.126
	373	239	63	0.158
	473	260	60	0.230
Zn	293	389	113	0.0596
	373	402	109	0.078
	473	414	105	0.110
	573	431	101	0.130
	673	444	96	0.165

Table A.3 Physical properties of liquid metals

Density: $\rho = \rho_o + (T - T_o)(d\rho / dT)$
 Surfaced tension: $\sigma = \sigma_o + (T - T_o)(d\sigma / dT)$
 Viscosity: $\mu = \mu_o \exp(E / RT)$
 Universal gas constant: $R = 8.3144 \text{ J K}^{-1} \text{ mol}^{-1}$

Metal	Melting point (K)	Density		Surface tension		Viscosity		Activation energy $\left(\frac{\text{KJ}}{\text{mol}}\right)$
		ρ_o $\left(\frac{\text{kg}}{\text{m}^3}\right)$	$d\rho / dT$ $\left(\frac{\text{kg}}{\text{m}^3\text{K}}\right)$	σ_o $\left(\frac{\text{mN}}{\text{m}}\right)$	$d\sigma / dT$ $\left(\frac{\text{mN}}{\text{m} \cdot \text{K}}\right)$	μ_{mp} $\left(\frac{\text{mN} \cdot \text{s}}{\text{m}^2}\right)$	μ_o $\left(\frac{\text{mN} \cdot \text{s}}{\text{m}^2}\right)$	
Al	933.4	2385	-0.28	914	-0.35	1.30	0.1492	16.5
Cu	1357.8	8000	-0.801	1285	-0.13	4.0	0.3009	30.5
In	429.4	7023	-0.6798	556	-0.09	1.89	0.3020	6.65
Pb	600.5	10678	-1.3174	468	-0.13	2.65	0.4636	8.61
Sn	505	7000	-0.6127	544	-0.07	1.85	0.5382	(5.19)*
Zn	692.6	6575	-1.10	782	-0.17	3.85	0.4131	12.7

* estimated.

Table A.4 Thermal and electrical properties of liquid metals

Metal	Temperature (K)	Specific heat $\left(\frac{\text{J}}{\text{kg} \cdot \text{K}}\right)$	Thermal conductivity $\left(\frac{\text{W}}{\text{m} \cdot \text{K}}\right)$	Resistivity $(\mu\Omega \cdot \text{m})$
Al	933	1080	94.03	0.002425
	973	1080	95.37	0.002483
	1073	1080	98.71	0.002630
	1173	1080	102.05	0.002777
	1273	-	105.35	0.002924
Cu	1356	495	165.6	0.00200
	1373	495	166.1	0.00202
	1473	495	170.1	0.00212
	1673	495	176.3	0.00233
	1873	495	180.4	0.00253
Pb	600	152	15.4	0.009485
	673	144	16.6	0.009863
	773	137	18.2	0.010344
	873	135	19.9	(0.010825)
In	429.6	(259)	(42.)	0.003230
	473	(259)		0.003339
	673	(259)		0.004361
	873	(259)		(0.005131)
Sn	505	250	30.0	0.004720
	573	242	31.4	0.004906
	673	241	33.4	0.005171
	773	(240)	35.4	0.005435
	1273	(260)	-	(0.00670)
Zn	692.5	481	49.5	0.00374
	773	481	54.1	0.00368
	873	481	59.9	0.00363
	1073	481	(60.7)	0.00367

Table A.5 Density of solid lead-tin at 293 K *

Composition wt. %Sn	density $\left(\frac{\text{kg}}{\text{m}^3}\right)$
20	10204
50	8873
63	8403
70	8326
100	7305

* Selected physical properties listed in Tables A.5 to A.6 were taken from Poirier (1988).

Table A.6 Density of liquid lead-tin with the relationship of $\rho = c_1 + c_2(T - 273)$

Atomic fraction of Tin	Weight fraction of Tin	c_1 $\left(\frac{\text{kg}}{\text{m}^3}\right)$	$c_2 \times 10^3$ $\left(\frac{\text{kg}}{\text{m}^3 \cdot \text{K}}\right)$	Temperature range (K)
0.162	0.100	10490	-1.1582	583 to 793
0.300	0.197	10020	-1.27	551 to 825
0.304	0.200	9956	-1.0481	553 to 793
0.428	0.300	9497	-1.0109	533 to 793
0.434	0.305	9580	-1.30	531 to 857
0.457	0.325	9383	-0.9762	523 to 793
0.538	0.400	9079	-0.9708	513 to 793
0.604	0.466	8590	-0.72	571 to 801
0.624	0.487	8697	-0.8688	493 to 793
0.636	0.500	8671	-0.8761	493 to 793
0.724	0.600	8321	-0.8690	463 to 793
0.732	0.610	8140	-0.94	496 to 799
0.744	0.625	8229	-0.8652	463 to 793
0.803	0.700	7995	-0.8443	463 to 793
0.895	0.830	7603	-0.7760	483 to 793
0.908	0.850	7543	-0.7775	493 to 793

density of liquid eutectic alloy, 8050 kg/m³

Table A.7 The physical properties of silicone oil *

Density, ρ : $\rho = -\frac{T}{1300} + 1.083$, where $10^\circ\text{C} < T < 160^\circ\text{C}$
 Density unit in $\left(\frac{\text{g}}{\text{cc}}\right)$.

Surface tension, σ : 37.3 dynes/cm at 25 °C

Kinematic viscosity, ν : $\nu = \frac{4700}{T^{1.53}}$, where $10^\circ\text{C} < T < 150^\circ\text{C}$
 Kinematic viscosity in cst

Heat capacity, C_p : $C_p = \frac{T}{1750} + 0.354$, where $10^\circ\text{C} < T < 160^\circ\text{C}$
 Heat capacity unit in $\left(\frac{\text{cal}}{\text{g} \cdot \text{C}}\right)$

Conductivity, k : $k = -\frac{T}{5000} + 0.316$, where $20^\circ\text{C} < T < 160^\circ\text{C}$
 Conductivity unit in $\left(\frac{\text{cal}}{\text{s} \cdot \text{cm} \cdot \text{C} \cdot 10^3}\right)$

Note: unit for density	$\text{g/cc} = 10^3 \text{ kg/m}^3$
unit for surface tension	$\text{dynes/cm} = 10^{-3} \text{ N/m}$
unit for viscosity	$1 \text{ p (poise)} = 1 \text{ g/(cm}\cdot\text{s)} = 0.1 \text{ kg/(m}\cdot\text{s)} = 0.1 \text{ Pa}\cdot\text{s}$
unit for kinematic viscosity	$1 \text{ st (stokes)} = 1 \text{ cm}^2 / \text{s} = 10^{-4} \text{ m}^2 / \text{s}$
unit for energy	$\text{cal} = 4.2 \text{ J}$
unit for heat capacity	$\text{cal}/(\text{g}\cdot\text{C}) = 4.2 \text{ kJ}/(\text{kg}\cdot\text{C})$
unit for conductivity	$\text{cal} / (\text{s} \cdot \text{cm} \cdot \text{C} \cdot 10^3) = 0.42 \text{ W}/(\text{m}\cdot\text{C})$

* Properties of Dow Corning® 704 Diffusion Pump Fluid (Tetramethyltetraphenyl-Trisiloxane) provided by Dow Corning Corporation, Midland, Michigan 48686-0995. Telephone: (517) 496-4000